The Thesis Committee for Natalie Soheila Wolfenbarger
Certifies that this is the approved version of the following thesis:

Characterization of Star Tracker Distortion for the ICESat Mission

APPROVED BY
SUPERVISING COMMITTEE:

Srinivas Bettadpur, Supervisor

Tim Urban, Co-Supervisor

Dae Young Lee, Member

Characterization of Star Tracker Distortion for the ICESat Mission

by

Natalie Soheila Wolfenbarger, B.S.

Thesis

Presented to the Faculty of the Graduate School of

The University of Texas at Austin

in Partial Fulfillment

of the Requirements

for the Degree of

Master of Science in Engineering

The University of Texas at Austin

May 2017

This work is dedicated to Dr. Bob Schutz, who provided me with the means and opportunity to advance my understanding of aerospace engineering towards better serving society through improved precision in remote sensing data, which serves as the lens through which we observe and monitor our planet.

Acknowledgements

I would like to acknowledge Dr. Sungkoo Bae, whose input and guidance was essential to the development of this work. I would further like to acknowledge Dr. Tim Urban, whose dependable support was invaluable in times of instability. I would also like to acknowledge Dr. Srinivas Bettadpur, who provided me with the latitude to explore and find my own path. Finally, I would like to acknowledge the National Aeronautics and Space Administration who funded this work under grant NNX13AB40G.

Characterization of Star Tracker Distortion for the ICESat Mission

Natalie Soheila Wolfenbarger, M.S.E.
The University of Texas at Austin, 2017

Supervisor: Srinivas Bettadpur

Precision attitude determination is essential to the success of many spacecraft missions, particularly those in remote sensing where slight deviations in instrument pointing can yield high measurement errors, such as for the Ice, Cloud, and land Elevation Satellite (ICESat). Characterizing and understanding the nature of star tracker distortion is beneficial to the development of improved models for estimation and correction in data post-processing towards achieving arcsecond pointing accuracy for applications such as geolocation. Using a localized attitude dependent distortion estimation algorithm, star tracker distortion throughout the seven-year ICESat mission lifespan is analyzed to determine how the estimated distortion changes with respect to certain parameters of interest. These parameters include time, apparent motion of stars across the star tracker field of view, region of the celestial sphere observed, frequency and duration of star tracker blinding events, star tracker temperature, and star color. Distortion is estimated for each operational period and for the full mission.

An increase in the estimated distortion of approximately half an arcsecond to one arcsecond was observed over the duration of the mission. Regions of high and low distortion were observed to shift depending on the direction stars entered and exited the field of view. The region of the celestial sphere observed was determined to be insignificant relative to the effects of star motion across the field of view. Artificially high distortion observations that followed periods of blinding were confirmed to be the source of the high distortion estimated for certain operational periods of the mission. Star tracker temperature was determined to have no effect on the estimated distortion. Chromatic aberration could not be definitively confirmed. Recommendations are provided for implementation of this method on future missions. CCD aging effects should be considered if a static distortion model yields distortion residuals with a temporal dependence. The incorporation of telemetry from additional star trackers to support attitude determination while the star tracker of interest is blinded would eliminate high distortion observations caused by poor attitude estimates after periods of star tracker blinding. Adjustment of the distortion basis function to include star color dependent coefficients would allow for direct estimation of chromatic aberration. Proper consideration of the results presented in this thesis will yield a more robust distortion estimation and correction process for future missions which require precision pointing.

Table of Contents

List of Tables xii

List of Figures xiii

Chapter 1: Introduction 1

1.1 ICESat Mission Overview 1

1.2 Motivation for Distortion Correction on ICESat 6

1.3 Motivation for Distortion Correction on ICESat-2 9

1.4 Characterizing Star Tracker Distortion 10

Chapter 2: Star Tracker Distortion and Attitude Determination Errors 13

2.1 Star Trackers 13

2.2 Star Identification 16

2.3 The Attitude Determination Problem 17

2.4 Extended Kalman Filter 22

2.5 ICESat Attitude Determination Implementation 29

2.6 Star Tracker Error Sources 30

Chapter 3: Star Tracker Distortion Estimation 33

3.1 Star Tracker Distortion Models 34

3.2 Localized Attitude Dependent Distortion Estimation 37

Chapter 4: Results of Distortion Estimation 43

4.1 Star Tracker Distortion Maps 43

4.1.1 Campaign L1a 44

4.1.2 Campaign L2a 46

4.1.3 Campaign L2b 48
4.1.4 Campaign L2c 50
4.1.5 Campaign L3a 52
4.1.6 Campaign L3b 54
4.1.7 Campaign L3c 56
4.1.8 Campaign L3d 58
4.1.9 Campaign L3e 60
4.1.10 Campaign L3f 62
4.1.11 Campaign L3g 64
4.1.12 Campaign L3h 66
4.1.13 Campaign L3i 68
4.1.14 Campaign L3j 70
4.1.15 Campaign L3k 72
4.1.16 Campaign L2d 74
4.1.17 Campaign L2e 76
4.1.18 Campaign L2f 78
4.1.19 Mission 80
4.7.19 Summary 82
4.2 Effects of Aging on Distortion 84
4.3 Effects of Apparent Star Motion on Distortion 87
4.4 Effects of Region of Celestial Sphere Observed on Distortion 95
4.5 Effects of Blinding on Distortion 105
4.6 Effects of Temperature on Distortion 116
4.7 Effects of Star Color on Distortion 120

4.7.1 Campaign L1a 125
4.7.2 Campaign L2a 127
4.7.3 Campaign L2b 129
4.7.4 Campaign L2c 131
4.7.5 Campaign L3a 133
4.7.6 Campaign L3b 135
4.7.7 Campaign L3c 137
4.7.8 Campaign L3d 139
4.7.9 Campaign L3e 141
4.7.10 Campaign L3f 143
4.7.11 Campaign L3g 145
4.7.12 Campaign L3h 147
4.7.13 Campaign L3i 149
4.7.14 Campaign L3j 151
4.7.15 Campaign L3k 153
4.7.16 Campaign L2d 155
4.7.17 Campaign L2e 157
4.7.18 Campaign L2f 159
4.7.18 Mission 161
4.7.19 Summary 163

Chapter 5: Conclusions and Future Work 166

Appendix 1: ICESat Campaign Properties 170

Appendix 2: Star Observation Correlation Coefficients 170

References 171

Vita 174

List of Tables

Table 1: ICESat laser campaign periods. 3

Table 2: Relevant properties for the campaigns with the most correlated star observations. 99

Table 3: Campaign blinding observation statistics. 107

Table 4: Temperature data from the optical bench thermocouples for each campaign, excluding campaign L2f. 118

List of Figures

Figure 1: ICESat airplane and sailboat spacecraft attitude modes. Note that the solar panels have rotated between the two images. 4

Figure 2: Effect of pointing uncertainty on ranging measurement error. 5

Figure 3: Pinhole camera model of a star tracker. Relationship between the star tracker angle outputs and focal plane coordinates. Only the horizontal dimension is shown for clarity. 14

Figure 4: Outline of the precision attitude determination algorithm. The EKF initialization phase is implemented after periods of blinding. The filter is considered initialized after nine consecutive quaternions are generated using QUEST. A sufficient number of stars identified is defined as greater than or equal to four stars. 29

Figure 5: Comparison of distortion maps generated from three days of data from campaign L2a using an attitude independent and attitude dependent method. The top three maps were generated using an attitude independent method, whereas the bottom three were generated using an attitude dependent method. 37

Figure 6: Comparison of distortion maps generated using a 0^{th} order polynomial basis function and a FOV partitioned into 1024, $\frac{1}{4}^\circ \times \frac{1}{4}^\circ$ grids and a 3^{rd} order polynomial basis function and a FOV partitioned into 16, $2^\circ \times 2^\circ$ grids. The 3^{rd} order map is on the left and the 0^{th} order map is on the right. 38

Figure 7: Star tracker FOV partitioned into 16 grids and 9 regions to ensure continuity between localized distortion functions estimated for each region. 40

Figure 8: Distortion map for the ICESat IST, generated from observations collected during campaign L1a. 45

Figure 9: Distortion vector map for the ICESat IST, generated from observations collected during campaign L1a. 45

Figure 10: Star density map for the ICESat IST, generated from observations collected during campaign L1a. 46

Figure 11: Distortion map for the ICESat IST, generated from observations collected during campaign L2a. 47

Figure 12: Distortion vector map for the ICESat IST, generated from observations collected during campaign L2a. 47

Figure 13: Star density map for the ICESat IST, generated from observations collected during campaign L2a. 48

Figure 14: Distortion map for the ICESat IST, generated from observations collected during campaign L2b. 49

Figure 15: Distortion vector map for the ICESat IST, generated from observations collected during campaign L2b. 49
Figure 16: Star density map for the ICESat IST, generated from observations collected during campaign L2b. 50
Figure 17: Distortion map for the ICESat IST, generated from observations collected during campaign L2c. 51
Figure 18: Distortion vector map for the ICESat IST, generated from observations collected during campaign L2c. 51
Figure 19: Star density map for the ICESat IST, generated from observations collected during campaign L2c. 52
Figure 20: Distortion map for the ICESat IST, generated from observations collected during campaign L3a. 53
Figure 21: Distortion vector map for the ICESat IST, generated from observations collected during campaign L3a. 53
Figure 22: Star density map for the ICESat IST, generated from observations collected during campaign L3a. 54
Figure 23: Distortion map for the ICESat IST, generated from observations collected during campaign L3b. 55
Figure 24: Distortion vector map for the ICESat IST, generated from observations collected during campaign L3b. 55
Figure 25: Star density map for the ICESat IST, generated from observations collected during campaign L3b. 56

Figure 26: Distortion map for the ICESat IST, generated from observations collected during campaign L3c. 57
Figure 27: Distortion vector map for the ICESat IST, generated from observations collected during campaign L3c. 57
Figure 28: Star density map for the ICESat IST, generated from observations collected during campaign L3c. 58
Figure 29: Distortion map for the ICESat IST, generated from observations collected during campaign L3d. 59
Figure 30: Distortion vector map for the ICESat IST, generated from observations collected during campaign L3d. 59
Figure 31: Star density map for the ICESat IST, generated from observations collected during campaign L3d. 60
Figure 32: Distortion map for the ICESat IST, generated from observations collected during campaign L3e. 61
Figure 33: Distortion vector map for the ICESat IST, generated from observations collected during campaign L3e. 61
Figure 34: Star density map for the ICESat IST, generated from observations collected during campaign L3e. 62
Figure 35: Distortion map for the ICESat IST, generated from observations collected during campaign L3f. 63
Figure 36: Distortion vector map for the ICESat IST, generated from observations collected during campaign L3f. 63

Figure 37: Star density map for the ICESat IST, generated from observations collected during campaign L3f. 64
Figure 38: Distortion map for the ICESat IST, generated from observations collected during campaign L3g. 65
Figure 39: Distortion vector map for the ICESat IST, generated from observations collected during campaign L3g. 65
Figure 40: Star density map for the ICESat IST, generated from observations collected during campaign L3g. 66
Figure 41: Distortion map for the ICESat IST, generated from observations collected during campaign L3h. 67
Figure 42: Distortion vector map for the ICESat IST, generated from observations collected during campaign L3h. 67
Figure 43: Star density map for the ICESat IST, generated from observations collected during campaign L3h. 68
Figure 44: Distortion map for the ICESat IST, generated from observations collected during campaign L3i. 69
Figure 45: Distortion vector map for the ICESat IST, generated from observations collected during campaign L3i. 69
Figure 46: Star density map for the ICESat IST, generated from observations collected during campaign L3i. 70
Figure 47: Distortion map for the ICESat IST, generated from observations collected during campaign L3j. 71

Figure 48: Distortion vector map for the ICESat IST, generated from observations collected during campaign L3j. 71
Figure 49: Star density map for the ICESat IST, generated from observations collected during campaign L3j. 72
Figure 50: Distortion map for the ICESat IST, generated from observations collected during campaign L3k. 73
Figure 51: Distortion vector map for the ICESat IST, generated from observations collected during campaign L3k. 73
Figure 52: Star density map for the ICESat IST, generated from observations collected during campaign L3k. 74
Figure 53: Distortion map for the ICESat IST, generated from observations collected during campaign L2d. 75
Figure 54: Distortion vector map for the ICESat IST, generated from observations collected during campaign L2d. 75
Figure 55: Star density map for the ICESat IST, generated from observations collected during campaign L2d. 76
Figure 56: Distortion map for the ICESat IST, generated from observations collected during campaign L2e. 77
Figure 57: Distortion vector map for the ICESat IST, generated from observations collected during campaign L2e. 77
Figure 58: Star density map for the ICESat IST, generated from observations collected during campaign L2e. 78

Figure 59: Distortion map for the ICESat IST, generated from observations collected during campaign L2f. 79
Figure 60: Distortion vector map for the ICESat IST, generated from observations collected during campaign L2f. 79
Figure 61: Star density map for the ICESat IST, generated from observations collected during campaign L2f. 80
Figure 62: Distortion map for the ICESat IST, generated from observations collected over the full mission..... 81
Figure 63: Distortion vector map for the ICESat IST, generated from observations collected over the full mission..... 81
Figure 64: Star density map for the ICESat IST, generated from observations collected over the full mission..... 82
Figure 65: Maximum distortion estimated over each campaign. The horizontal distance between points is scaled to correspond to time in days. The two campaigns associated with the large spikes in maximum distortion, L2c and L3f, are the same campaigns with distortion maps that visibly differ from the other campaigns in the mission. The cause for these spikes will be discussed be discussed in the section, *Effects of Blinding on Distortion*. The maximum distortion increased from approximately 2.5 arcseconds to 3.5 arcseconds, resulting in a total increase of approximately one arcsecond. 85

Figure 66: Mean distortion estimated over each campaign. The horizontal distance between points is scaled to correspond to time in days. The mean distortion increased from approximately 0.8 arcseconds to 1.3 arcseconds, resulting in a total increase of approximately half an arcsecond. 86

Figure 67: Comparison of distortion map features for campaigns L2a and L3a, flown in (+Y) sailboat mode and (-Y) sailboat mode respectively. L2a spanned day 268 to day 323 of 2003. L3a spanned day 277 to day 313 of 2004. 89

Figure 68: Comparison of distortion map features for campaigns L2b and L3b, flown in (+Y) sailboat mode and (-Y) sailboat mode respectively. L2b spanned day 48 to day 81 of 2004. L3b spanned day 48 to day 83 of 2005. 90

Figure 69: Distortion maps for campaigns where ICESat was operated in the (–X) attitude mode. L2c spanned day 139 to day 173 of 2004. L3f spanned day 144 to day 177 of 2006. L2f spanned day 273 to day 284 of 2009. 92

Figure 70: Distortion maps for campaigns where ICESat was operated in the (+X) attitude mode. L3c spanned day 140 to day 174 of 2005. L3k spanned day 278 to day 293 of 2008. 93

Figure 71: Star tracker observation of the celestial sphere for an inertial orbit. The gray regions convey the star tracker line of sight. 96

Figure 72: Star tracker observation of the celestial sphere for a noon-midnight sun-synchronous orbit. The gray regions convey the star tracker line of sight. 97
Figure 73: Star tracker observation of the celestial sphere for an ICESat-like orbit. The gray regions convey the star tracker line of sight. 98
Figure 74: Distortion maps for campaigns L3d and L3i. Properties of these campaigns can be found in Table 2. 100
Figure 75: Distortion maps for campaigns L3g and L3k. Properties of these campaigns can be found in Table 2. 101
Figure 76: Distortion maps for campaigns L3e and L3j. Properties of these campaigns can be found in Table 2. 102
Figure 77: Distortion maps for campaigns L1a and L3b. Properties of these campaigns can be found in Table 2. 103
Figure 78: Example of high distortion observations occurring after periods of blinding during campain L1a on day 51 of the year 2003. 106
Figure 79: Distribution of high distortion observations for campaign L2c. 108
Figure 80: Distribution of high distortion observations for campaign L3c. 109
Figure 81: Distribution of high distortion observations for campaign L3f. 109

Figure 82: Distribution of high distortion observations for campaign L3g. 110
Figure 83: Distribution of high distortion observations for campaign L3h. 110
Figure 84: Distortion maps for campaigns L2c, L3c, and L3f illustrating the effects of high distortion observations following blinding periods. 112
Figure 85: Distortion maps excluding high distortion observations for campaigns L2c, L3c, and L3f. 115
Figure 86: Mean distortion estimated over each campaign. The horizontal distance between points is scaled to correspond to time in days. High and low temperature campaigns correspond to red and blue points respectively. 119
Figure 87: Star color histograms for stars defined in the GLAS star catalog and observed over the ICESat mission. 122
Figure 88: Effects of downsampling star observations on maximum estimated distortion for ICESat campaign L3a. 124
Figure 89: Distortion map for the ICESat IST, generated from blue star observations collected during campaign L1a. 126
Figure 90: Distortion vector map for the ICESat IST, generated from blue star observations collected during campaign L1a. 126
Figure 91: Star density map for the ICESat IST, generated from blue star observations collected during campaign L1a 127

Figure 92: Distortion map for the ICESat IST, generated from blue star observations collected during campaign L2a. 128
Figure 93: Distortion vector map for the ICESat IST, generated from blue star observations collected during campaign L2a. 128
Figure 94: Star density map for the ICESat IST, generated from blue star observations collected during campaign L2a. 129
Figure 95: Distortion map for the ICESat IST, generated from blue star observations collected during campaign L2b. 130
Figure 96: Distortion vector map for the ICESat IST, generated from blue star observations collected during campaign L2b. 130
Figure 97: Star density map for the ICESat IST, generated from blue star observations collected during campaign L2b. 131
Figure 98: Distortion map for the ICESat IST, generated from blue star observations collected during campaign L2c. 132
Figure 99: Distortion vector map for the ICESat IST, generated from blue star observations collected during campaign L2c. 132
Figure 100: Star density map for the ICESat IST, generated from blue star observations collected during campaign L2c. 133
Figure 101: Distortion map for the ICESat IST, generated from blue star observations collected during campaign L3a. 134
Figure 102: Distortion vector map for the ICESat IST, generated from blue star observations collected during campaign L3a. 134

Figure 103: Star density map for the ICESat IST, generated from blue star observations collected during campaign L3a. 135
Figure 104: Distortion map for the ICESat IST, generated from blue star observations collected during campaign L3b. 136
Figure 105: Distortion vector map for the ICESat IST, generated from blue star observations collected during campaign L3b. 136
Figure 106: Star density map for the ICESat IST, generated from blue star observations collected during campaign L3b 137
Figure 107: Distortion map for the ICESat IST, generated from blue star observations collected during campaign L3c. 138
Figure 108: Distortion vector map for the ICESat IST, generated from blue star observations collected during campaign L3c. 138
Figure 109: Star density map for the ICESat IST, generated from blue star observations collected during campaign L3c. 139
Figure 110: Distortion map for the ICESat IST, generated from blue star observations collected during campaign L3d. 140
Figure 111: Distortion vector map for the ICESat IST, generated from blue star observations collected during campaign L3d. 140
Figure 112: Star density map for the ICESat IST, generated from blue star observations collected during campaign L3d. 141
Figure 113: Distortion map for the ICESat IST, generated from blue star observations collected during campaign L3e. 142

Figure 114: Distortion vector map for the ICESat IST, generated from blue star observations collected during campaign L3e. 142
Figure 115: Star density map for the ICESat IST, generated from blue star observations collected during campaign L3e. 143
Figure 116: Distortion map for the ICESat IST, generated from blue star observations collected during campaign L3f. 144
Figure 117: Distortion vector map for the ICESat IST, generated from blue star observations collected during campaign L3f. 144
Figure 118: Star density map for the ICESat IST, generated from blue star observations collected during campaign L3f. 145
Figure 119: Distortion map for the ICESat IST, generated from blue star observations collected during campaign L3g. 146
Figure 120: Distortion vector map for the ICESat IST, generated from blue star observations collected during campaign L3g. 146
Figure 121: Star density map for the ICESat IST, generated from blue star observations collected during campaign L3g. 147
Figure 122: Distortion map for the ICESat IST, generated from blue star observations collected during campaign L3h. 148
Figure 123: Distortion vector map for the ICESat IST, generated from blue star observations collected during campaign L3h. 148
Figure 124: Star density map for the ICESat IST, generated from blue star observations collected during campaign L3h. 149

Figure 125: Distortion map for the ICESat IST, generated from blue star observations collected during campaign L3i. 150
Figure 126: Distortion vector map for the ICESat IST, generated from blue star observations collected during campaign L3i. 150
Figure 127: Star density map for the ICESat IST, generated from blue star observations collected during campaign L3i. 151
Figure 128: Distortion map for the ICESat IST, generated from blue star observations collected during campaign L3j. 152
Figure 129: Distortion vector map for the ICESat IST, generated from blue star observations collected during campaign L3j. 152
Figure 130: Star density map for the ICESat IST, generated from blue star observations collected during campaign L3j. 153
Figure 131: Distortion map for the ICESat IST, generated from blue star observations collected during campaign L3k. 154
Figure 132: Distortion vector map for the ICESat IST, generated from blue star observations collected during campaign L3k. 154
Figure 133: Star density map for the ICESat IST, generated from blue star observations collected during campaign L3k. 155
Figure 134: Distortion map for the ICESat IST, generated from blue star observations collected during campaign L2d. 156
Figure 135: Distortion vector map for the ICESat IST, generated from blue star observations collected during campaign L2d. 156

Figure 136: Star density map for the ICESat IST, generated from blue star observations collected during campaign L2d. 157
Figure 137: Distortion map for the ICESat IST, generated from blue star observations collected during campaign L2e. 158
Figure 138: Distortion vector map for the ICESat IST, generated from blue star observations collected during campaign L2e. 158
Figure 139: Star density map for the ICESat IST, generated from blue star observations collected during campaign L2e. 159
Figure 140: Distortion map for the ICESat IST, generated from blue star observations collected during campaign L2f. 160
Figure 141: Distortion vector map for the ICESat IST, generated from blue star observations collected during campaign L2f. 160
Figure 142: Star density map for the ICESat IST, generated from blue star observations collected during campaign L2f. 161
Figure 143: Distortion map for the ICESat IST, generated from blue star observations collected over the full mission. 162
Figure 144: Distortion vector map for the ICESat IST, generated from blue star observations collected over the full mission. 162
Figure 145: Star density map for the ICESat IST, generated from blue star observations collected over the full mission. 163

Chapter 1: Introduction

Remote sensing spacecraft often require highly accurate attitude knowledge since slight deviations in instrument pointing can introduce high measurement errors. Attitude determination in spacecraft is accomplished using a suite of instruments which can include star trackers and gyroscopes. Each instrument introduces different types of errors and uncertainties that must be quantified and compensated for in processing attitude and pointing solutions. Characterizing and understanding the nature of these errors is beneficial to the development of improved models for attitude estimation in post-processing towards achieving arcsecond-level attitude and pointing accuracy through reduction of uncertainty. The distinction between attitude and pointing is made to distinguish between determining the orientation of the spacecraft body frame and the orientation of the remote sensing instrument. Because relative motion between the instrument and spacecraft body can occur in flight due to temperature variations or other forcing mechanisms, the precision in attitude knowledge and pointing knowledge are not necessarily equivalent. The attitude and pointing determination problems are coupled in the sense that a reduction in attitude determination uncertainty allows for higher precision pointing knowledge. One such mission that required high precision instrument pointing knowledge was the Ice, Cloud, and land Elevation Satellite (ICESat), operational between 2003 and 2009.

1.1 ICESat Mission Overview

ICESat's primary mission was to determine changes in polar ice-sheet volume and assess the impact on global sea level using laser altimetry performed

by the Geoscience Laser Altimeter System (GLAS)[1]. ICESat operated at a 600 km altitude orbit with an inclination of 94°. This allowed the orbital plane to precess at a rate of 0.5° per day, producing 8-day and 91-day repeat ground tracks[1]. The GLAS instrument was comprised of three lasers: L1, L2, and L3. Only one laser was operational at a given time. During nominal operations near the beginning of the mission, laser L1 failed. This led to the adoption of a modified operational plan to maximize the lifetime of the remaining lasers, which called for intermittent laser operation. These periods of operation are referred to as campaigns and span approximately one month, three times per year[1]. The campaigns are defined in Table 1.

Table 1: ICESat laser campaign periods.

Campaign	Year	Day of Year	Calendar Day	Total Days	S/C Attitude Mode (GLAS Frame)
L1a	2003	051 – 088	20 Feb – 29 Mar	38	Sailboat/Airplane (-Y/+X)
L2a	2003	268 – 323	25 Sep – 19 Nov	55	Sailboat (+Y)
L2b	2004	048 – 081	17 Feb – 21 Mar	34	Sailboat (+Y)
L2c	2004	139 – 173	18 May – 21 Jun	35	Airplane (-X)
L3a	2004	277 – 313	03 Oct – 08 Nov	37	Sailboat (-Y)
L3b	2005	048 – 083	17 Feb – 24 Mar	36	Sailboat (-Y)
L3c	2005	140 – 174	20 May – 23 Jun	35	Airplane (+X)
L3d	2005	294 – 328	21 Oct – 24 Nov	35	Sailboat (+Y)
L3e	2006	053 – 087	22 Feb – 28 Mar	35	Sailboat (+Y)
L3f	2006	144 – 177	24 May – 26 Jun	34	Airplane (-X)
L3g	2006	298 – 331	25 Oct – 27 Nov	34	Sailboat (-Y)
L3h	2007	071 – 104	12 Mar – 14 Apr	34	Sailboat (-Y)
L3i	2007	275 – 309	02 Oct – 05 Nov	35	Sailboat (+Y)
L3j	2008	048 – 081	17 Feb – 21 Mar	34	Sailboat (+Y)
L3k	2008	278 – 293	04 Oct – 19 Oct	16	Airplane (+X)
L2d	2008	330 – 352	25 Nov – 17 Dec	23	Sailboat (-Y)
L2e	2009	068 – 101	09 Mar – 11 Apr	34	Sailboat (-Y)
L2f	2009	273 – 284	30 Sep – 11 Oct	12	Airplane (-X)

There are two primary spacecraft attitude modes: sailboat mode and airplane mode[1–3]. These attitude modes are employed to optimize the solar incidence on the solar panel arrays as the orbital plane precesses[1]. Figure 1 depicts the two spacecraft attitude modes and GLAS body axis definitions[2,3]. In sailboat mode, the y_G axis is approximately aligned to the spacecraft velocity vector[1]. In airplane mode, it is the x_G axis that remains aligned to the velocity vector[1]. The velocity vector can be aligned to either the positive or negative axis in both attitude

modes[1]. For a high beta angle*, the spacecraft enters sailboat mode whereas for a low beta angle, the spacecraft enters airplane mode[2,3].

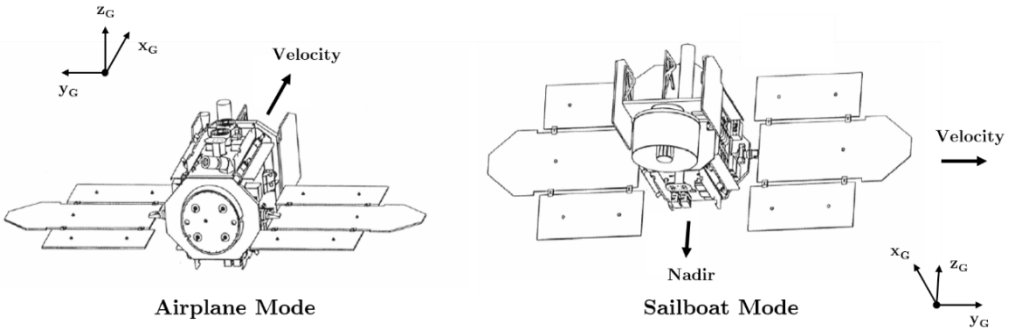

Figure 1: ICESat airplane and sailboat spacecraft attitude modes. Note that the solar panels have rotated between the two images.

The laser error budget allowed for 7.5 cm range error which corresponds to better than 1.5 arcsecond (1σ) pointing knowledge[4]. Figure 2 demonstrates how small errors in pointing can contribute to large errors in ranging measurements[4].

* Beta angle is defined as the angle between the spacecraft orbital plane and the Sun vector. Beta angle is defined between +90° and -90°. If the Sun vector is parallel to the orbital plane, the beta angle is 0°. If the Sun vector is perpendicular to the orbital plane, the beta angle is 90°.

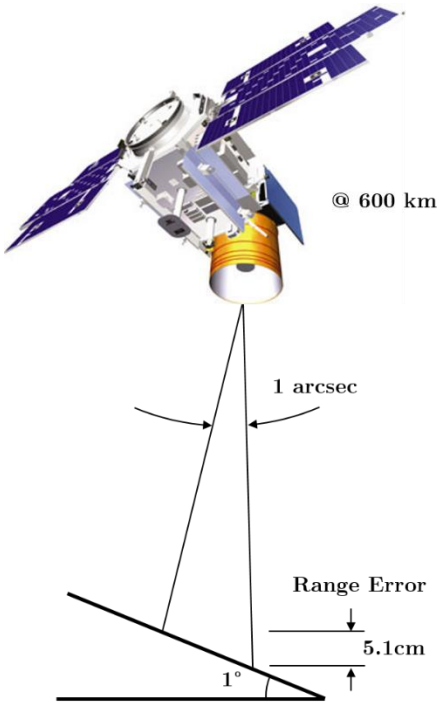

Figure 2: Effect of pointing uncertainty on ranging measurement error.

A Stellar Reference System (SRS) was designed to fulfill the laser pointing requirement[4]. The SRS is comprised of a star tracker, a gyroscope, two CCDs, and a series of retroreflectors. The star tracker used in the SRS is referred to as the instrument star tracker (IST). The IST is a Raytheon Optical System Inc. HD-1003 CCD star tracker operating at 10 Hz with an 8°×8° field of view (FOV) and an imaging array of 512×512 pixels[4]. The IST operates according to a search and track algorithm, where first the brightest stars are found in the FOV and then tracked until they exit from view. The 1σ uncertainty is 6 arcseconds in pitch and roll, and 0.2 in magnitude. The magnitude sensitivity range is between 2.0 and

6.0†. The gyroscope is a hemispherical resonator gyroscope (HRG), measuring angular rates at 10 Hz[4]. Two additional star trackers, Ball CT-602 star trackers (BSTs), were mounted on the spacecraft to support on-orbit attitude determination. Originally, data from the BSTs were intended to be used in conjunction with the IST or to serve as a backup unit for the IST in the precision pointing determination process[4]. Ultimately, only the IST was used for precision pointing determination. Because the IST is an integral component in the SRS which is used to determine the laser pointing direction, errors present in the IST are of great interest and significance to precision pointing determination.

A star catalog is used to identify stars observed by the star tracker. The star catalog contains the positions of stars in the Celestial Reference Frame (CRF) and their respective magnitudes. The mission star catalog for ICESat was constructed using the Hipparcos star catalog, which was the most accurate catalog at the time of the ICESat mission[4]. The median precision and brightness of the Hipparcos star catalog is 0.77 milliarcseconds and 0.0015 magnitude[4]. The star catalog is the closest representation of true star position available for the purposes of attitude determination.

1.2 Motivation for Distortion Correction on ICESat

In the initial phases of the mission, data obtained from the IST contained evidence of star tracker distortion, which manifested as consistently large residuals between the star position specified by the star catalog and the observed star

† Star magnitudes are defined using an inverse logarithmic relationship, where a smaller apparent magnitude corresponds to a brighter star.

position. This distortion was initially analyzed by examining the angles between stars identified in the star tracker FOV. The difference between the observed angle and the angle specified in the star catalog was computed for a subset of the available star tracker data. This subset of data was constructed using select observations from different campaigns to ensure the observations uniformly spanned the FOV, while minimizing the size of the data file. Given the rate of precession of the orbital plane, using the same amount of data from only a single campaign would span only a small fraction of the FOV. By dividing the FOV into grids, it was possible to calculate a mean angular error associated with each grid. The calculated mean corresponded to the average of all angular errors associated with stars observed within each grid. Using this method, it was possible to obtain a histogram plot, describing the number of grids corresponding to different magnitudes of mean angular error. These histograms were computed for both the IST and the two BSTs. The mean angular errors of the BSTs were tightly distributed around approximately 3 arcseconds, whereas the IST mean angular errors were more diffuse, spanning from a minimum value of approximately 5 arcseconds to a maximum of approximately 25 arcseconds. The magnitude and distribution of the mean angular errors for the IST were indicative of star tracker distortion. Once this phenomenon was observed, methods were sought to estimate and correct for the apparent star tracker distortion. These methods were successfully implemented for the IST and the two BSTs in work by Smith as a proof of concept study using only a small fraction of the available data[5].

Once the distortion estimation and correction algorithm was successfully validated, the scope of data used to obtain an estimate was expanded to include a

full campaign. Data from campaign L2a were used to generate a distortion estimate over the IST FOV, which was then used to correct observed star unit vectors for precision attitude determination. The attitude estimates produced by this method were officially released as ancillary files for ICESat/GLAS elevation product generation under ANC09 Release 13 (PAD calibration level 3)[6]. Instability issues with this campaign led to the adoption of a distortion map generated using star tracker data from campaign L3a. Attitude determination estimates generated using this distortion map corresponded to ANC09 Release 16 (PAD calibration level 3) through ANC09 Release 20 (PAD calibration level 3)[6]. At Release 19, campaign L2a had an estimated pointing knowledge accuracy of 5 arcseconds, whereas all other campaigns had pointing knowledge accuracy of 15-20 arcseconds[1]. This was still well above the 2 arcsecond accuracy requirement, but much improved from initial estimates conducted without performing distortion estimation and correction of the star tracker data.

After Release 20, an arctangent processing discrepancy was discovered[5]. This arctangent correction was applied and new attitude estimates were released under ANC09 Release 21 (PAD calibration level 1)[6]. This release was determined to have a pointing accuracy of approximately 2 arcseconds[5]. The apparent distortion was no longer observable after the arctangent correction was applied. Although the distortion estimation and correction algorithm was no longer necessary to obtain the required pointing knowledge accuracy, its success in mitigating the apparent distortion was recognized and the algorithm was proposed for inclusion in ICESat's follow-on mission, ICESat-2[7].

1.3 Motivation for Distortion Correction on ICESat-2

ICESat-2 is planned for launch in fall of 2017. It will operate at an altitude of 480 km at a 92° inclination. Its primary mission objectives parallel those of the original ICESat: to characterize polar ice sheet elevation change and sea ice thickness and its effect on global sea level using laser altimetry performed by the Advanced Topographic Laser Altimeter System (ATLAS). The pointing knowledge requirements are more stringent than ICESat at 3.1 microradians (1σ), which corresponds to less than 1 arcsecond[7]. A Laser Reference Sensor (LRS) system, serves as a single integrated platform to meet the laser pointing knowledge requirements, fulfilling the same role as GLAS on ICESat[8]. The LRS star tracker has a 12°×12° FOV and a 1024×1024 pixel detector array. Like ICESat, there are additional navigation sensors including two star trackers: the Sodern Hydra star trackers and a 50 Hz HRG. These star trackers are primarily used for on-orbit attitude determination; however, they may also be used to support precision pointing determination. The minimum operational mission lifetime is specified as three years, with a goal of five years[9]. In the Algorithm Theoretical Basis Document for Precision Pointing Determination, distortion correction is identified as one of four important deterministic corrections to apply to LRS star tracker measurements, others being integration time, centroiding error, and stellar aberration[4]. Furthermore, in night sky testing of the LRS star tracker, evidence of chromatic aberration was observed[8]. Methods that could mitigate these distortion effects are of great interest to achieving the sub-arcsecond pointing knowledge requirement for ICESat-2.

1.4 Characterizing Star Tracker Distortion

It is important to understand the characteristics of star tracker distortion when applying distortion estimation and correction algorithms to determine both the limitations of the algorithm and characterize the behavior of star tracker distortion over the period of a mission. Improved understanding of these limitations, artifacts, and trends will contribute to better reduction in pointing uncertainty. Seven years of star tracker telemetry are available from the ICESat mission. Applying previously developed distortion estimation and correction algorithms to these data will allow for improved understanding of star tracker distortion and provide valuable lessons learned for future applications on ICESat-2, where evidence of distortion has been observed in testing of the Laser Reference System (LRS) star tracker. Some parameters of interest have been selected for analysis based on their potential to influence star tracker distortion. These parameters include time, apparent motion of stars across the star tracker FOV, region of the celestial sphere observed, frequency and duration of star tracker blinding events, star tracker temperature, and star color. Analyzing how distortion changes over the duration of the mission will give insight into the effects of CCD aging, including the rate and magnitude of variation. Because stars are not stationary in the FOV, star motion may influence the estimated distortion due to a dynamic uncertainty in the FOV corresponding to transitions between pixels. Distortion may also be influenced by the region of stars observed by the star tracker. Over the period of an orbit, the star tracker observes only a fraction of the celestial sphere. Because the ICESat orbit precesses slowly, at 0.5° per day, the IST is periodically exposed to those same stars over multiple days. Blinding events,

where the star tracker is unable to observe any stars due to saturation, contribute to growth in attitude uncertainty as available observations become sparser and the attitude estimation filter must be repeatedly re-initialized. For distortion estimation methods dependent on attitude, this can cause high distortion observations associated with periods after blinding. Temperature fluctuations can cause physical distortion in the sensing array or other star tracker components. Higher temperatures can increase noise in the sensing array, resulting in an increase in apparent distortion. A star color dependent distortion, referred to as chromatic aberration, would manifest as distinct distortion fields for stars of specific colors. Characterizing and understanding the nature of star tracker distortion is beneficial to the development of improved models for estimation and correction in data post-processing towards achieving arcsecond pointing precision for applications like geolocation performed in support of ICESat and ICESat-2.

This thesis provides a thorough summary of the application of a localized distortion estimation technique to the ICESat IST data and evaluates the effects of mission-based parameters including time, apparent motion of stars across the star tracker FOV, region of the celestial sphere observed, frequency and duration of star tracker blinding events, star tracker temperature, and star color on the estimated star tracker distortion. Chapter 2 describes how a star tracker operates, presents an idealized model for star measurement by a star tracker, provides a brief overview of star identification methods, discusses the attitude determination problem in detail, describes the approach to precision attitude determination adopted for ICESat, and provides some examples of star tracker error sources. Chapter 3 defines the distortion estimation problem, presents the star tracker

distortion models found in current literature, and outlines the approach chosen for estimating distortion in the IST. Chapter 4 presents the estimated distortion for each campaign and the results of the analyses conducted to determine the effects of the chosen parameters of interest on the estimated distortion. Chapter 5 summarizes the conclusions and opportunities for future work. The conclusions derived from this study will be incorporated into the precision attitude and pointing determination process for ICESat-2. These conclusions have further application and relevance to future spacecraft missions that utilize star trackers for the purposes of attitude determination and can be included in calibration or post-processing efforts to reduce uncertainty through mitigation of star tracker distortion.

Chapter 2: Star Tracker Distortion and Attitude Determination Errors

Attitude sensors, including gyroscopes, sun sensors, magnetometers, and star trackers, are critical to successful navigation and attitude control. The telemetry obtained from these instruments is related to an inertial frame to determine the orientation, or attitude, of the spacecraft. Star trackers are particularly effective attitude sensors because their telemetry corresponds to observed star positions, which are essentially fixed on the celestial sphere.

2.1 Star Trackers

Star trackers are instruments comprised of a detector array, lens, and a computer. The detector technology can be either a charged coupled device (CCD) or complementary metal-oxide semiconductor (CMOS). In both cases, the detector array is comprised of photoelectric elements called pixels which generate charge when they encounter photons. The ICESat IST is a CCD-based star tracker. The CCD accumulates charge from incoming light for a predetermined amount of time called the integration period before the charges are digitized and transferred to the computer from which star positions and magnitudes can be derived. Approximately 60% of the photons that encounter each pixel are recorded by the CCD[4]. The recorded star magnitude corresponds to the amount of charge accumulated over the integration time. If the total charge falls below a certain threshold of photons, the star will not be recorded. This can occur when observing dimmer stars. For the IST, this threshold corresponds to a star magnitude of 6.0. For brighter stars, saturation can occur. Saturation is the phenomenon where accumulated charge

exceeds the capacity of a pixel and is spread to adjacent pixels. Additionally, as the charge accumulated approaches capacity, signal response to incoming light is reduced[10]. Typically, the lens is defocused such that incoming starlight is spread over multiple pixels on the detector surface. This allows for sub-pixel precision in determining the star position on the CCD array in a process referred to as centroiding[11]. The IST output consists of observed star magnitudes and the angles corresponding to the position of observed star centroids in the star tracker reference frame (SCF). These angles are generated from the digitized CCD coordinates, focal length, and a scaling factor provided by the manufacturer[5]. Figure 3 demonstrates the relationship between these parameters.

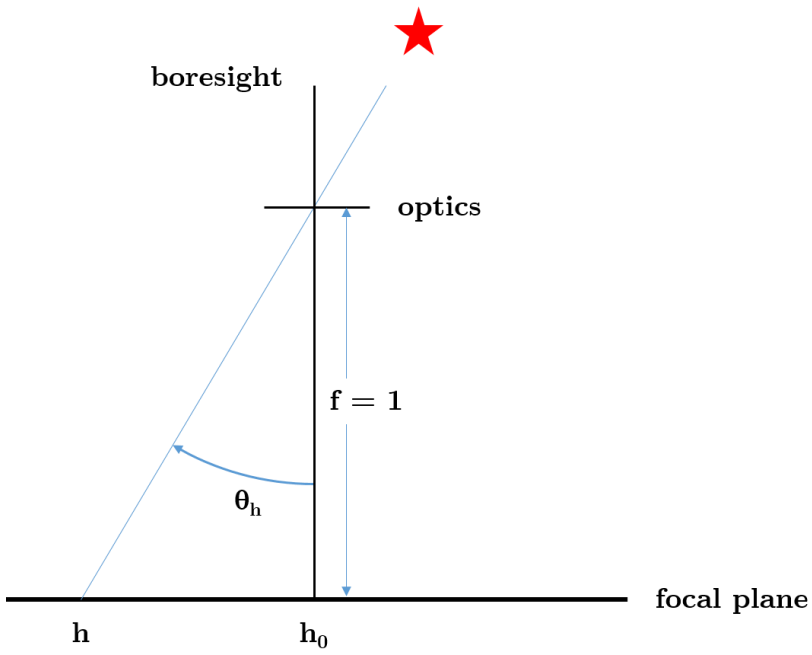

Figure 3: Pinhole camera model of a star tracker. Relationship between the star tracker angle outputs and focal plane coordinates. Only the horizontal dimension is shown for clarity.

From these angles, the unit vector in the SCF can be calculated using a pinhole camera model where θ_h is the horizontal angle output, θ_v is the vertical angle output, h is the horizontal focal plane coordinate, v is the vertical focal plane coordinate, h_0 is the horizontal principal point, v_0 is the vertical principal point, and 1 is the scaled focal length[12,13].

$$\begin{aligned} h &= \tan\theta_h \\ v &= \tan\theta_{\mathrm{v}} \end{aligned} \tag{1}$$

$$u = \begin{bmatrix} u_1 \\ u_2 \\ u_3 \end{bmatrix} = \frac{1}{\sqrt{(h-h_0)^2 + (v-v_0)^2 + 1}} \begin{bmatrix} h-h_0 \\ v-v_0 \\ 1 \end{bmatrix} \tag{2}$$

The pinhole camera model is an idealized model that assumes light travels in a straight line from its source through the pinhole to the detector surface, neglecting any diffraction due to the lens[12,13]. The vertical and horizontal star positions in the focal frame used in the distortion estimation algorithm are related to the unit vectors by

$$\begin{aligned} h &= \frac{u_1}{u_3} \\ v &= \frac{u_2}{u_3} \end{aligned} \tag{3}$$

Once observed star positions and magnitudes are recorded, they can be associated with reference stars in the star catalog and identified. There are a variety of star

identification algorithms in use today. The star identification algorithm used for ICESat incorporates both a pattern matching algorithm and direct matching algorithm.

2.2 Star Identification

There have been multiple approaches to the problem of star identification since the first implementation of star cameras towards spacecraft attitude determination. In their review paper, "A Survey on Star Identification Algorithms", Spratling and Mortari provide a thorough summary of star identification algorithms from the first algorithm published by Junkins *et al.* in "Star Pattern Recognition and Spacecraft Attitude Determination" in 1981 to Kolomenkin's proposed modification to Mortari's Search-Less algorithm in 2008. Most advancements in the development of star identification algorithms have been to reduce search time. Even the development of Mortari's celebrated Pyramid algorithm, which is extremely robust to non-stars, was motivated by the reduction of iterations in his Search-Less algorithm[14]. For ground-based processing towards precision pointing determination, minimizing the occurrences of misidentification is prioritized over a reduction of processing speed.

The two algorithms chosen for star identification on ICESat include a pattern matching algorithm (PMA) and a direct matching technique (DMT). In PMA, a geometric approach is employed towards identifying groups of stars simultaneously observed in the FOV. This typically requires at least three stars to be observed within the FOV. A benefit of this type of algorithm is that no a priori attitude estimate is required. One deficiency in this type of algorithm is the

increased probability of misidentification. To reduce both probability of misidentification and search time, the celestial sphere can be partitioned into grids. Given a good a priori boresight direction, only the portion of the star catalog containing stars within the region defined by grids adjacent to or containing the boresight vector will be considered in the matching algorithm. In DMT, an a priori attitude estimate is used in conjunction with observed star magnitude and position to identify a single star in the FOV. This process is repeated for all stars observed in the FOV. Prior to launch, the algorithms were evaluated through simulation of one orbital period of data for different values of right ascension. Both algorithms performed well, with the PMA exhibiting misidentification in only a fraction of a percent of cases considered whereas the DMT experienced no misidentifications[4]. In the ICESat precision pointing determination algorithm, the PMA is primarily used for initialization whereas the DMT is employed in all other cases. Analysis of the attitude determination output files over all campaigns of the mission indicates that the PMA was used 287,429 times in total whereas the DMT was used 500,577,979 times in total. The simulated performance of these star identification algorithms suggests that misidentification of stars is not a significant driver in star tracker derived attitude determination error sources for ICESat.

2.3 The Attitude Determination Problem

The problem of spacecraft attitude determination using star trackers can be posed simply as finding the matrix that maps the catalog star position vectors to the position vectors of stars observed in the star tracker FOV. This matrix represents a rotation from the CRF to the spacecraft body frame. For multiple

unit vector observations, this problem takes the form of a classical least squares problem. The least squares attitude determination problem, referred to as the Wahba Problem, corresponds to the minimization of the cost function

$$J(A) = \frac{1}{2}\sum_{i=1}^{n} a_i \left|\widehat{\boldsymbol{W}}_{\boldsymbol{i}} - A\widehat{\boldsymbol{V}}_{\boldsymbol{i}}\right|^2 \tag{4}$$

where $\widehat{\boldsymbol{W}}_{\boldsymbol{i}}$ represents the unit vector of the star observation in the spacecraft frame and $\widehat{\boldsymbol{V}}_{\boldsymbol{i}}$ is the unit vector of the star catalog position in the CRF, a_i is the weight associated with the observation, n is the number of unit vector observations, and A is the attitude matrix of interest[15]. Note that because the attitude matrix is a rotation matrix, it is orthogonal with determinant of one[16]. Wahba chooses to normalize the weights such that

$$\sum_{i=1}^{n} a_i = 1 \tag{5}$$

which through manipulation yields a cost function of the form

$$J(A) = 1 - \sum_{i=1}^{n} a_i \widehat{\boldsymbol{W}}_i{}^T A\widehat{\boldsymbol{V}}_i \tag{6}$$

where by inspection, maximization of the cost function

$$J'(A) = \sum_{i=1}^{n} a_i \widehat{\boldsymbol{W}}_i{}^T A \widehat{\boldsymbol{V}}_i \tag{7}$$

will minimize $J(A)$. $J'(A)$ can be equivalently expressed as

$$J'(A) = \sum_{i=1}^{n} a_i \operatorname{tr}\left[A \widehat{\boldsymbol{V}}_i \widehat{\boldsymbol{W}}_i{}^T\right] \tag{8}$$

or even more simply as

$$J'(A) = \operatorname{tr}[AB^T] \tag{9}$$

where

$$B = \sum_{i=1}^{n} a_i \widehat{\boldsymbol{W}}_i \widehat{\boldsymbol{V}}_i{}^T \tag{10}$$

The same result would be obtained using the approach of Markley and Mortari where instead of normalizing the weights, the weights can be set to correspond to the inverse variances such that Wahba's problem relates to the Maximum Likelihood Estimate[17].

In the ICESat attitude determination algorithm, the QUaternion ESTimator (QUEST) algorithm is used to solve Wahba's problem. QUEST is an implementation of Davenport's q-method developed by Shuster[17]. In Davenport's q-method, the attitude matrix, A, is parameterized by a unit quaternion defined as

$$\boldsymbol{q} = \begin{bmatrix} \boldsymbol{q_v} \\ q_4 \end{bmatrix} = \begin{bmatrix} \boldsymbol{e} \sin\left(\frac{\emptyset}{2}\right) \\ \cos\left(\frac{\emptyset}{2}\right) \end{bmatrix} \tag{11}$$

such that

$$A(\boldsymbol{q}) = ({q_4}^2 - |\boldsymbol{q_v}|^2)\, I_{3\times3} + 2\boldsymbol{q_v}{\boldsymbol{q_v}}^T - 2q_4 Q \tag{12}$$

where $\boldsymbol{e}$ defines the axis of rotation, $\emptyset$ defines the angle of rotation, and Q is the skew symmetric matrix defined by

$$Q \equiv \begin{bmatrix} 0 & -q_3 & q_2 \\ q_3 & 0 & -q_1 \\ -q_2 & q_1 & 0 \end{bmatrix} \tag{13}$$

Using this parameterization of A, the cost function shown in Eq. 9 can be equivalently expressed as

$$J'(A) = \mathrm{tr}[AB^T] = \boldsymbol{q}^T K \boldsymbol{q} \tag{14}$$

where

$$S = B + B^T, \qquad K \equiv \begin{bmatrix} S - I_{3\times3}\,\mathrm{tr}(B) & \boldsymbol{z} \\ \boldsymbol{z}^T & \mathrm{tr}(B) \end{bmatrix} \tag{15}$$

and

$$\boldsymbol{z} \equiv \sum_{i=1}^{n} a_i \, \widehat{\boldsymbol{W}}_i \times \widehat{\boldsymbol{V}}_i \tag{16}$$

The optimal quaternion is the normalized eigenvector corresponding to the largest eigenvalue of the matrix K[18]. The QUEST method deviates from Davenport's q-method here, where a Newton-Raphson approach is used to solve the eigenvalue problem instead of more robust computationally expensive methods[18]. The summation of the weights defined in the cost function is used to initialize the Newton-Raphson method[17]. If weights were normalized, the initial estimate for λ_{max} would be one[17,18]. Once the maximum eigenvalue is obtained, the optimal quaternion can be computed using

$$\boldsymbol{q} = \frac{1}{\sqrt{\gamma^2 + |\boldsymbol{x}|^2}} \begin{bmatrix} \boldsymbol{x} \\ \gamma \end{bmatrix} \tag{17}$$

where

$$\boldsymbol{x} \equiv \text{adj}[(\lambda_{max} + \text{tr}(B))I_{3\times 3} - S]\boldsymbol{z} \tag{18}$$

and

$$\gamma \equiv \det[(\lambda_{max} + \text{tr}(B))I_{3\times 3} - S] \tag{19}$$

The covariance matrix associated with the rotation angle error is given by

$$P = \left[\sum_{i=1}^{n} a_i (I_{3\times 3} - \widehat{\boldsymbol{W}}_i \widehat{\boldsymbol{W}}_i^{\boldsymbol{T}})\right]^{-1} \tag{20}$$

Although the quaternion yielded by QUEST corresponds to the optimal attitude, the attitude estimate can be further refined by incorporating gyroscope measurements and implementing a filter to reduce measurement noise. The filter can either incorporate the optimal quaternion generated using QUEST into the observation model or incorporate the star unit vectors directly. The observation model used in the ICESat algorithm directly includes star unit vector observations and as such is called a unit vector filter (UVF) observation model[4]. This model will be further defined in the next section.

2.4 Extended Kalman Filter

Due to the nonlinear nature of the problem, the standard filtering algorithm applied to the attitude determination problem is the Extended Kalman Filter (EKF). The algorithm for ICESat is adapted from work by Lefferts, Markley, Shuster, Fisher and Strikwerda[19,20]. The dynamics are modeled as

$$\begin{aligned} \frac{d}{dt}\,\boldsymbol{q}(t) &= \frac{1}{2}\Omega(\boldsymbol{\omega}(t))\boldsymbol{q}(t) \\ \frac{d}{dt}\,\boldsymbol{\omega}(t) &= \boldsymbol{\eta}(t) \end{aligned} \tag{21}$$

where $\boldsymbol{q}$ is the quaternion, $\boldsymbol{\omega}$ is the angular rate, $\boldsymbol{\eta}$ is Gaussian white noise and Ω is defined as

$$\Omega(\boldsymbol{\omega}) \equiv \begin{bmatrix} 0 & \omega_3 & -\omega_2 & \omega_1 \\ -\omega_3 & 0 & \omega_1 & \omega_2 \\ \omega_2 & -\omega_1 & 0 & \omega_3 \\ -\omega_1 & -\omega_2 & -\omega_3 & 0 \end{bmatrix} \tag{22}$$

The state vector given by

$$\boldsymbol{x}(t) = \begin{bmatrix} \boldsymbol{q}(t) \\ \boldsymbol{\omega}(t) \end{bmatrix} \tag{23}$$

and the deviation from the state is given by

$$\Delta\boldsymbol{x}(t) = \begin{bmatrix} \boldsymbol{\Delta\theta}(t) \\ \boldsymbol{\Delta\omega}(t) \end{bmatrix} = \begin{bmatrix} \frac{\Delta q_1(t)}{2} \\ \frac{\Delta q_2(t)}{2} \\ \frac{\Delta q_3(t)}{2} \\ \boldsymbol{\Delta\omega}(t) \end{bmatrix} \tag{24}$$

Note that $\boldsymbol{x}(t) \in \mathbb{R}^7$ and $\Delta\boldsymbol{x}(t) \in \mathbb{R}^6$. The reduction in dimension from the state occurs to address the inherent dependence of the four quaternion components caused by the unit norm constraint. If the deviation is defined to correspond to the full seven-dimensional state, the resulting covariance matrix is singular. This singularity is difficult to maintain numerically due to finite precision. Different methods have been proposed to address this numerical instability, including a

reduced representation of the covariance matrix, truncating the state deviation, and representing the state in a body-fixed frame[19]. The ICESat precision attitude determination algorithm implements the truncation of state deviation method. Because the angular deviation is small, the scalar component of the deviation corresponding to the quaternion is simply 1 to the first order. This allows the dynamic model for the state deviations to be expressed as

$$\begin{aligned} \frac{d}{dt}\,\boldsymbol{\Delta\theta}(t) &= [\boldsymbol{\omega}(t)]\boldsymbol{\Delta\theta}(t) + \boldsymbol{\Delta\omega}(t) + \boldsymbol{\eta_1}(t) \\ \frac{d}{dt}\,\boldsymbol{\Delta\omega}(t) &= \boldsymbol{\eta_2}(t) \end{aligned} \tag{25}$$

where $[\boldsymbol{\omega}(t)]\boldsymbol{\Delta\theta}(t)$ is the matrix representation of the cross product $-\boldsymbol{\omega}(t)\times\boldsymbol{\Delta\theta}(t)$ such that

$$[\boldsymbol{\omega}(t)] = \begin{bmatrix} 0 & \omega_3 & -\omega_2 \\ -\omega_3 & 0 & \omega_1 \\ \omega_2 & -\omega_1 & 0 \end{bmatrix} \tag{26}$$

and the $\boldsymbol{\eta_1}$ and $\boldsymbol{\eta_2}$ terms describe the process noise associated with the different terms in the state deviation dynamics. The state prediction equations, map the state from the previous estimate, denoted by $k-1$, to the current estimate, denoted by k. The notation $k|k-1$ simply conveys that the state at k is defined given information from the previous estimate at $k-1$. The prediction equations correspond to

$$\begin{aligned} \boldsymbol{q}_{k|k-1} &= M_{k-1}\boldsymbol{q}_{k-1} \\ \boldsymbol{\omega}_{k|k-1} &= \boldsymbol{\omega}_{k-1} \end{aligned} \tag{27}$$

where

$$M_{k-1} = \cos\left(\frac{\phi_{k-1}}{2}\right) I_{4\times 4} + \sin\left(\frac{\phi_{k-1}}{2}\right) \Omega(\widehat{\boldsymbol{n}}_{\boldsymbol{k-1}}) \tag{28}$$

where $\boldsymbol{\phi}_{k-1}$ is the angle of rotation given the estimated angular rate and elapsed time and $\widehat{\boldsymbol{n}}_{k-1}$ defines the unit axis of rotation such that

$$\phi_{k-1} \equiv |\boldsymbol{\omega}_{k-1}|(t_k - t_{k-1}) \tag{29}$$

$$\widehat{\boldsymbol{n}}_{k-1} \equiv \frac{\boldsymbol{\omega}_{k-1}}{|\boldsymbol{\omega}_{k-1}|} \tag{30}$$

The estimated angular velocity is constant between filter updates and thus the mapping matrix simply corresponds to identity. The state deviation covariance matrix is found using

$$P_{k|k-1} = \Phi_{k-1} P_{k-1} {\Phi_{k-1}}^T + \mathrm{Q}_{k-1} \tag{31}$$

where $\Phi_{k-1} = \Phi(t_k - t_{k-1})$ corresponds to the state deviation transition matrix from t_{k-1} to t_k and Q_{k-1} is the process noise covariance matrix. The state

transition matrix can be derived by expressing the state deviation dynamics equations in terms of a single linear differential equation given by

$$\frac{d}{dt}\,\boldsymbol{\Delta x}(t) = F(t)\boldsymbol{\Delta x}(t) + G(t)\boldsymbol{\eta}(t) \tag{32}$$

where

$$F(t) = \begin{bmatrix} [\boldsymbol{\omega}(t)] & I_{3\times3} \\ 0_{3\times3} & 0_{3\times3} \end{bmatrix} \tag{33}$$

$$G(t) = \begin{bmatrix} 0_{3\times3} \\ I_{3\times3} \end{bmatrix} \tag{34}$$

Assuming discrete time process noise and recognizing $\boldsymbol{\omega}(t)$ is constant over the interval $(t_k - t_{k-1})$, an analytic representation of the state deviation transition matrix and the process noise covariance matrix can be obtained. The full analytic expression can be found in "Attitude Determination for the Star Tracker Mission" by Fisher *et al.*

As noted in the previous section, the measurement model for the EKF is based on the UVF observation model. The measurement model is defined as

$$\boldsymbol{z}_k = \widehat{\boldsymbol{W}}_k - \widehat{\boldsymbol{W}}_{k-1} \tag{35}$$

$\widehat{\boldsymbol{W}}_k$ is modeled by

$$\widehat{\boldsymbol{W}}_k = A_k \widehat{\boldsymbol{V}}_k + \Delta\widehat{\boldsymbol{W}}_k \tag{36}$$

where $\Delta\widehat{\boldsymbol{W}}_k$ is the error associated the attitude matrix, assumed to be zero-mean Gaussian white noise. $\widehat{\boldsymbol{W}}_{k-1}$is the predicted star unit vector obtained using

$$\widehat{\boldsymbol{W}}_{k|k-1} = A_{k|k-1} \widehat{\boldsymbol{V}}_k \tag{37}$$

Substituting the equations above into the measurement model, a new definition of the measurement model corresponding to

$$\boldsymbol{z}_k = A_k \widehat{\boldsymbol{V}}_k + \Delta\widehat{\boldsymbol{W}}_k - A_{k|k-1} \widehat{\boldsymbol{V}}_k \tag{38}$$

can be obtained. A_k can be expressed as a function of $A_{k|k-1}$ using a matrix exponential because the transition matrix associated with the attitude matrix is composed of constant coefficients. The expression can be expanded to the first order, noting the argument $\Delta\boldsymbol{\theta}_k$ is small so higher terms can be neglected, to obtain

$$A_k = e^{-[\Delta\boldsymbol{\theta}_k]} A_{k|k-1} \approx (I_{3\times 3} - [\Delta\boldsymbol{\theta}_k]) A_{k|k-1} \tag{39}$$

Substituting the expanded form of this equation into the measurement model yields

$$\boldsymbol{z}_k = \left[\widehat{\boldsymbol{W}}_{k|k-1}\right] \Delta\boldsymbol{\theta}_k + \Delta\widehat{\boldsymbol{W}}_k \tag{40}$$

where the sensitivity matrix used in the EKF equations can be derived via inspection as simply

$$H_k = \left[\left[\widehat{\boldsymbol{W}}_{k|k-1}\right] \quad 0_{3\times 3}\right] \tag{41}$$

The EKF update equations are given by

$$\begin{aligned} K_k &= P_{k|k-1}{H_k}^T\left(H_k P_{k|k-1}{H_k}^T + R_k\right)^{-1} \\ \Delta\boldsymbol{x}_k &= K_k\boldsymbol{z}_k \\ P_k &= (I - K_k H_k)P_{k|k-1} \end{aligned} \tag{42}$$

The measurement covariance matrix, R_k, is a diagonal matrix with variance terms defined based upon the median star position uncertainty and star magnitude defined in the Hipparcos catalog. Using the EKF update equations, the new estimates can be obtained using

$$\begin{aligned} \boldsymbol{q}_k &= 2\Delta\boldsymbol{\theta}_k \otimes \boldsymbol{q}_{k|k-1} \\ \boldsymbol{\omega}_k &= \boldsymbol{\omega}_{k|k-1} + \Delta\boldsymbol{\omega}_k \end{aligned} \tag{43}$$

where the $\otimes$ operator denotes quaternion composition. This algorithm is repeated for each new measurement obtained from the star tracker.

2.5 ICESat Attitude Determination Implementation

Precision attitude determination for ICESat was performed using the methods described in the sections *The Attitude Determination Problem* and *Extended Kalman Filter*. A general outline of the process is shown in Figure 4.

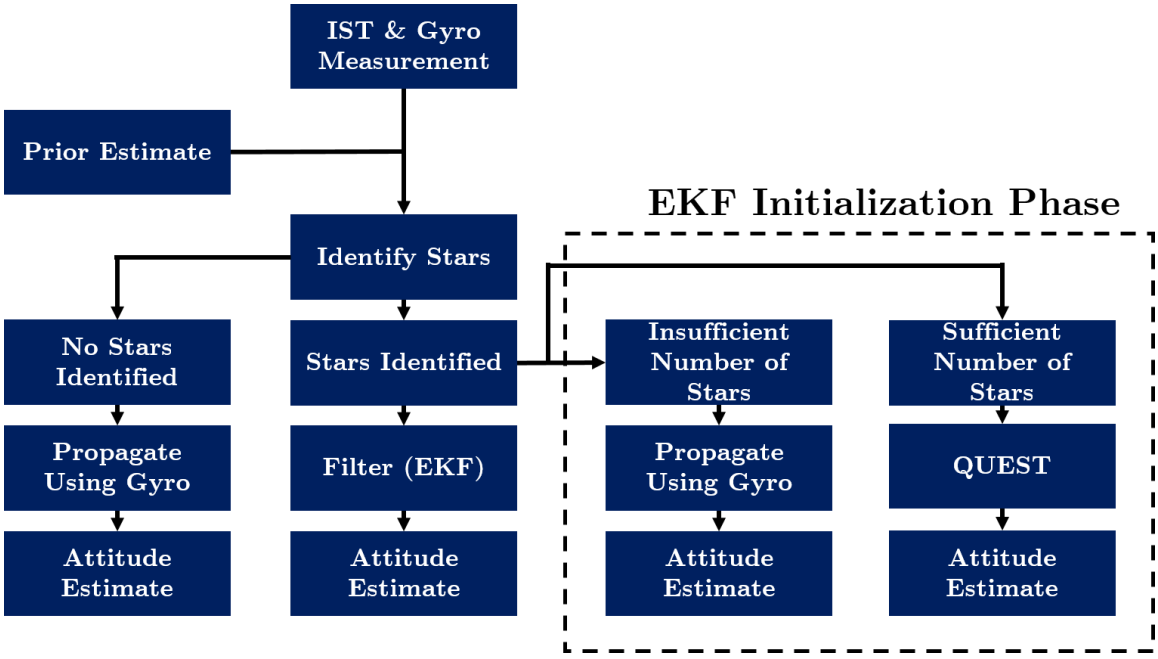

Figure 4: Outline of the precision attitude determination algorithm. The EKF initialization phase is implemented after periods of blinding. The filter is considered initialized after nine consecutive quaternions are generated using QUEST. A sufficient number of stars identified is defined as greater than or equal to four stars.

To prevent poor measurements from being used in the EKF and corrupting the estimate, an initialization phase was incorporated into the algorithm. Star measurements were only passed to the filter if at least nine consecutive CCD frames

containing successfully identified stars were observed prior. Furthermore, these frames were only included in this count if four or more stars were identified within the frame. During this initialization phase, attitude estimates were derived entirely from QUEST. In the absence of stars, the quaternions were propagated purely using the gyroscope rates. Because gyroscope bias is only estimated through the EKF, when the EKF is not being used to filter incoming measurements, quaternions are propagated with gyroscope rates that have not been adjusted to compensate for variations in the rate bias. This implementation resulted in less robust attitude estimates following periods of star tracker blinding. This feature of the attitude determination algorithm is important to consider when using the attitude estimates to model additional phenomena such as star tracker distortion.

2.6 Star Tracker Error Sources

Star tracker attitude determination error primarily stems from the following sources: hardware parameters, noise, centroiding algorithms, star catalog uncertainties, and distortion. Hardware parameter errors such as focal length error and principal point offsets are mostly corrected using factory preset calibrations[5]. The noise in unit vector generation, referred to as noise equivalent angle, is also quantifiable and is measured and calibrated prior to launch. Typically, these effects on attitude determination can be mitigated through use of an EKF. Centroiding algorithms have become very sophisticated and have achieved accuracy in the range of thousandths of a pixel[21]. The accuracy of ICESat's centroiding algorithm is at the 0.1 pixel level, but is also dependent on star magnitude[4]. Star catalogs are derived from ground and spacecraft observations. When measured stars are

compared to the catalog for identification, corrections are applied to mitigate the effects of aberration, proper motion, and parallax. ICESat used the Hipparcos star catalog, which provides a median precision of star position and brightness of 0.77 milliarcseconds and 0.0015 magnitude respectively[4]. As such, the star catalog is an effective representation of truth.

The existence of "bad stars" can contribute to observed distortion through misidentification and centroiding ambiguity. Near neighbor stars can result in changes in observed magnitude which may inhibit proper identification or even shift the true position of the centroid of the identified star. Variable stars, which experience periodic fluctuations in brightness, can also cause identification issues if they are not well-defined. To reduce the likelihood of using such stars for attitude determination, some authors choose to blend stars or exclude them entirely[22]. In the case where available stars are sparse due to limitations of the star tracker magnitude sensitivity or the size of the FOV, eliminating stars may not be desirable or even possible. Blending of stars is another approach to addressing this problem without significantly reducing the stars available for identification. By combining the magnitude and position properties of near neighbor stars such that they can be expressed in the star catalog as a single pseudo-star, the ambiguity of the centroid no longer poses a problem in obtaining a precise attitude quaternion.

Distortion encompasses all higher order errors that are not corrected in the calibration process which include optical effects, warping of the CCD detector surface, temperature effects, and even errors in calibration[5]. Furthermore, anything that induces a deviation in star position from the ideal pinhole camera model can be considered distortion[12,13]. Some authors choose to categorize star tracker

distortion as temporal, high spatial frequency, and low spatial frequency error based upon features of the power spectral density of the star tracker position noise[22,23]. Temporal errors are star tracker errors that change with time, such as the distortion associated with changes in dark current[‡]. High spatial frequency errors are characterized by changes in error on the order of pixels. Low spatial frequency errors are systematic and can be modeled and removed in post-processing. Using a model of the star tracker distortion, corrections can be applied to observed star vectors, effectively calibrating the star tracker using data obtained in flight. These calibrated star unit vectors can then be used to compute improved attitude estimates following the procedure described in prior sections. The methods presented in the next section are implemented to model and characterize the low spatial frequency errors in the ICESat IST.

[‡]Dark current is the leakage current characteristic to semiconductors where electrons possess sufficient thermal energy to break free from the silicon lattice and are accumulated as signal even in the absence of light[28].

Chapter 3: Star Tracker Distortion Estimation

Distortion models for optical sensors have been proposed for a wide variety of applications. In principle, these models all strive to accomplish the same goals of modeling and correcting for distortion in the image captured by the CCD or CMOS sensing array. In photogrammetry, distortion is often distinguished as radial and tangential. The radial distortion can be described by a lookup table derived from test data or by a model employing an odd-ordered polynomial basis function of radial distance from the principal point of symmetry[24]. Tangential distortion is also referred to as decentering distortion because it is induced by the rotational asymmetry of the lens. It is typically only significant in cameras with variable focus or zoom. In the field of optics, lens aberration models encompass any order of radial distance from the principal point. Distortion is considered one of five categories of lens aberration, which also include spherical, coma, astigmatism, and field curvature[24]. Most models used today are derived from those proposed in photogrammetry applications and classical optics and as such tend to favor the radial polynomial distortion model approach. For sensors where traditional optical aberrations are not the only sources of distortion, using a radial basis function for distortion may be too restrictive. The assumed radial symmetry would not capture localized higher order distortion that may be present. Using a more generalized polynomial distortion model based on horizontal and vertical positions in the focal plane, any distortion that does not follow a radial trend will become evident in the distortion map. Sinusoidal basis functions have also been proposed as a possible model for estimating distortion[25].

3.1 Star Tracker Distortion Models

In star tracker specific distortion models, in addition to the problem of choosing a model for the distortion, the decision of whether to incorporate attitude knowledge into estimating the distortion must also be considered. In attitude *independent* methods, the distortion is characterized by the difference between the catalog star distance and the observed star distance between two stars, computed using the equation,

$$\begin{aligned} \delta_h &= (h_2 - h_1) - \left(h_{2,CRF} - h_{1,CRF}\right) \\ \delta_v &= (v_2 - v_1) - \left(v_{2,CRF} - v_{1,CRF}\right) \end{aligned} \tag{44}$$

The h and v terms correspond to horizontal and vertical position in the focal plane. The numbers in the subscripts distinguish between the two stars observed. The CRF subscript denotes that the position is derived from the star catalog and is not the position observed in the star tracker focal plane. In this method, no basis function is assumed and distortion values are computed directly. The FOV is divided into grids and an average distortion is computed for each grid. The distortion value is assigned to the grid where the star corresponding to (h_1, v_1) is located, while the opposite distortion value is assigned to the grid containing (h_2, v_2). The average is computed by summing the distortion values for an individual grid and dividing by the number of stars observed in the grid according to the equations

$$d_h = \frac{\sum_1^N \delta_h}{N}$$
$$d_v = \frac{\sum_1^N \delta_v}{N} \tag{45}$$

The method is considered attitude independent because knowledge of attitude is unnecessary after the stars have been identified. In attitude *dependent* methods, the distortion is derived from the difference between the unit vectors of the mission catalog star and the observed star. The attitude is used to build the rotation matrix to bring the mission catalog star position from the CRF to the SCF[12]. Because the star tracker output directly contributes to the attitude solution, distortion presented in the star tracker will also manifest as errors in the rotation matrix. This recursive relationship indicates that multiple iterations of estimation and correction are necessary to fully eliminate the effects of star tracker distortion on the attitude estimate[5]. The chosen model can be used to describe the full FOV in a global estimate of distortion or be used to define a subsection of the FOV in a localized estimate. Dividing the FOV into overlapping regions allows for the modeling of highly irregular distortion without requiring a significant increase in the order of the basis function. The use of averaging functions can ensure continuity of the distortion model across the FOV. A least squares approach is a common method of estimating the distortion coefficients of the basis function in star tracker applications.

A localized attitude dependent approach was the chosen method for analyzing the distortion in the ICESat IST. Only the first iteration was considered in analyzing distortion characteristics. The localized method was chosen primarily

because the resulting smoothness of the distortion map allows for a qualitative comparison between campaigns and better represents a real-world physical star tracker distortion. Although attitude independent methods would highlight the existence of bad pixels in the detector more effectively, in the analysis of the broader distortion trends this feature is not a necessity. A comparison of distortion maps generated using an attitude independent and attitude dependent method are shown in Figure 5[12]. The maps are generated using three days of data from campaign L2a. The attitude independent and dependent distortion maps share similar features. A smoothing effect is evident in the attitude dependent distortion maps. The maps illustrate the distortion estimated over the full 8°×8° FOV.

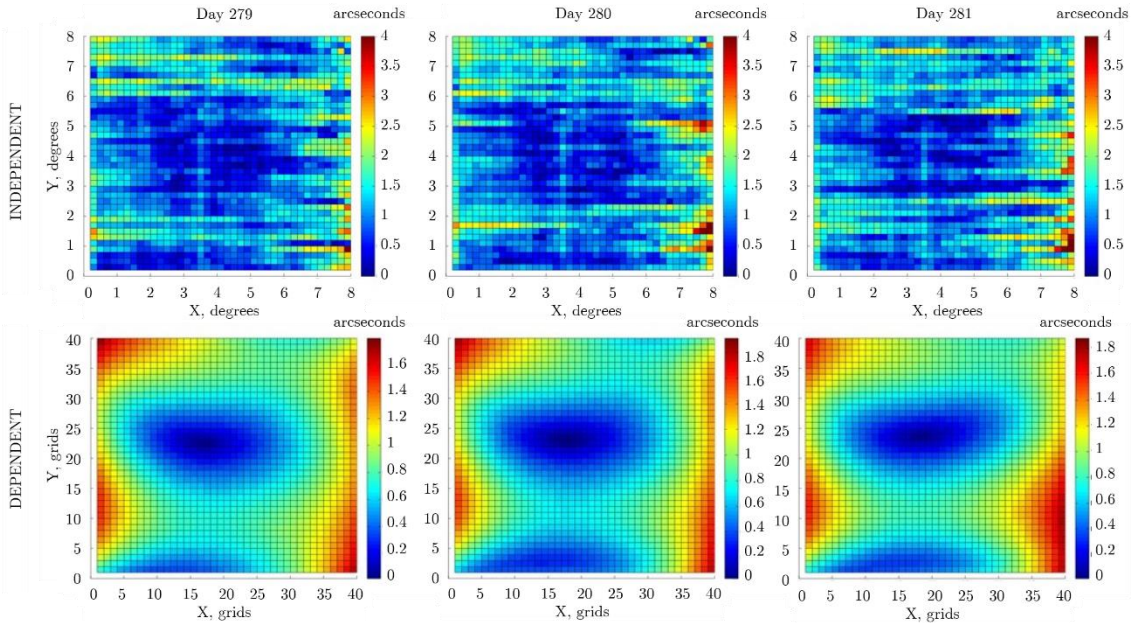

Figure 5: Comparison of distortion maps generated from three days of data from campaign L2a using an attitude independent and attitude dependent method. The top three maps were generated using an attitude independent method, whereas the bottom three were generated using an attitude dependent method.

3.2 Localized Attitude Dependent Distortion Estimation

The order of the basis function and number of grids used to partition the FOV was chosen by comparing a map generated using highly localized 0th order polynomial basis functions with maps generated using different orders of less localized polynomial basis functions. It was found, by trial and error, that a third order polynomial basis function and a FOV partitioned into 16, $2^{\circ}\times2^{\circ}$ grids yielded the best result, given the similar features in the maps generated from each model. The comparison of these two distortion maps is shown in Figure 6[12].

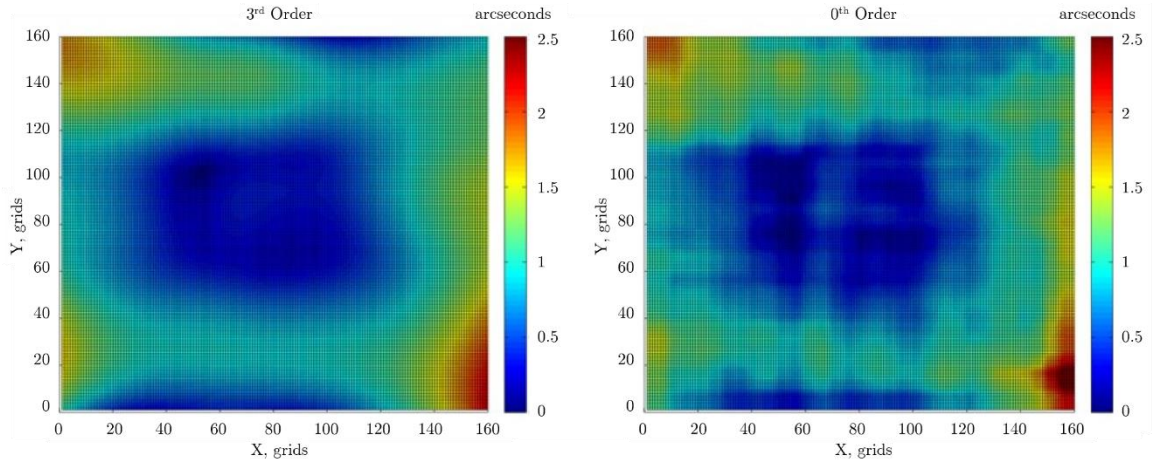

Figure 6: Comparison of distortion maps generated using a 0^{th} order polynomial basis function and a FOV partitioned into 1024, $\frac{1}{4}^{\circ} \times \frac{1}{4}^{\circ}$ grids and a 3^{rd} order polynomial basis function and a FOV partitioned into 16, $2^{\circ} \times 2^{\circ}$ grids. The 3^{rd} order map is on the left and the 0^{th} order map is on the right.

The third order basis function used to model distortion is given by the polynomial

$$\tilde{\mathbf{\Phi}} = [1 \quad h \quad v \quad h^2 \quad hv \quad v^2 \quad h^3 \quad h^2v \quad hv^2 \quad v^3] \tag{46}$$

where h and v describe the observed horizontal and vertical coordinates of the star position in the focal plane[5,12,25]. The observed distortion is defined as

$$\begin{aligned} \delta_h &= h - h_{CRF} \\ \delta_v &= v - v_{CRF} \end{aligned} \tag{47}$$

where h and v are the measured star unit vectors in the SCF and h_{CRF} and v_{CRF} are the star unit vectors corresponding to the catalog positions of the stars rotated from the CRF to the SCF. The matrix rotating the star unit vectors from the CRF to the SCF is derived from the estimated attitude associated with that measurement time. The relationship between the vector of observed distortion represented by d_h and d_v and distortion computed from the model is

$$\begin{aligned} \boldsymbol{d_h} &= \Phi \boldsymbol{a} + \boldsymbol{\epsilon} \\ \boldsymbol{d_v} &= \Phi \boldsymbol{b} + \boldsymbol{\epsilon} \end{aligned} \tag{48}$$

where Φ is the matrix built from the accumulated coordinates of star observations within a region over the period of a campaign, $\boldsymbol{a}$ and $\boldsymbol{b}$ are the column vectors containing the estimated horizontal and vertical distortion coefficients respectively, and ϵ is the error between the observed and modeled distortion[12]. It is assumed the error is described by a zero-mean Gaussian distribution. The distortion coefficients are found using a least squares approach and are given by

$$\begin{aligned} \boldsymbol{a} &= (\Phi^T \Phi)^{-1} \Phi^T \boldsymbol{d_h} \\ \boldsymbol{b} &= (\Phi^T \Phi)^{-1} \Phi^T \boldsymbol{d_v} \end{aligned} \tag{49}$$

The uncertainty in the estimate of the distortion coefficients is analyzed using the covariance matrix given by

$$P = (\Phi^T \Phi)^{-1} \tag{50}$$

where the diagonal terms contain the variance associated with each estimated state.

The 8°×8° FOV was segmented into 16 distinct 2°×2° grids and 9 overlapping 4°×4° regions. This resulted in a total of 20 distortion coefficients estimated over each region, 10 horizontal and 10 vertical, and 180 coefficients over the FOV. Once the distortion coefficients were estimated, the FOV was further broken into 160×160 cells. The distortion for the cells in each region was computed using the third order polynomial functions for both the horizontal and vertical distortion shown in Eq. 48. The weighted distortion is then calculated for each grid using a weighting function to ensure continuity between overlapping regions.

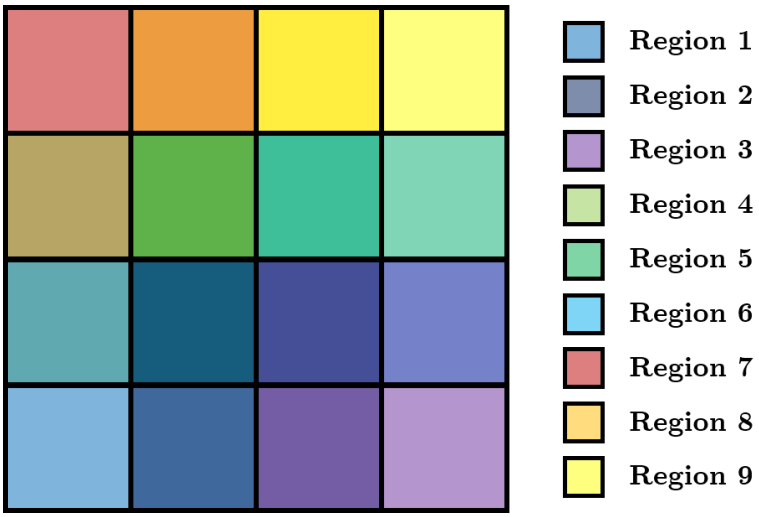

Figure 7: Star tracker FOV partitioned into 16 grids and 9 regions to ensure continuity between localized distortion functions estimated for each region.

The distortion associated with the cells in each grid is computed using a weighted sum of the preliminary distortion for all regions that overlap the grid. This implies that the distortion function for a single grid may be the result of four preliminary distortion functions, such as in the center, two preliminary distortion functions, such as along the edges, or simply defined by its preliminary value, such as in the corners. The weighted distortion is computed according to the equation

$$\begin{aligned} \delta_{x,w} &= \delta_{x,1}w_1 + \delta_{x,2}w_2 + \delta_{x,3}w_3 + \delta_{x,4}w_4 \\ \delta_{y,w} &= \delta_{y,1}w_1 + \delta_{y,2}w_2 + \delta_{y,3}w_3 + \delta_{y,4}w_4 \end{aligned} \tag{51}$$

where the numbers correspond to the preliminary functions starting from the region whose center is defined as the bottom left vertex of the target grid, traveling counter clockwise, and x and y correspond to the position of the cell in the focal plane. The weighting functions are given by

$$\begin{aligned} w_1 &= (1 - w_x)(1 - w_y) \\ w_2 &= w_x(1 - w_y) \\ w_3 &= w_x w_y \\ w_4 &= (1 - w_x)w_y \end{aligned} \tag{52}$$

and the weighting basis functions are given by

$$w_x = x^2(3 - 2x)$$
$$w_y = y^2(3 - 2y) \tag{53}$$

This weighting function method was originally developed for topographical applications, but has been adopted for star tracker distortion applications in existing literature[25]. In the case of only two overlapping regions, the resulting distortion within the grid would only be the weighted sum of two preliminary functions. If the grid is defined by only one region, it retains the preliminary distortion values of the region. This process ensures both continuity in the distortion map across the FOV and improves the estimate by including neighboring data points[25].

The distortion maps used to analyze trends in the ICESat campaigns were generated using the methods described above. Star tracker telemetry was organized such that each output file corresponded to one day of data. Because the star tracker telemetry files spanned the entire ICESat mission, processing the data was performed sequentially, one data file at a time. The quantities $\Phi^T\Phi$, $\Phi^T\boldsymbol{d_h}$, $\Phi^T\boldsymbol{d_v}$ were accumulated for each day in a campaign and summed before computing the estimate of the distortion coefficients. Instead of plotting the estimated distortion at the position of each observed star, the distortion was plotted at uniform points defined by the cell vertices along the horizontal and vertical directions across the FOV.

Chapter 4: Results of Distortion Estimation

Distortion maps were generated using star tracker output for each ICESat laser campaign over the duration of its seven-year mission. The maps were compared to investigate the dependence of distortion on parameters including time, apparent motion of stars across the star tracker FOV, region of the celestial sphere observed, frequency and duration of star tracker blinding events, star tracker temperature, and star color. These properties where chosen for analysis because of their anticipated potential to affect the estimated distortion. The lessons learned from application of this method will be incorporated into the precision attitude and pointing determination process for ICESat-2. Results are further relevant to application on future spacecraft missions that utilize star trackers for the purposes of attitude determination and can be incorporated into calibration or post-processing to reduce uncertainty through mitigation of star tracker distortion.

4.1 Star Tracker Distortion Maps

The distortion maps presented in this section convey the magnitude of distortion across the star tracker FOV. Distortion vector maps are also provided to illustrate the direction of the distortion. The distortion vector corresponds to the vector defined by the horizontal and vertical components of the distortion calculated using the estimated distortion coefficients. Star density maps are shown to convey the distribution of star observations. The star density maps are a color-scaled histogram of star observations defined over the star tracker FOV. Because of hardware calibration errors, some of the observed star positions are defined outside the FOV. These observations are associated with the most adjacent bin

defined inside the FOV for star density map generation. All observations associated with positions outside the FOV are below 0° in either the X or Y direction. The results are organized by campaign, in chronological order. The IST distortion map generated using data from the full mission is presented after the campaign-based distortion maps. A table providing a summary of relevant parameters for each campaign is provided in Appendix 1.

4.1.1 Campaign L1a

Campaign L1a was the first ICESat laser campaign, spanning 38 days. The IST observed 145,352,382 stars during this period. Campaign L1a was unique in that it was the only campaign to be operated in both sailboat mode and airplane mode, although it was only operated in airplane mode for approximately one week[26]. The distortion map, distortion vector map, and star density map generated using the data from this campaign are provided in the figures below.

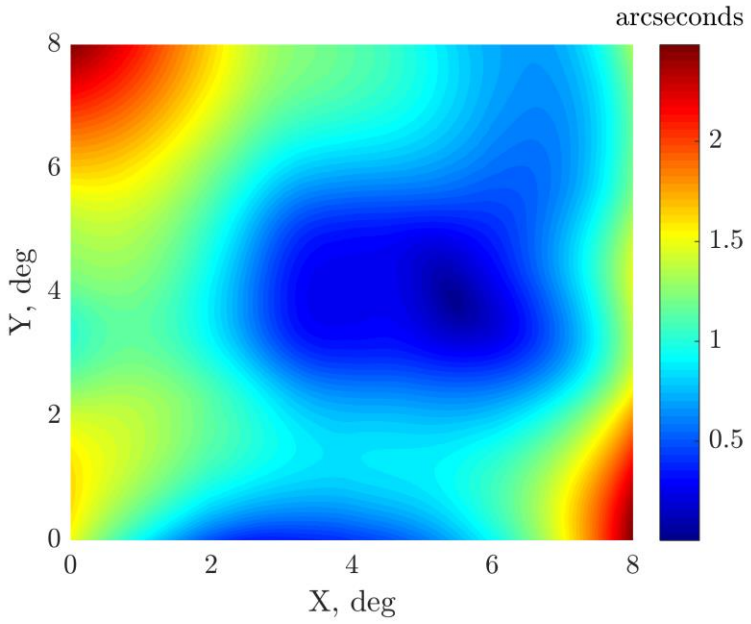

Figure 8: Distortion map for the ICESat IST, generated from observations collected during campaign L1a.

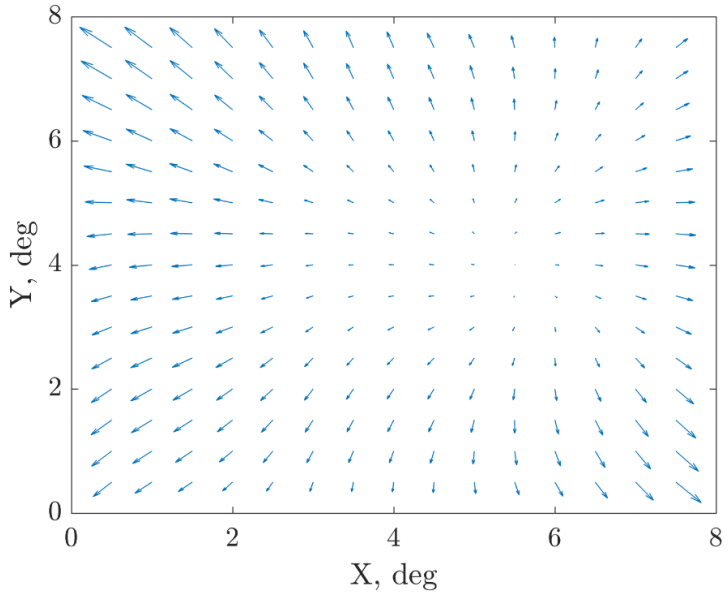

Figure 9: Distortion vector map for the ICESat IST, generated from observations collected during campaign L1a.

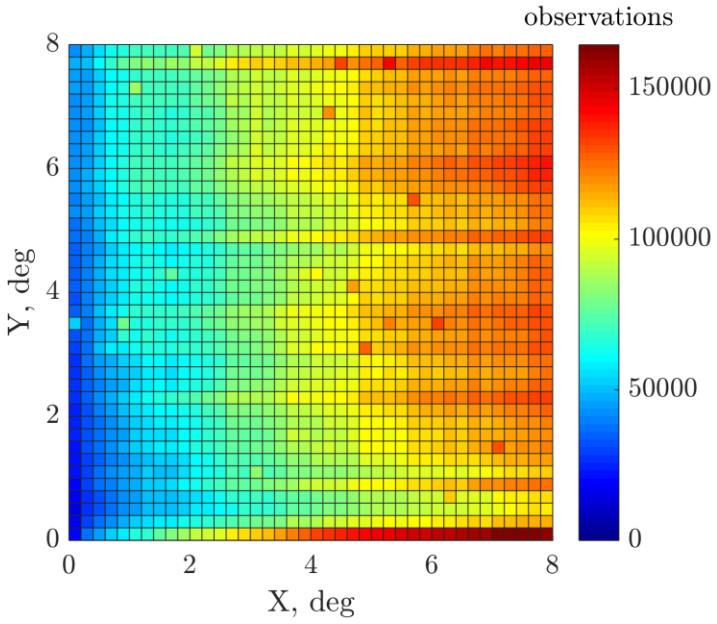

Figure 10: Star density map for the ICESat IST, generated from observations collected during campaign L1a.

4.1.2 Campaign L2a

Campaign L2a was the longest ICESat laser campaign, spanning 55 days. The IST observed 254,282,205 stars during this period. Campaign L2a was operated in (+Y) sailboat mode. The distortion map, distortion vector map, and star density map generated using the data from this campaign are provided in the figures below.

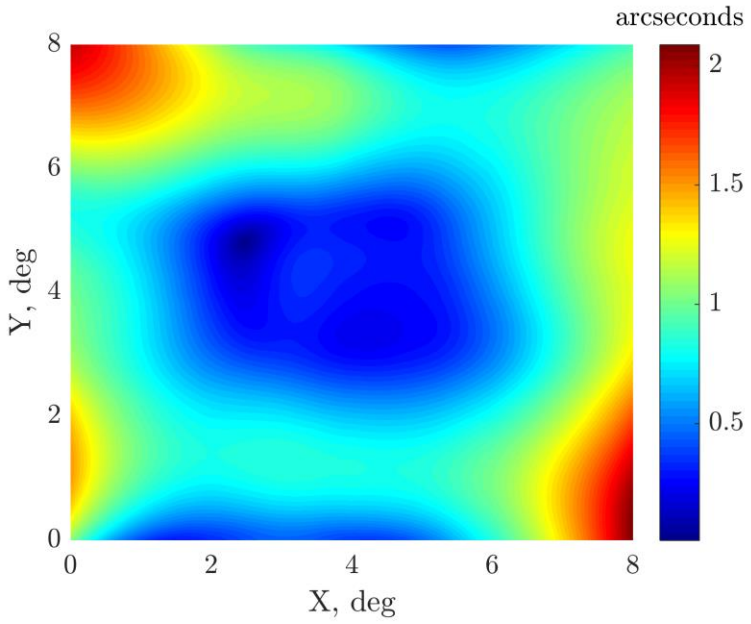

Figure 11: Distortion map for the ICESat IST, generated from observations collected during campaign L2a.

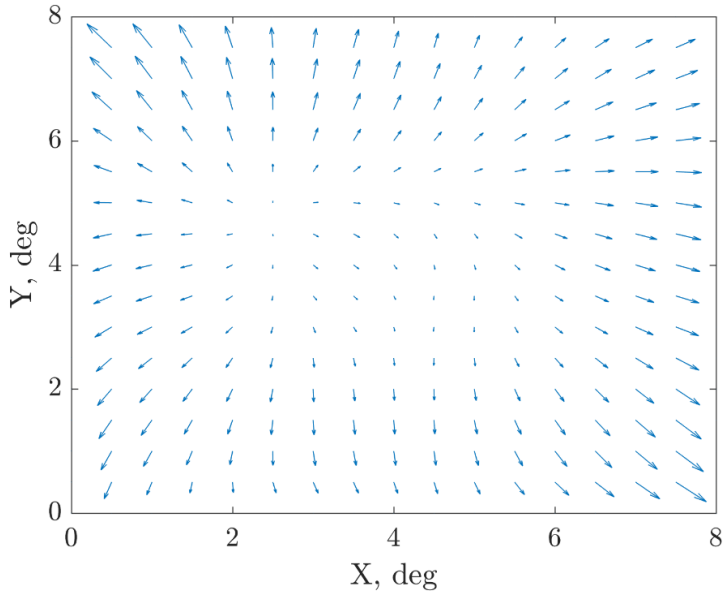

Figure 12: Distortion vector map for the ICESat IST, generated from observations collected during campaign L2a.

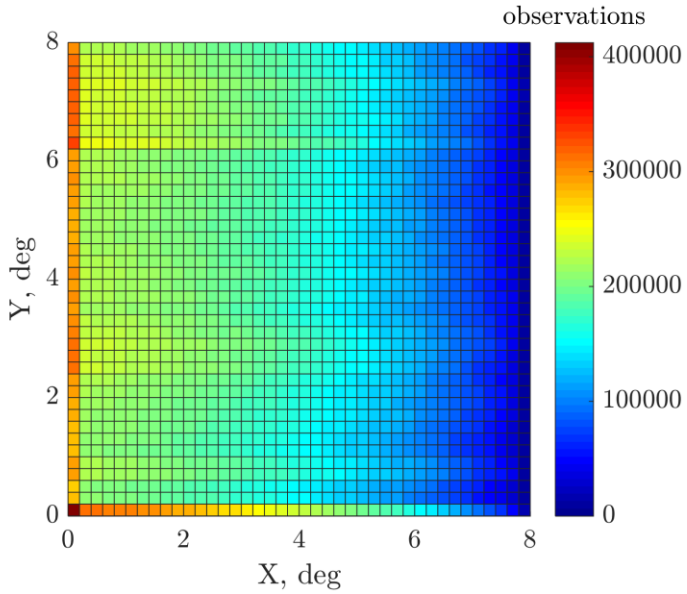

Figure 13: Star density map for the ICESat IST, generated from observations collected during campaign L2a.

4.1.3 Campaign L2b

Campaign L2b spanned 34 days. The IST observed 137,380,590 stars during this period. Campaign L2b was operated in (+Y) sailboat mode. The distortion map, distortion vector map, and star density map generated using the data from this campaign are provided in the figures below. The hot spots visible in the star density map are an artifact of the maneuvers performed by ICESat to achieve targeted altimetry measurements. These maneuvers create areas of higher density observations relative to simple nadir pointing operation.

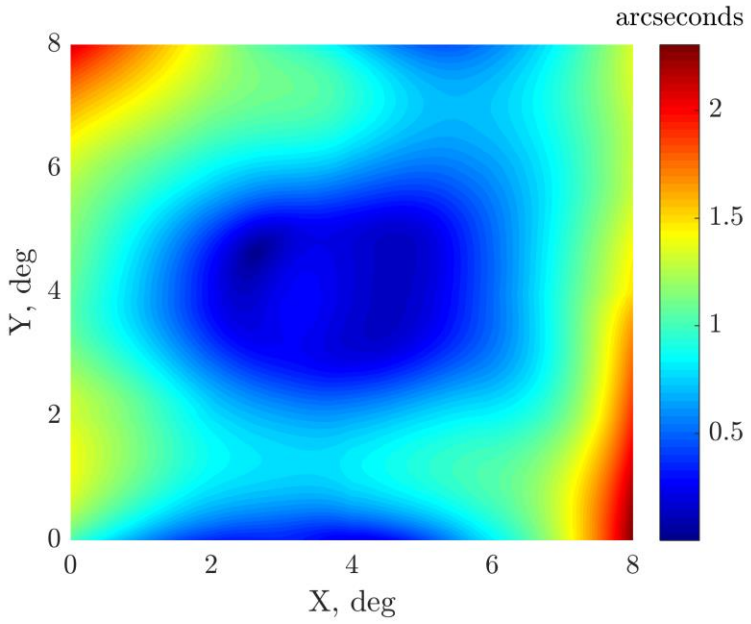

Figure 14: Distortion map for the ICESat IST, generated from observations collected during campaign L2b.

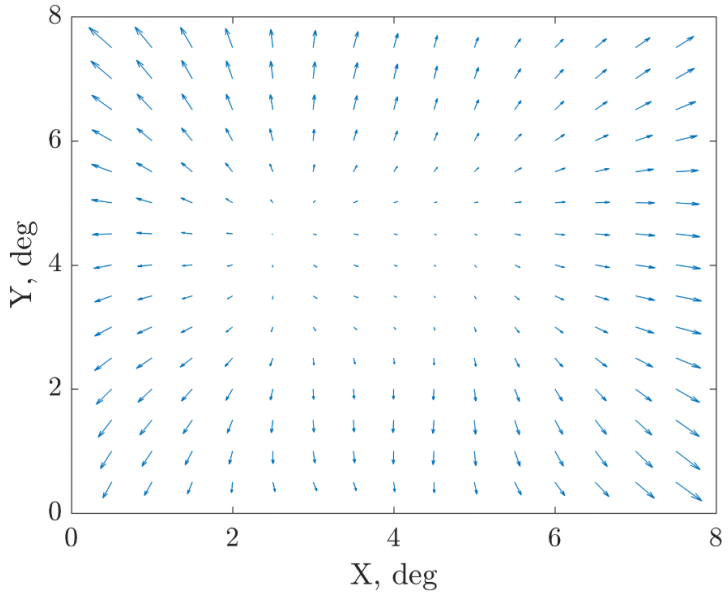

Figure 15: Distortion vector map for the ICESat IST, generated from observations collected during campaign L2b.

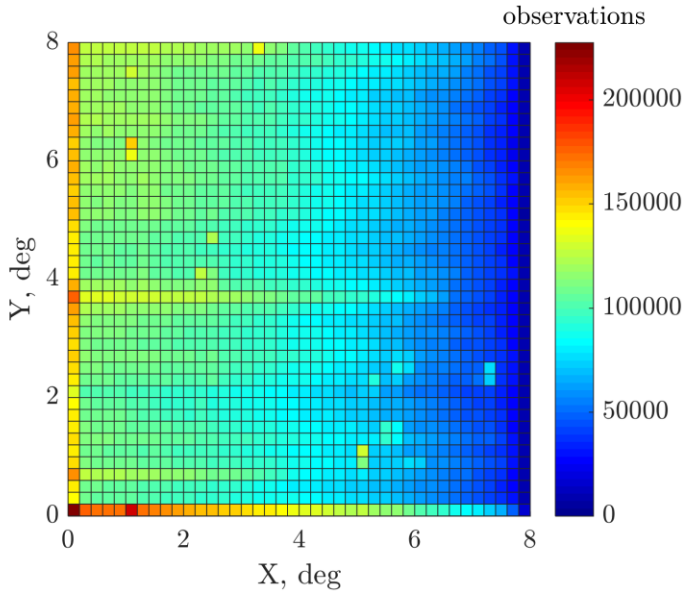

Figure 16: Star density map for the ICESat IST, generated from observations collected during campaign L2b.

4.1.4 Campaign L2c

Campaign L2c spanned 35 days. The IST observed 135,654,382 stars during this period. Campaign L2c was operated in (-X) airplane mode. The distortion map, distortion vector map, and star density map generated using the data from this campaign are provided in the figures below. The high distortion estimated in this campaign is not representative of systematic star tracker distortion, but is rather an artifact of the attitude solution used to generate the distortion observation. This will be explained in the later section, *Effects of Blinding on Distortion*.

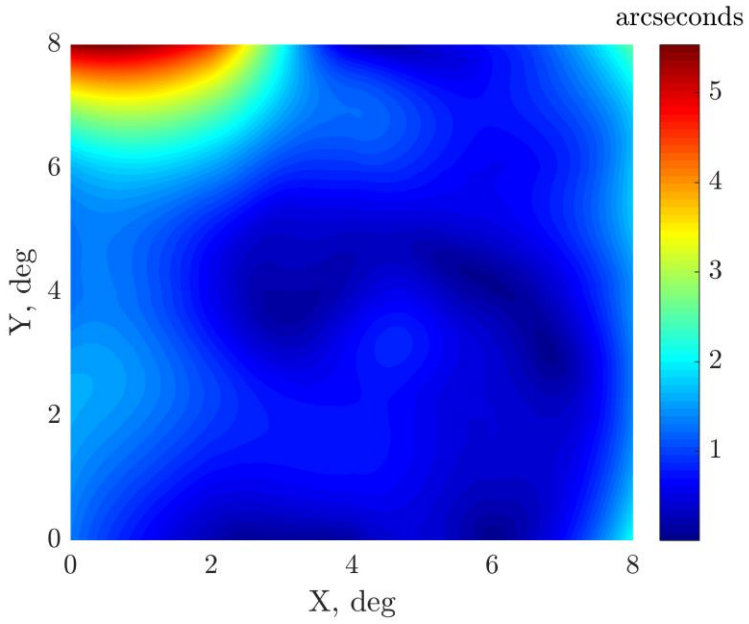

Figure 17: Distortion map for the ICESat IST, generated from observations collected during campaign L2c.

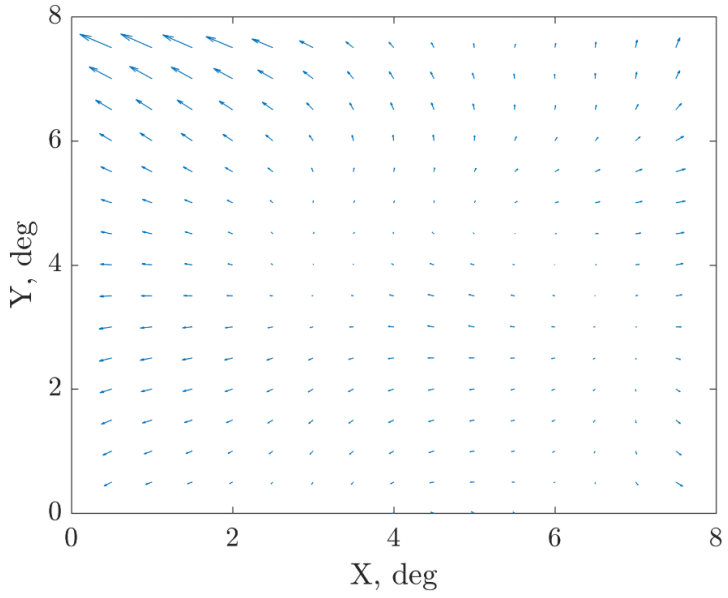

Figure 18: Distortion vector map for the ICESat IST, generated from observations collected during campaign L2c.

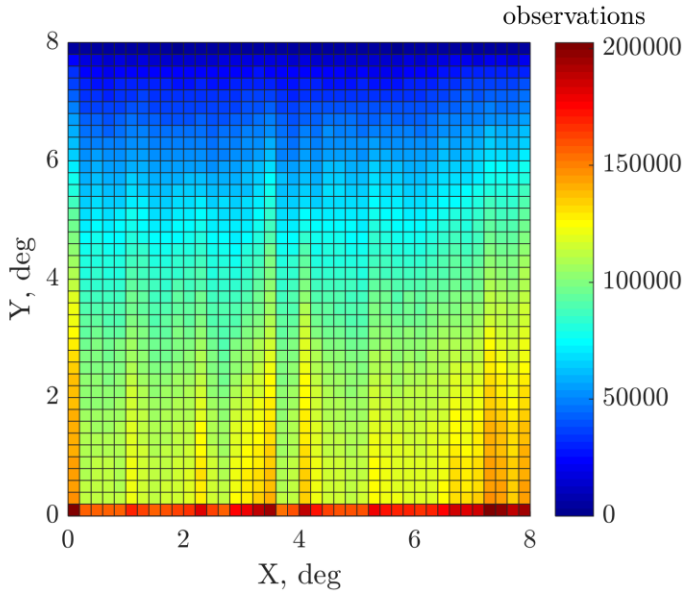

Figure 19: Star density map for the ICESat IST, generated from observations collected during campaign L2c.

4.1.5 Campaign L3a

Campaign L3a spanned 37 days. The IST observed 161,387,262 stars during this period. Campaign L3a was operated in (-Y) sailboat mode. The distortion map, distortion vector map, and star density map generated using the data from this campaign are provided in the figures below.

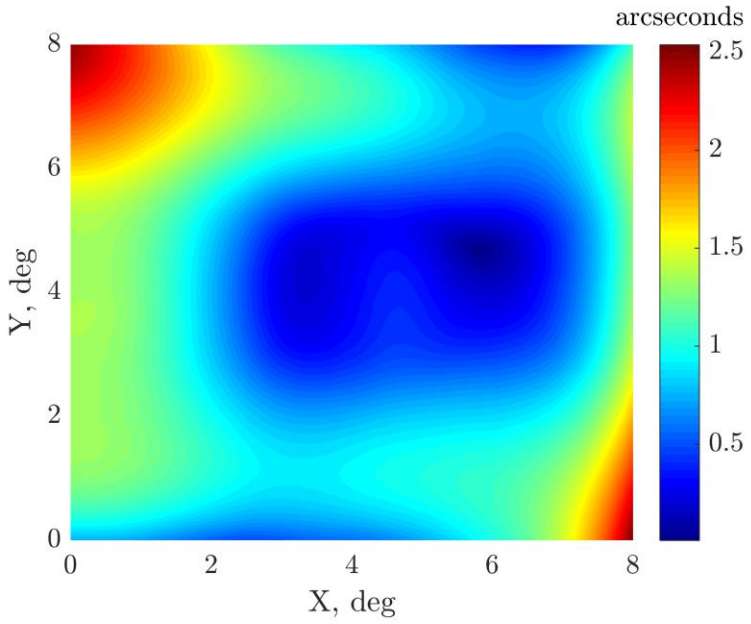

Figure 20: Distortion map for the ICESat IST, generated from observations collected during campaign L3a.

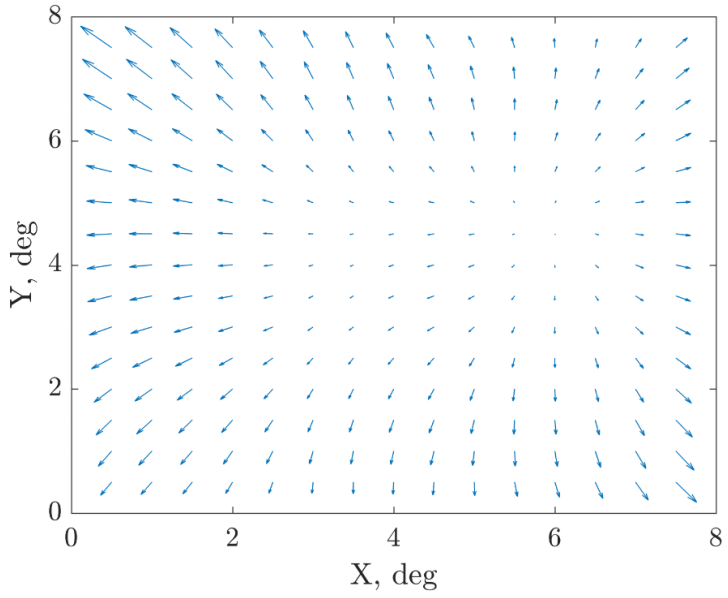

Figure 21: Distortion vector map for the ICESat IST, generated from observations collected during campaign L3a.

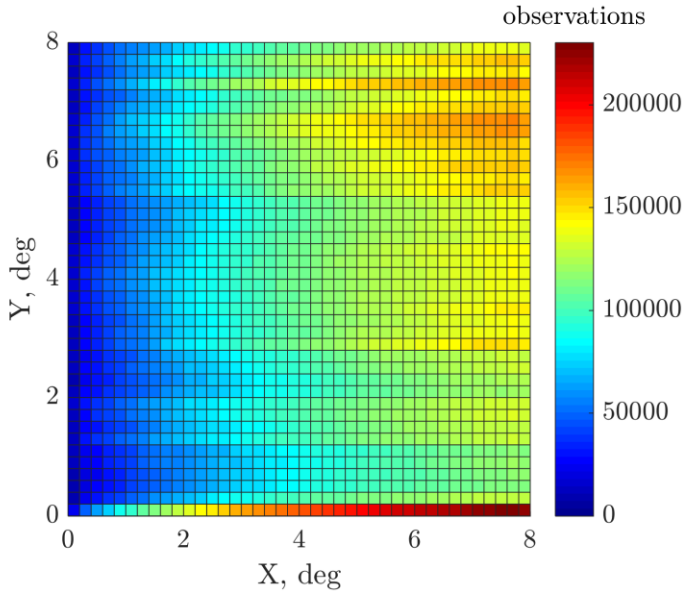

Figure 22: Star density map for the ICESat IST, generated from observations collected during campaign L3a.

4.1.6 Campaign L3b

Campaign L3b spanned 36 days. The IST observed 151,888,368 stars during this period. Campaign L3b was operated in (-Y) sailboat mode. The distortion map, distortion vector map, and star density map generated using the data from this campaign are provided in the figures below.

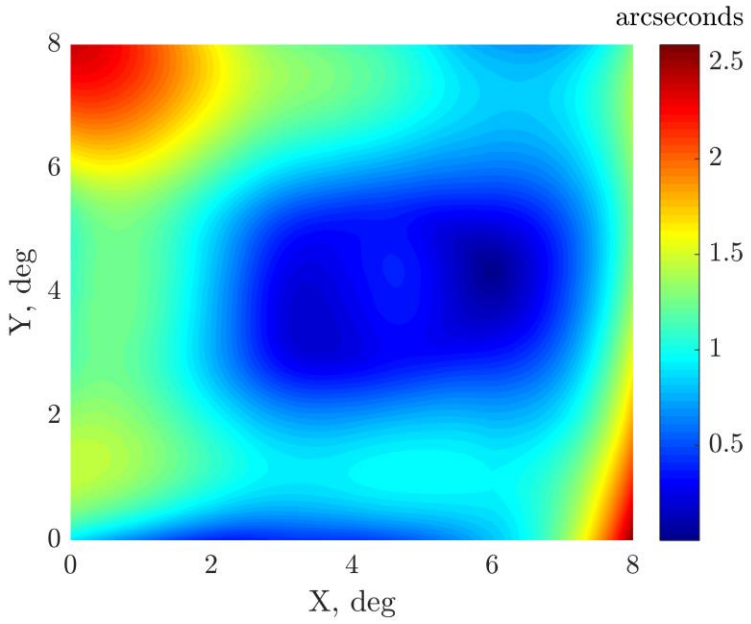

Figure 23: Distortion map for the ICESat IST, generated from observations collected during campaign L3b.

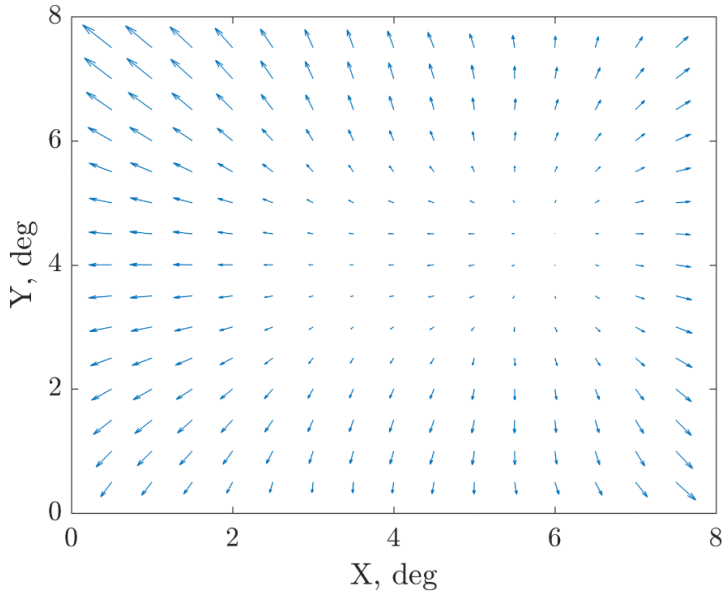

Figure 24: Distortion vector map for the ICESat IST, generated from observations collected during campaign L3b.

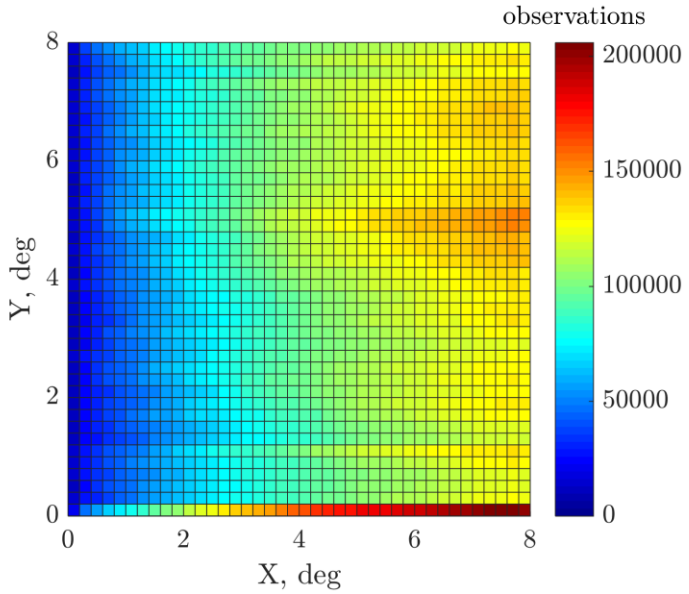

Figure 25: Star density map for the ICESat IST, generated from observations collected during campaign L3b.

4.1.7 Campaign L3c

Campaign L3c spanned 35 days. The IST observed 137,303,074 stars during this period. Campaign L3c was operated in (+X) airplane mode. The distortion map, distortion vector map, and star density map generated using the data from this campaign are provided in the figures below. The unique features in the distortion map for this campaign are primarily artifacts of the attitude solution used to generate the distortion observation, much like campaign L2c. This will be explained in the later section, *Effects of Blinding on Distortion*.

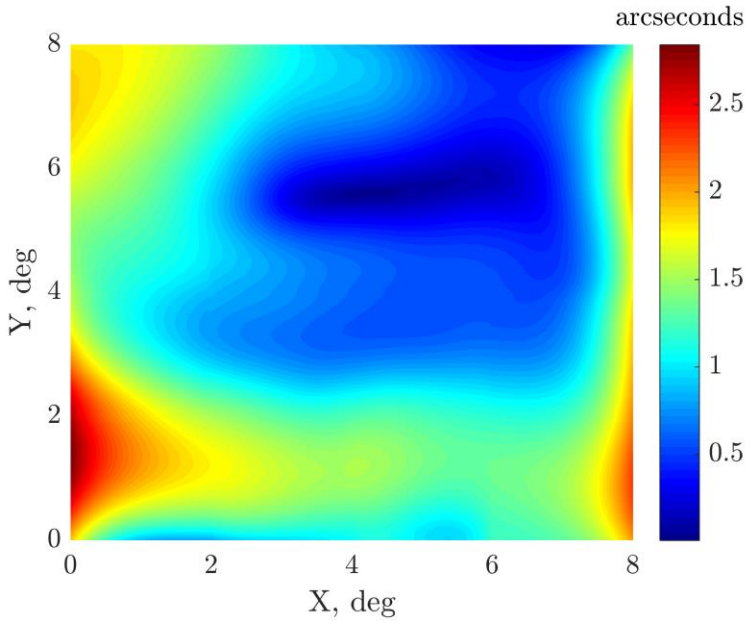

Figure 26: Distortion map for the ICESat IST, generated from observations collected during campaign L3c.

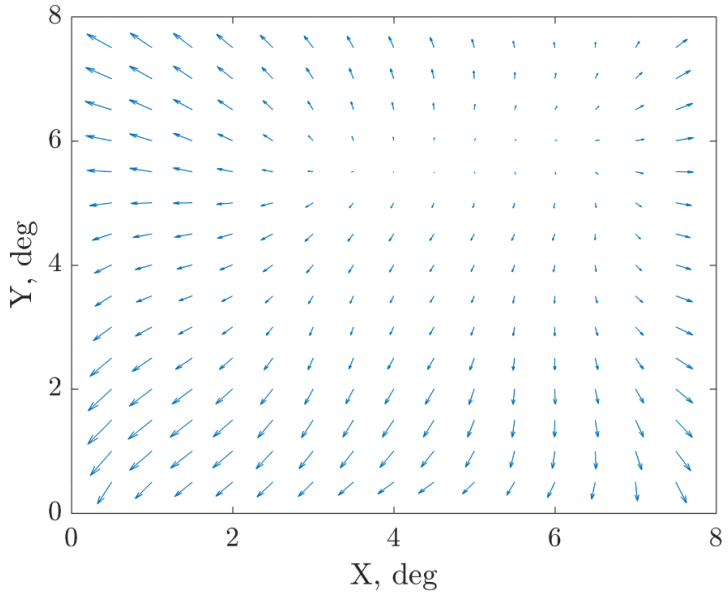

Figure 27: Distortion vector map for the ICESat IST, generated from observations collected during campaign L3c.

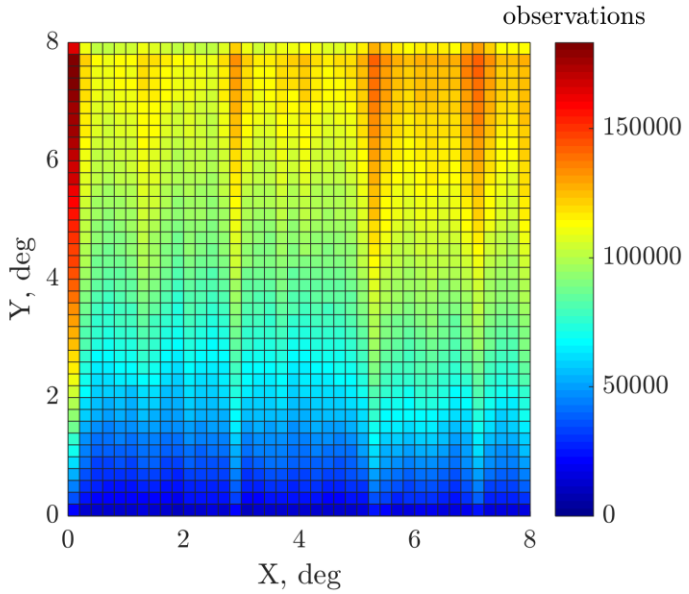

Figure 28: Star density map for the ICESat IST, generated from observations collected during campaign L3c.

4.1.8 Campaign L3d

Campaign L3d spanned 35 days. The IST observed 159,025,723 stars during this period. Campaign L3d was operated in (+Y) sailboat mode. The distortion map, distortion vector map, and star density map generated using the data from this campaign are provided in the figures below.

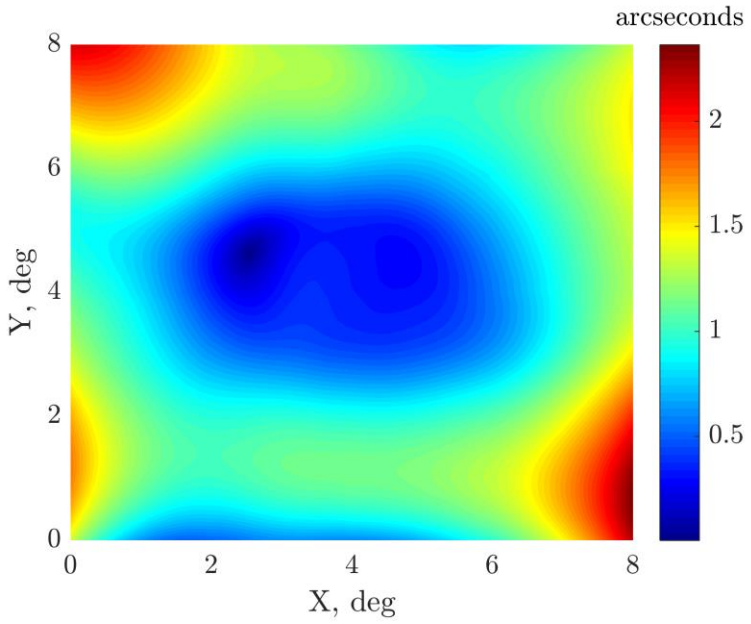

Figure 29: Distortion map for the ICESat IST, generated from observations collected during campaign L3d.

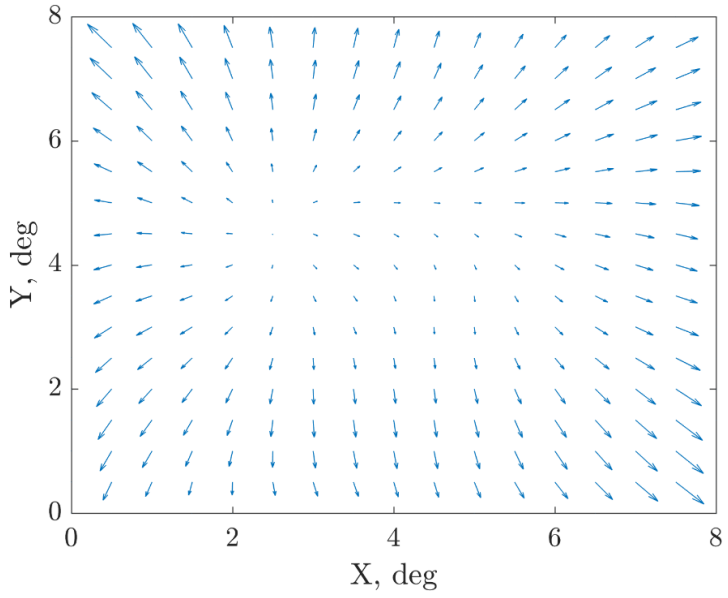

Figure 30: Distortion vector map for the ICESat IST, generated from observations collected during campaign L3d.

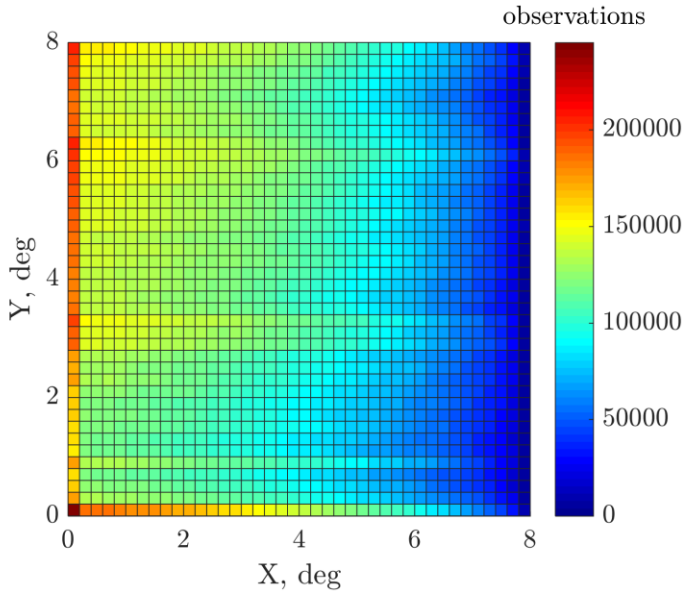

Figure 31: Star density map for the ICESat IST, generated from observations collected during campaign L3d.

4.1.9 Campaign L3e

Campaign L3e spanned 35 days. The IST observed 156,443,642 stars during this period. Campaign L3e was operated in (+Y) sailboat mode. The distortion map, distortion vector map, and star density map generated using the data from this campaign are provided in the figures below.

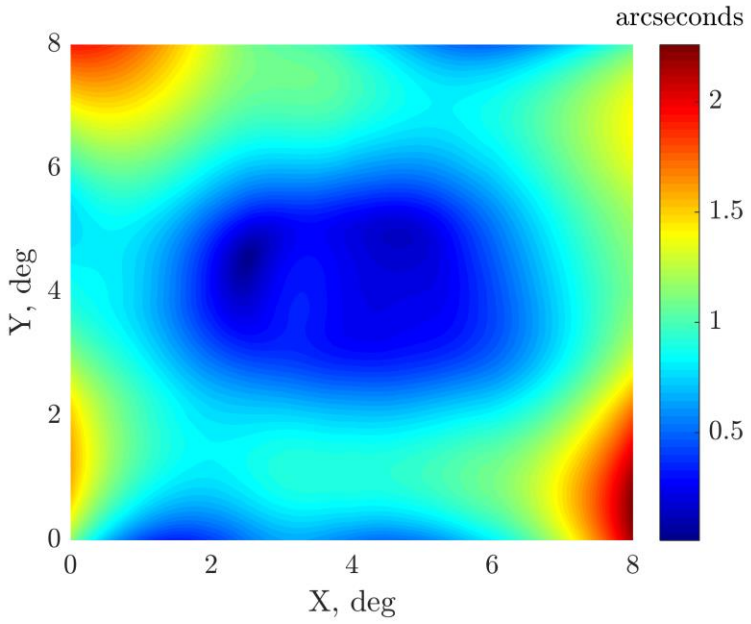

Figure 32: Distortion map for the ICESat IST, generated from observations collected during campaign L3e.

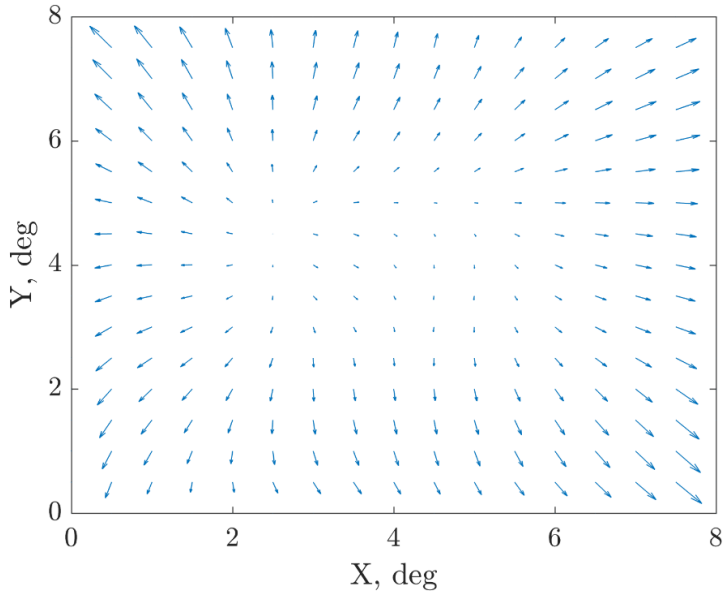

Figure 33: Distortion vector map for the ICESat IST, generated from observations collected during campaign L3e.

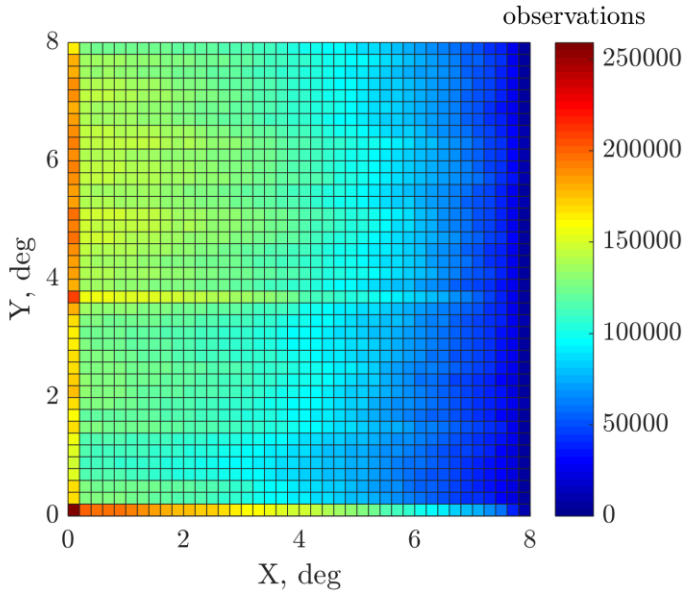

Figure 34: Star density map for the ICESat IST, generated from observations collected during campaign L3e.

4.1.10 Campaign L3f

Campaign L3f spanned 34 days. The IST observed 133,451,338 stars during this period. Campaign L3f was operated in (-X) airplane mode. The distortion map, distortion vector map, and star density map generated using the data from this campaign are provided in the figures below. The distortion map shares features with the distortion map generated from campaign L2c. Once again, the high distortion estimated in this campaign is not representative of systematic star tracker distortion, but is rather an artifact of the attitude solution used to generate the distortion observation. This will be explained in the later section, *Effects of Blinding on Distortion.*

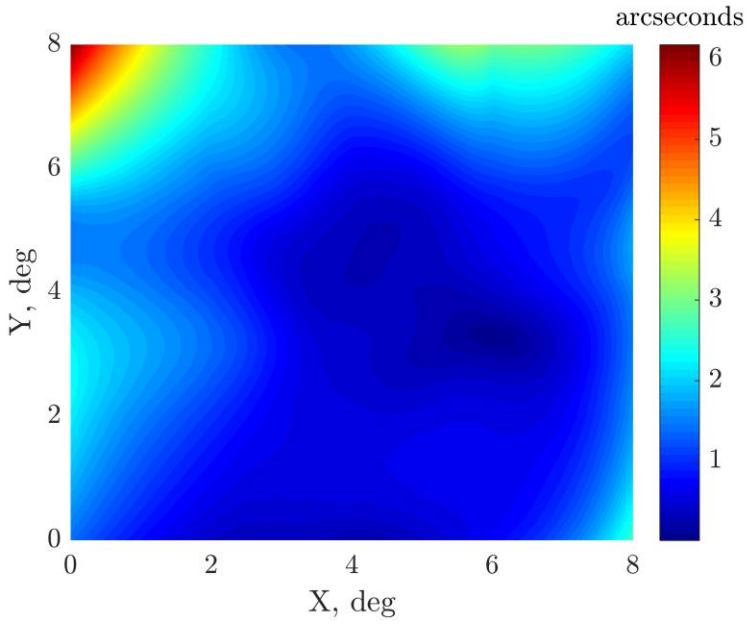

Figure 35: Distortion map for the ICESat IST, generated from observations collected during campaign L3f.

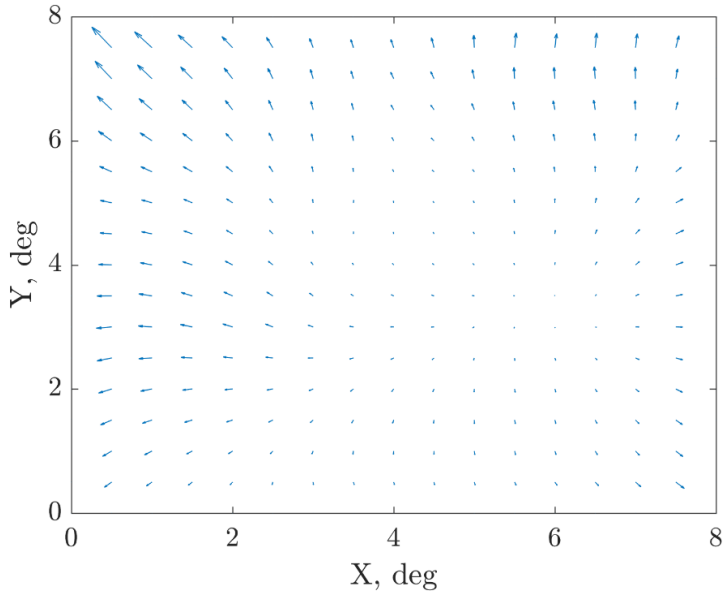

Figure 36: Distortion vector map for the ICESat IST, generated from observations collected during campaign L3f.

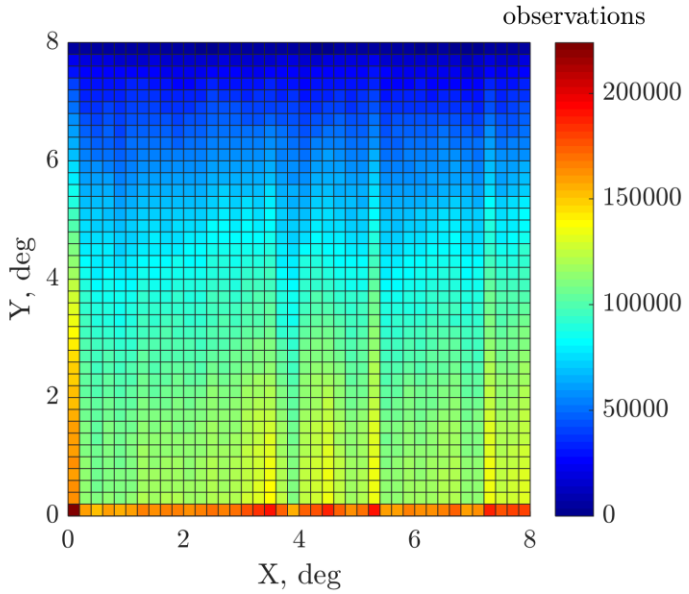

Figure 37: Star density map for the ICESat IST, generated from observations collected during campaign L3f.

4.1.11 Campaign L3g

Campaign L3g spanned 34 days. The IST observed 145,423,157 stars during this period. Campaign L3g was operated in (-Y) sailboat mode. The distortion map, distortion vector map, and star density map generated using the data from this campaign are provided in the figures below.

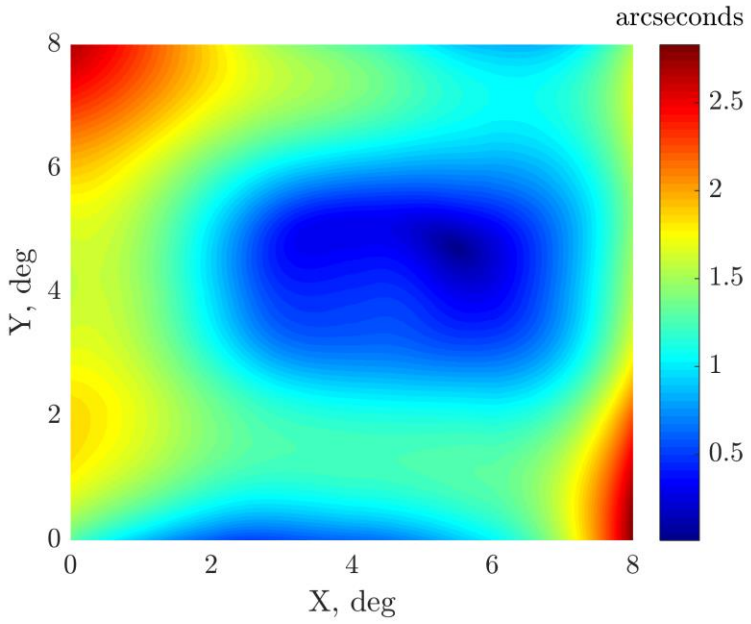

Figure 38: Distortion map for the ICESat IST, generated from observations collected during campaign L3g.

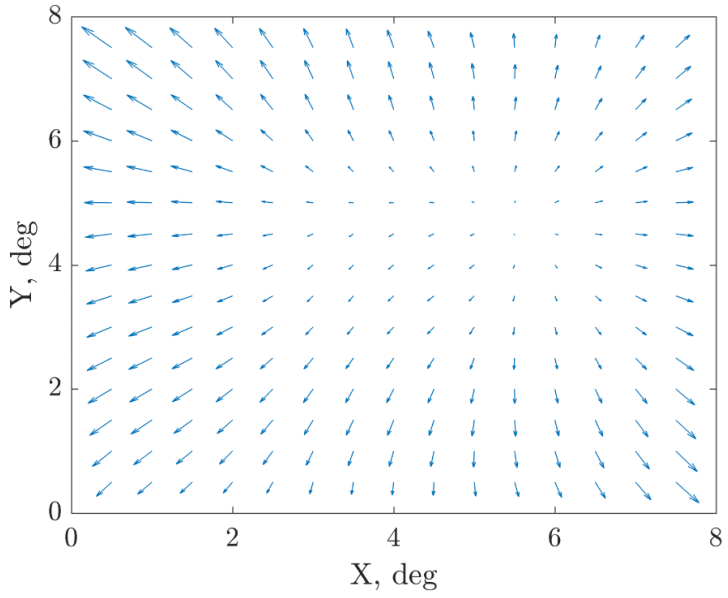

Figure 39: Distortion vector map for the ICESat IST, generated from observations collected during campaign L3g.

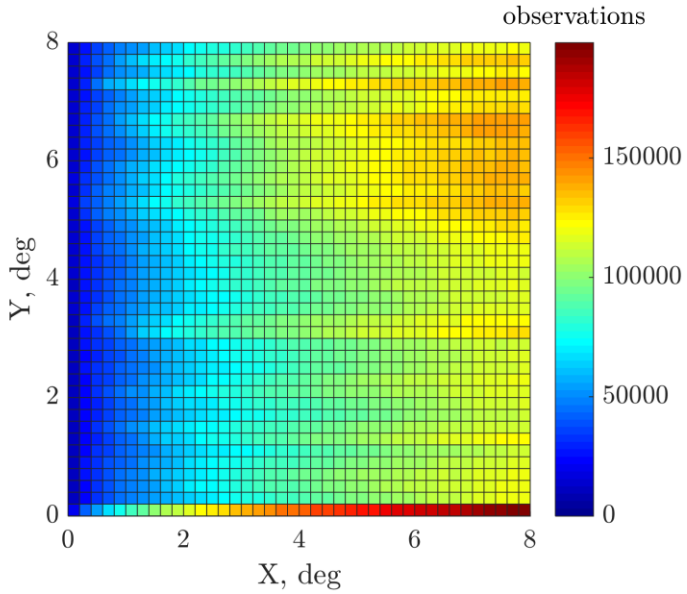

Figure 40: Star density map for the ICESat IST, generated from observations collected during campaign L3g.

4.1.12 Campaign L3h

Campaign L3h spanned 34 days. The IST observed 150,349,948 stars during this period. Campaign L3h was operated in (-Y) sailboat mode. The distortion map, distortion vector map, and star density map generated using the data from this campaign are provided in the figures below.

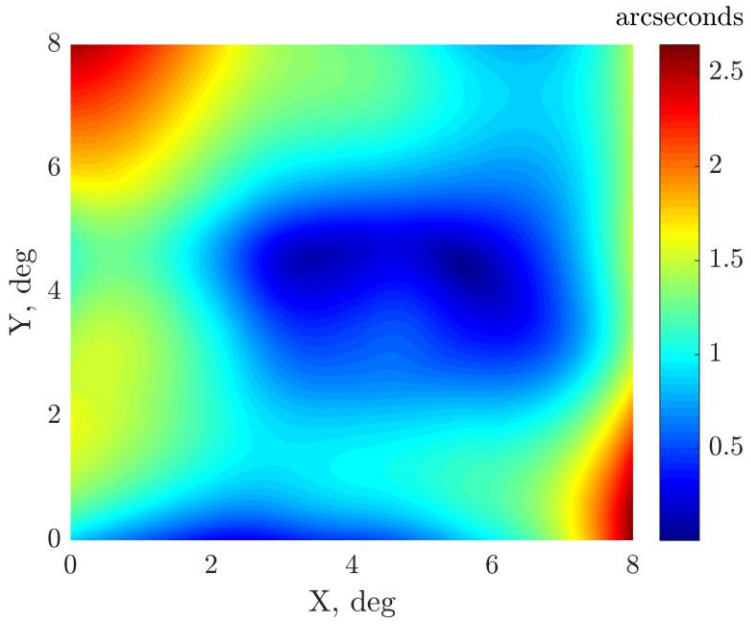

Figure 41: Distortion map for the ICESat IST, generated from observations collected during campaign L3h.

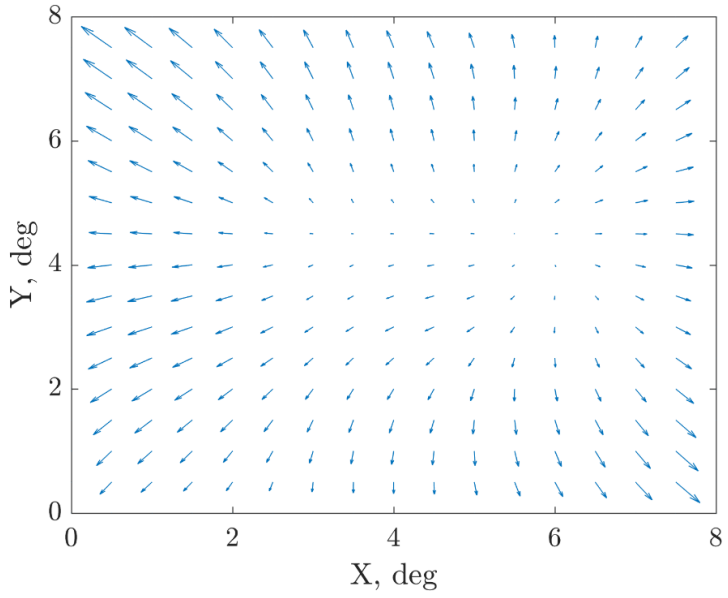

Figure 42: Distortion vector map for the ICESat IST, generated from observations collected during campaign L3h.

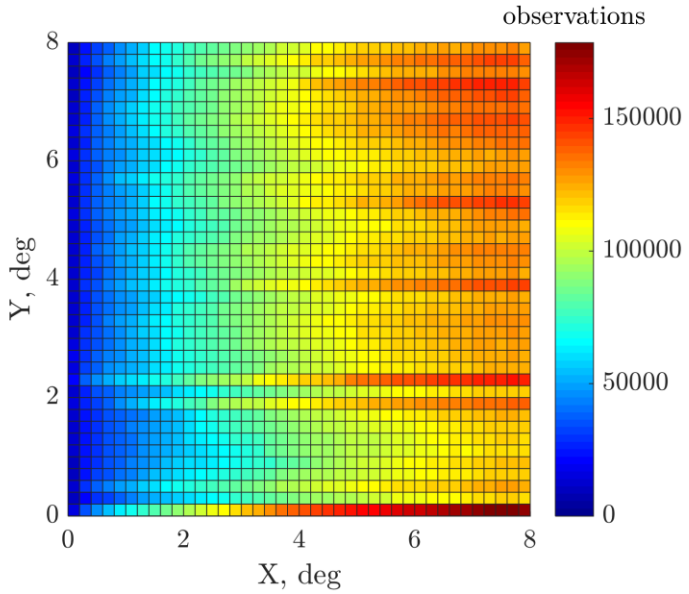

Figure 43: Star density map for the ICESat IST, generated from observations collected during campaign L3h.

4.1.13 Campaign L3i

Campaign L3i spanned 35 days. The IST observed 144,878,058 stars during this period. Campaign L3i was operated in (+Y) sailboat mode. The distortion map, distortion vector map, and star density map generated using the data from this campaign are provided in the figures below.

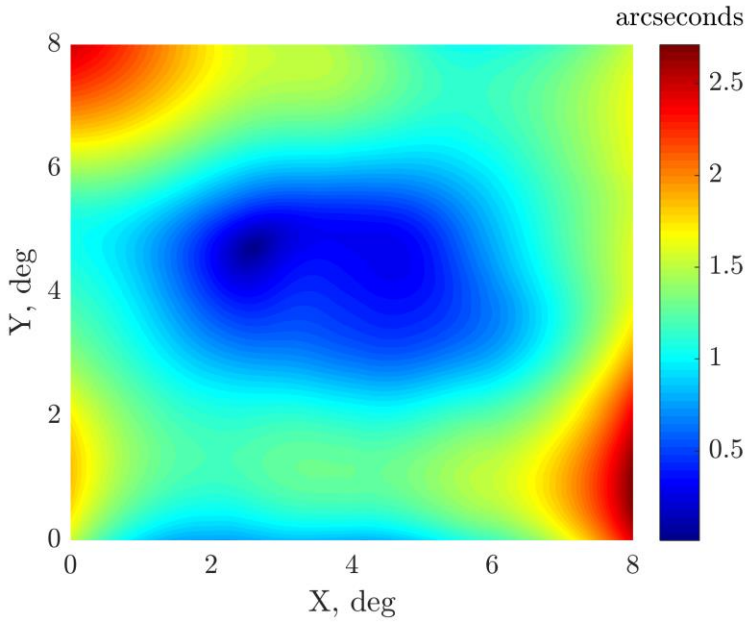

Figure 44: Distortion map for the ICESat IST, generated from observations collected during campaign L3i.

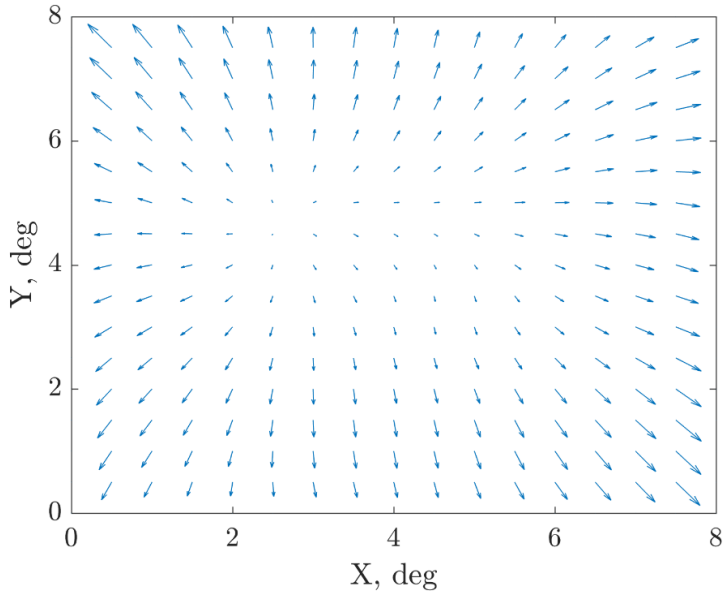

Figure 45: Distortion vector map for the ICESat IST, generated from observations collected during campaign L3i.

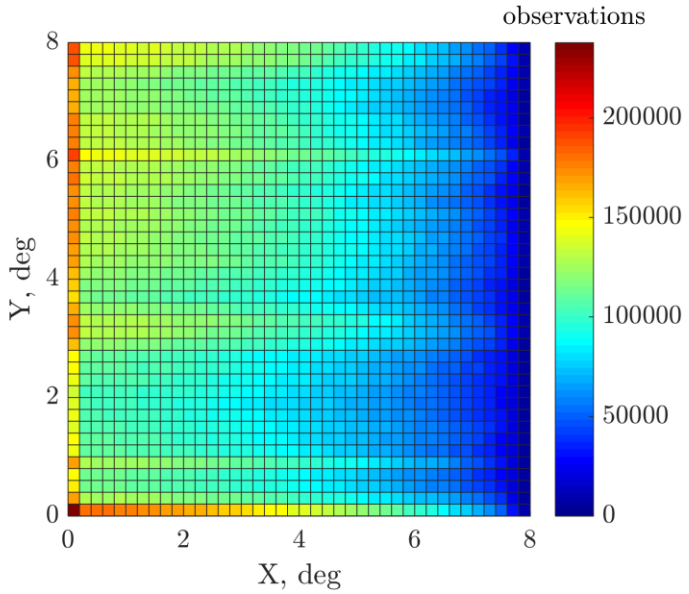

Figure 46: Star density map for the ICESat IST, generated from observations collected during campaign L3i.

4.1.14 Campaign L3j

Campaign L3j spanned 34 days. The IST observed 159,760,021 stars during this period. Campaign L3j was operated in (+Y) sailboat mode. The distortion map, distortion vector map, and star density map generated using the data from this campaign are provided in the figures below.

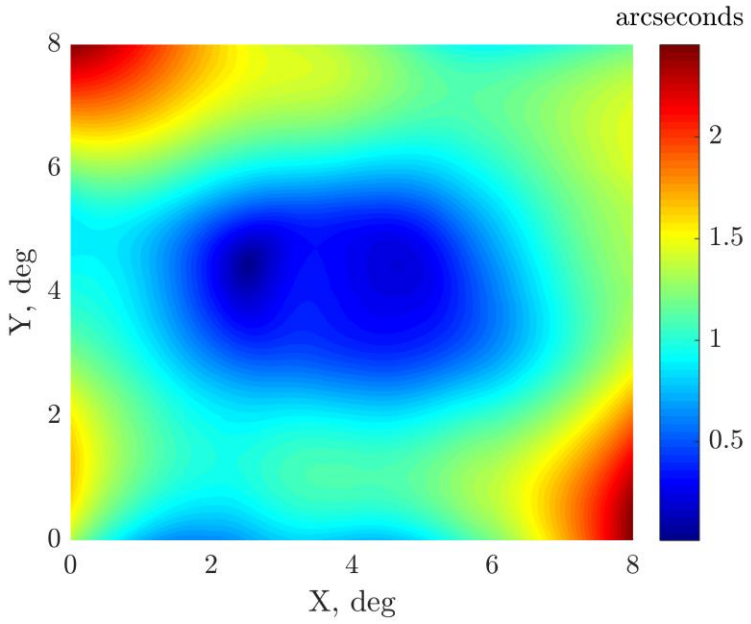

Figure 47: Distortion map for the ICESat IST, generated from observations collected during campaign L3j.

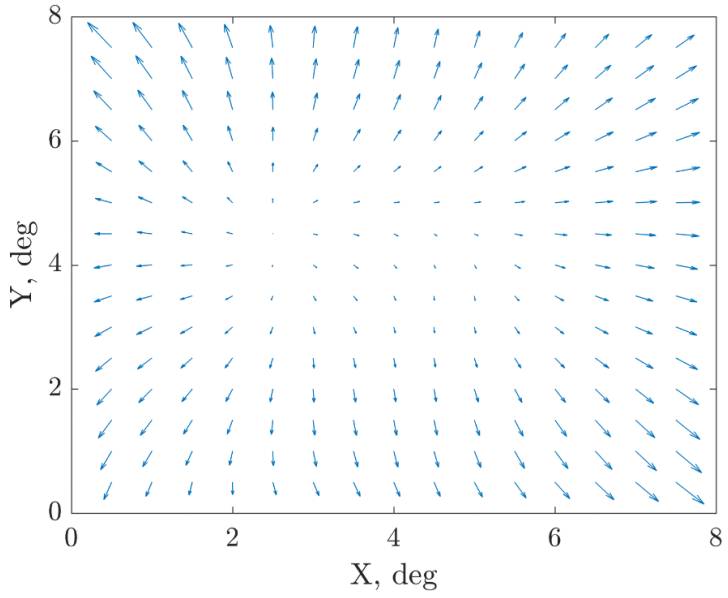

Figure 48: Distortion vector map for the ICESat IST, generated from observations collected during campaign L3j.

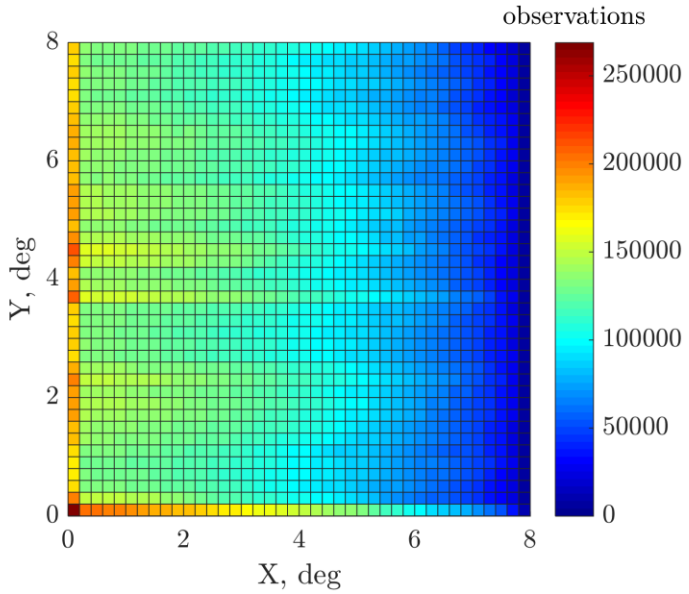

Figure 49: Star density map for the ICESat IST, generated from observations collected during campaign L3j.

4.1.15 Campaign L3k

Campaign L3k spanned 16 days. The IST observed 67,748,591 stars during this period. Campaign L3k was operated in (+X) airplane mode. The distortion map, distortion vector map, and star density map generated using the data from this campaign are provided in the figures below.

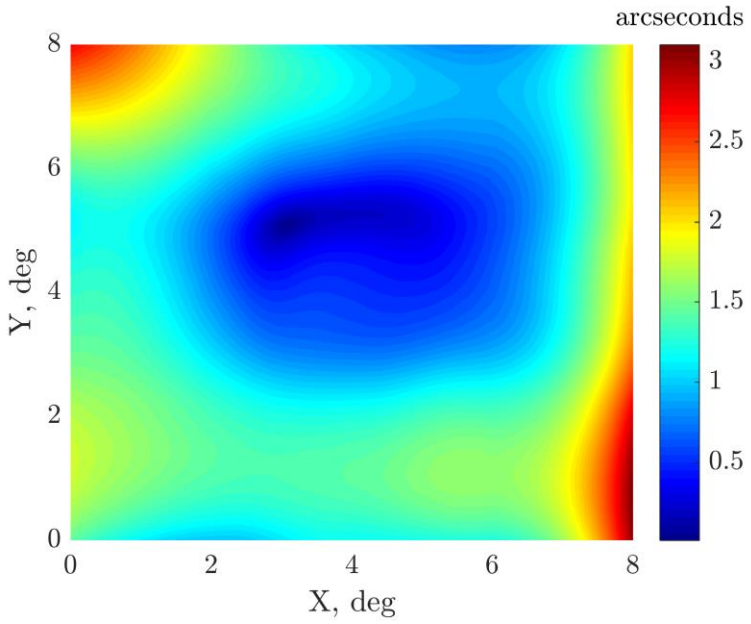

Figure 50: Distortion map for the ICESat IST, generated from observations collected during campaign L3k.

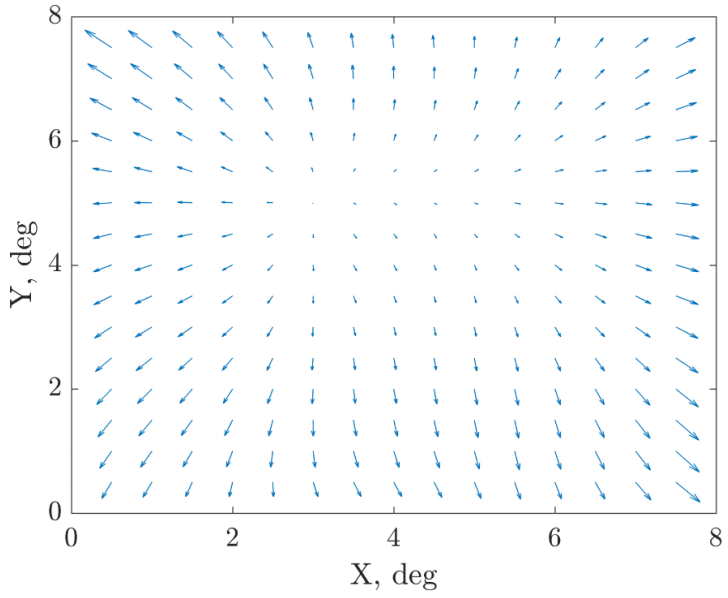

Figure 51: Distortion vector map for the ICESat IST, generated from observations collected during campaign L3k.

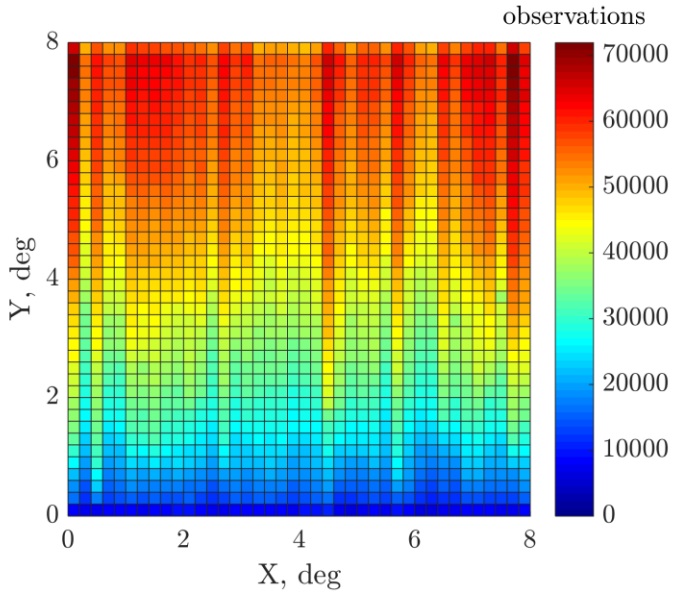

Figure 52: Star density map for the ICESat IST, generated from observations collected during campaign L3k.

4.1.16 Campaign L2d

Campaign L2d spanned 23 days. The IST observed 94,009,239 stars during this period. Campaign L2d was operated in (-Y) sailboat mode. The distortion map, distortion vector map, and star density map generated using the data from this campaign are provided in the figures below.

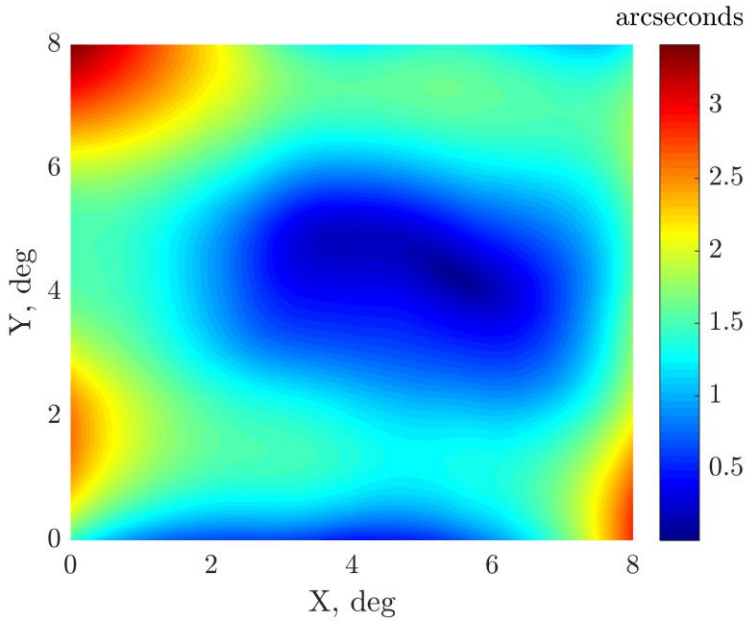

Figure 53: Distortion map for the ICESat IST, generated from observations collected during campaign L2d.

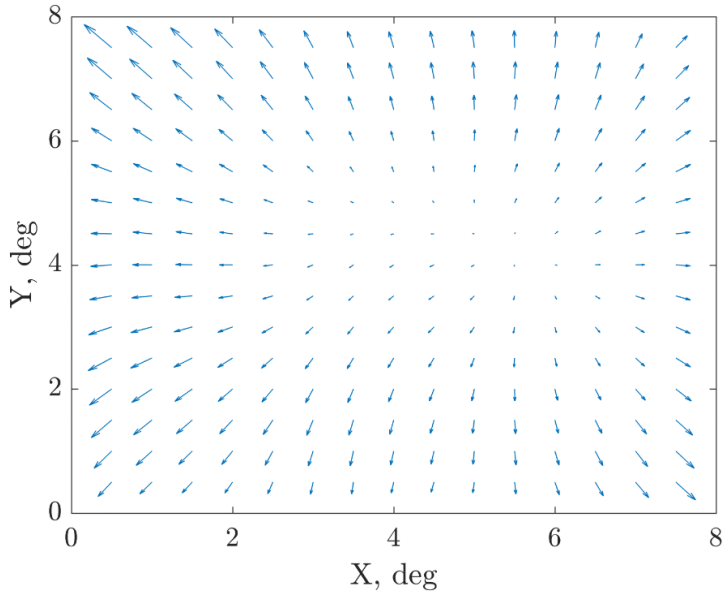

Figure 54: Distortion vector map for the ICESat IST, generated from observations collected during campaign L2d.

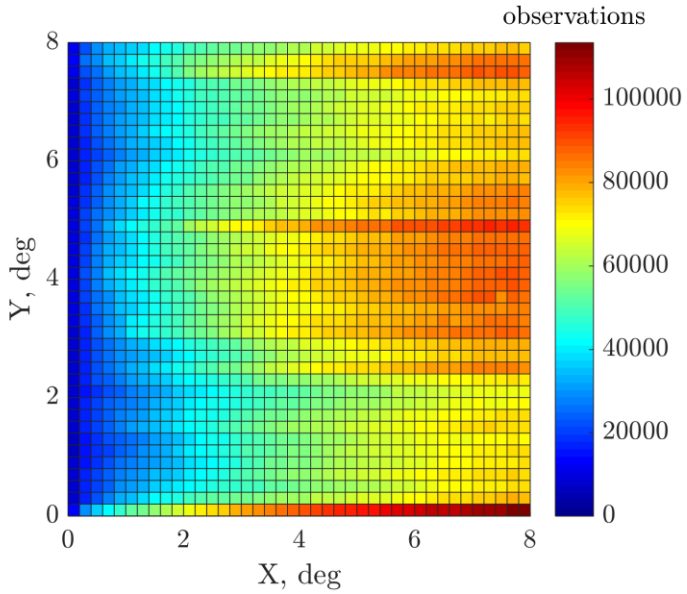

Figure 55: Star density map for the ICESat IST, generated from observations collected during campaign L2d.

4.1.17 Campaign L2e

Campaign L2e spanned 34 days. The IST observed 155,654,414 stars during this period. Campaign L2e was operated in (-Y) sailboat mode. The distortion map, distortion vector map, and star density map generated using the data from this campaign are provided in the figures below.

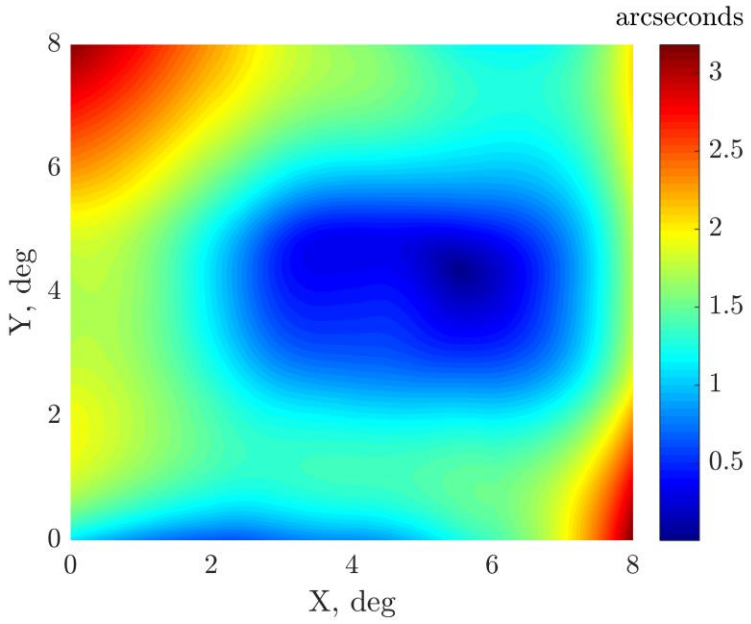

Figure 56: Distortion map for the ICESat IST, generated from observations collected during campaign L2e.

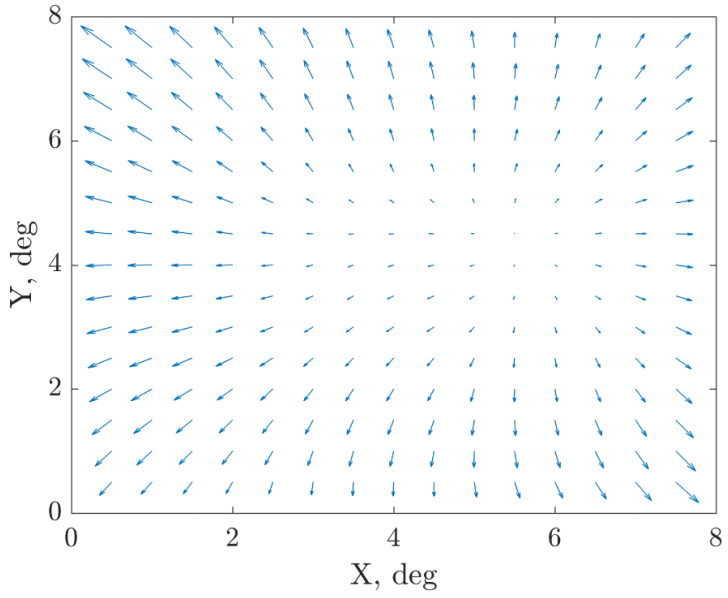

Figure 57: Distortion vector map for the ICESat IST, generated from observations collected during campaign L2e.

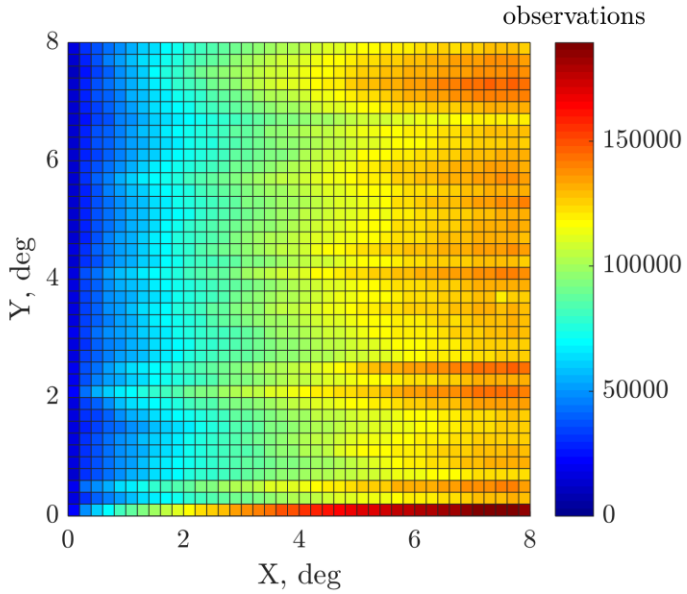

Figure 58: Star density map for the ICESat IST, generated from observations collected during campaign L2e.

4.1.18 Campaign L2f

Campaign L2f spanned 12 days. The IST observed 46,875,331 stars during this period. Campaign L2f was operated in (-X) airplane mode. The distortion map, distortion vector map, and star density map generated using the data from this campaign are provided in the figures below. The distortion map for this campaign was generated with significantly less data than was used for the other campaigns, but it still shares the general features and magnitude of the distortion found in most other campaigns. This suggests that there are enough observations present in most to campaigns to minimize the effects of noise.

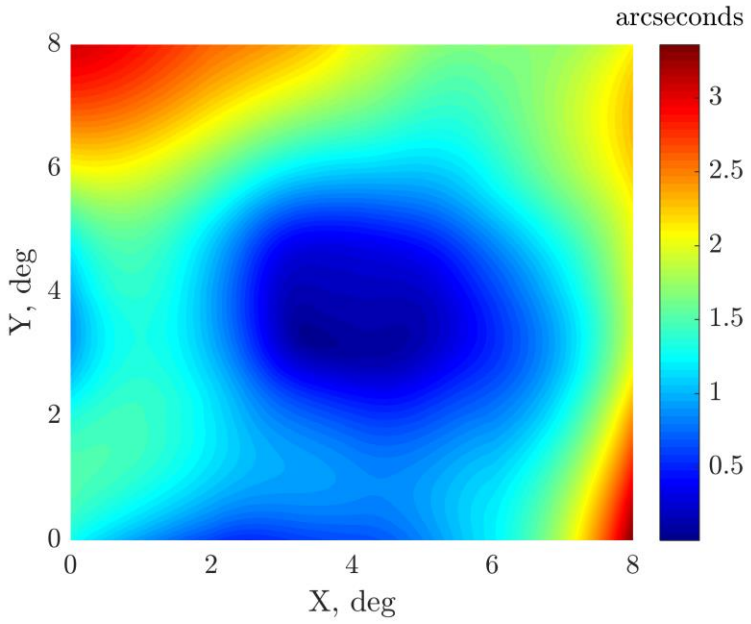

Figure 59: Distortion map for the ICESat IST, generated from observations collected during campaign L2f.

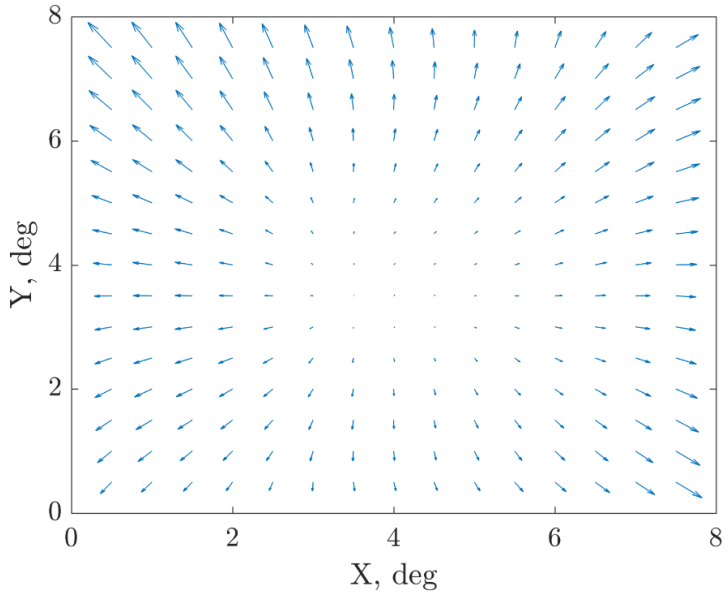

Figure 60: Distortion vector map for the ICESat IST, generated from observations collected during campaign L2f.

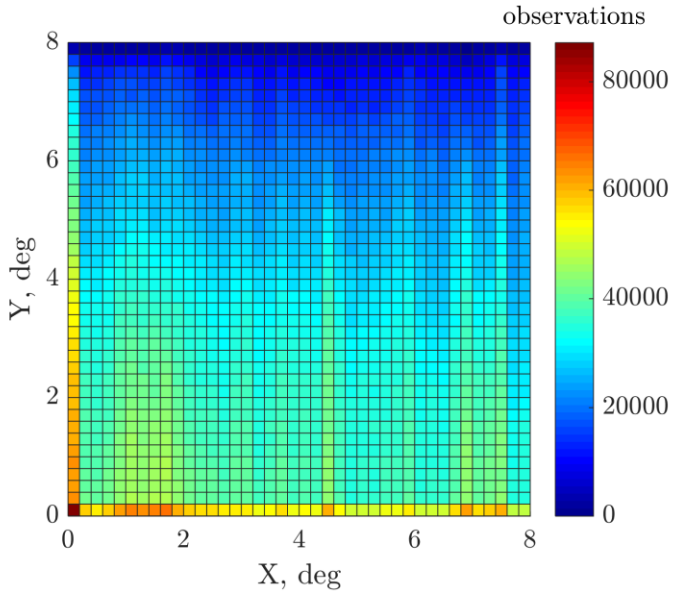

Figure 61: Star density map for the ICESat IST, generated from observations collected during campaign L2f.

4.1.19 Mission

Over the duration of the mission, the IST observed 2,536,867,725 stars. The distortion map, distortion vector map, and star density map generated using the entirety of the data collected over the mission are provided in the figures below.

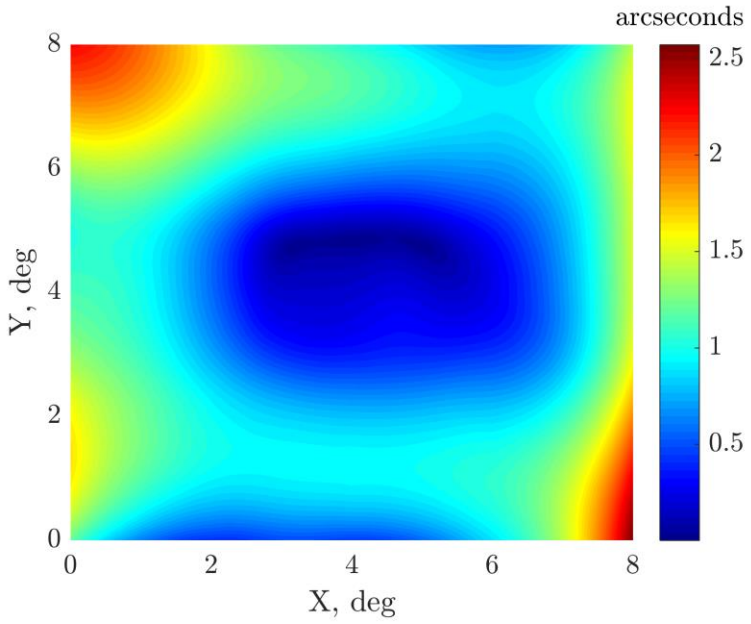

Figure 62: Distortion map for the ICESat IST, generated from observations collected over the full mission.

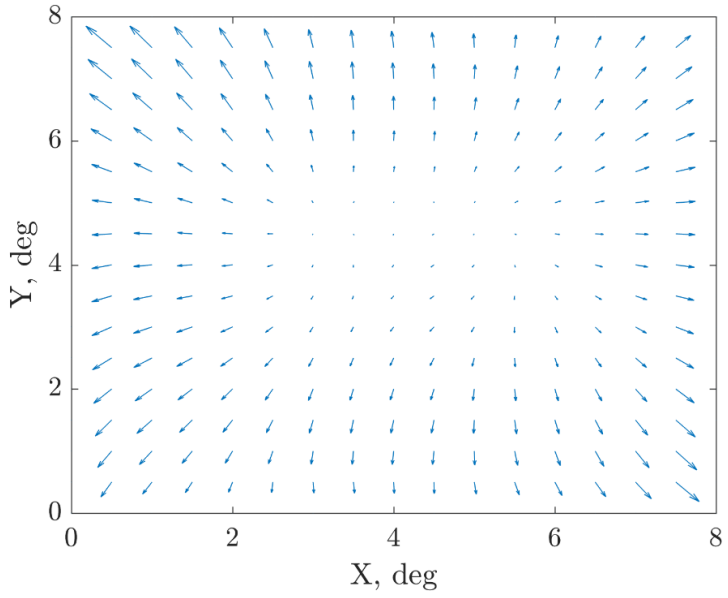

Figure 63: Distortion vector map for the ICESat IST, generated from observations collected over the full mission.

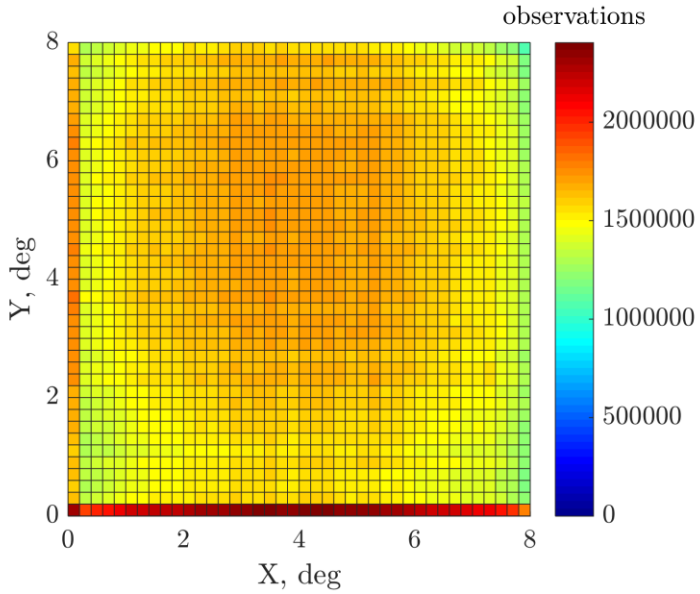

Figure 64: Star density map for the ICESat IST, generated from observations collected over the full mission.

4.7.19 Summary

Apart from campaigns L2c and L3f, the distortion maps share very similar features. The general trend of increased distortion with increased radial distance from the center is characteristic of classical radial distortion in optics which can take the form of barrel or pincushion distortion. Positive radial distortion, where the distortion vector appears to point outward from the principal point is referred to as pincushion distortion, whereas negative distortion, where the distortion vector points towards the principal point, is referred to as barrel distortion[24].

The distortion vector maps reveal primarily outward pointing distortion vectors, suggesting the dominant distortion type for most campaigns is pincushion distortion. This distortion type can be attributed primarily to the lens. Although this form of distortion appears to be dominant, it is evident that there are other

distortion modes present in the maps above. If a radial distortion model was used, the higher order localized features would not be observable in the estimation and correction process. The higher magnitude distortion regions in the top left and bottom right corners of the focal plane, also evident in the mission distortion map, may be caused by malfunctioning pixels or may even be an artifact of the CCD mounting geometry.

The star density maps reveal that the number of star observations across the FOV of a star tracker is not uniform. In general, depending on the tracking and identification algorithms used, observations may be more biased towards brighter stars or may favor tracking existing stars over new stars entering the FOV. The ICESat IST identifies the brightest stars in the FOV and then tracks them until they exit from view. This creates regions of sparse observations where stars enter the FOV. This is evident in the star density maps provided in the previous sections where there are clearly fewer stars observed along the side of the FOV where stars enter. The high densities associated with the bottom row and left column are caused by the observed star positions that are defined outside the FOV. Stars can become associated with positions outside the FOV due to residual calibration errors in the principal point and focal length. Because the observations associated with positions outside the FOV are below 0° in either the X or Y direction, the densities associated with the bottom row and left column are artificially inflated. When the observation densities adjacent to one of these regions is low, the higher relative density associated with that region is not observable. The observation density map generated using the star tracker telemetry over the full mission is more uniform due to the variation of attitude modes throughout the

mission, which causes variations in the directions that stars enter and exit the FOV. The slightly higher densities observed in the center of the FOV is expected, because although the observation densities along the edges of the FOV vary from campaign to campaign, the observation density in the center of the FOV remains relatively constant. The artifacts resulting from star positions outside the FOV can still be observed in the bottom row and left column.

4.2 Effects of Aging on Distortion

Degradation of the CCD imaging array is expected over the mission duration due to the prolonged exposure to radiation. These aging effects manifest as an increase in dark current or hot pixels and charge transfer efficiency problems[27]. Dark current is the leakage current characteristic to semiconductors where electrons possess sufficient thermal energy to break free from the silicon lattice and are accumulated as signal even in the absence of light[28]. Hot pixels are localized areas where dark current is consistently high or even saturated[29]. Pixels can also experience random spikes in signal referred to as random telegraph noise[§]; however, these transient effects would not be captured very effectively by a distortion map which is derived from observed distortion over the span of a month.

Plots describing the maximum and mean distortion estimated for each campaign are provided in Figure 65 and Figure 66 to determine the existence of any aging effects as the mission progressed. In the distortion map, an increase in

[§] Random telegraph signal (RTS) noise is characterized by transitions between discrete current levels that appear to occur randomly[27].

dark current or hot pixels should manifest as an increase in maximum distortion and mean distortion.

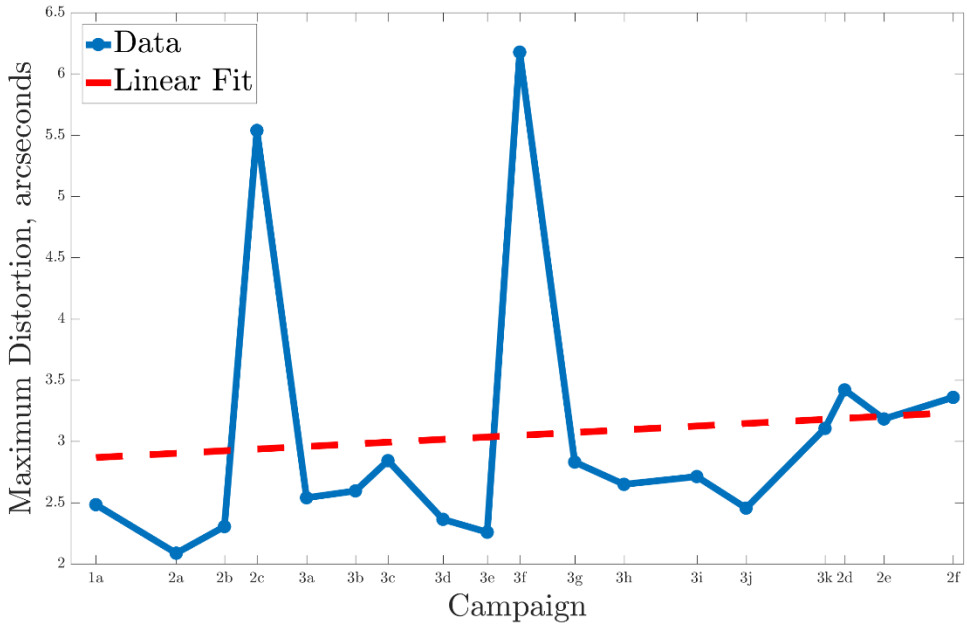

Figure 65: Maximum distortion estimated over each campaign. The horizontal distance between points is scaled to correspond to time in days. The two campaigns associated with the large spikes in maximum distortion, L2c and L3f, are the same campaigns with distortion maps that visibly differ from the other campaigns in the mission. The cause for these spikes will be discussed be discussed in the section, *Effects of Blinding on Distortion*. The maximum distortion increased from approximately 2.5 arcseconds to 3.5 arcseconds, resulting in a total increase of approximately one arcsecond.

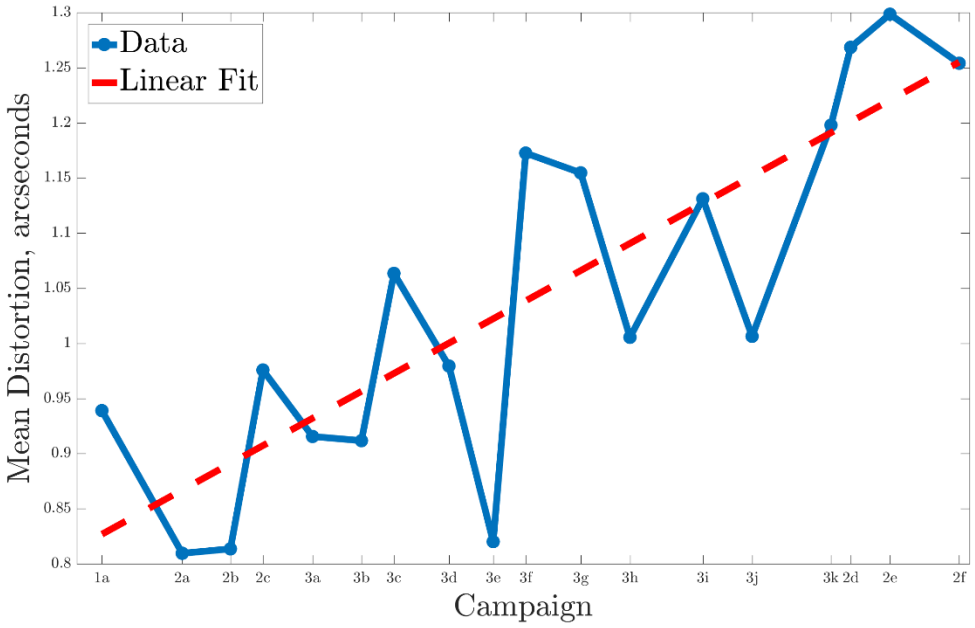

Figure 66: Mean distortion estimated over each campaign. The horizontal distance between points is scaled to correspond to time in days. The mean distortion increased from approximately 0.8 arcseconds to 1.3 arcseconds, resulting in a total increase of approximately half an arcsecond.

An increase in distortion with time is evident in Figure 65 and Figure 66. The maximum distortion for each campaign was chosen as a metric to accompany mean distortion primarily because the large regions of low distortion in the center of the distortion maps cause changes in mean distortion between campaigns to appear less pronounced. In the maximum distortion plots, the increase in distortion over the mission lifetime is approximately an arcsecond, whereas the average distortion plots show an increase of less than half an arcsecond. There are large spikes in maximum distortion for campaigns L2c and L3f. These are the same campaigns with distortion maps that visibly differ from the other campaigns in the

mission. The cause of the spikes in estimated distortion for these campaigns will be discussed in the section, *Effects of Blinding on Distortion.* Although the aging effects observed are on the order of an arcsecond or less for the ICESat IST, for high precision attitude determination applications, accounting for this temporal increase in distortion may be necessary. If the specified requirement can be met through correction of observed star positions based on a distortion map that does not account for aging effects, then temporal variations do not need to be considered. A temporal term should be incorporated if corrections of observed star positions do not appear to yield a significant reduction in attitude uncertainty for observations corresponding to certain periods of time.

4.3 Effects of Apparent Star Motion on Distortion

The direction of apparent star motion over the star tracker FOV is determined by the spacecraft attitude mode. In sailboat mode, stars travel horizontally across the FOV, whereas in airplane mode stars travel vertically across the FOV. Attitude modes can be further defined by a positive or negative axis. In (+Y) sailboat mode, stars move right to left. In (–Y) sailboat mode, stars move left to right. In (+X) airplane mode, stars move bottom to top. In (-X) airplane mode, stars move top to bottom. This apparent motion can be observed in the star density maps where columns or rows convey similar observation densities along the direction of motion. The effect of this phenomena on the distortion map is considered by comparing campaigns of the same attitude modes. Four campaigns have been chosen for direct comparison: L2a, L2b, L3a, and L3b. Campaigns L2a and L2b both correspond to a (+Y) sailboat attitude mode, whereas in campaigns

L3a and L3b ICESat was flown in a (-Y) sailboat mode. Campaigns L2a and L3a observed similar regions of the celestial sphere, as did campaigns L2b and L3b. By comparing the distortion maps for two pairs of campaigns that were derived from observations of a similar region of the celestial sphere, but were flown in different attitude modes, it is possible to decouple the effects of these parameters for an independent evaluation of their effect on distortion. The colorbars on the following distortion maps were not scaled such that they corresponded to the same maximum magnitude primarily because of the aging effects described in the previous section. The relative features, like the distribution and size of low and high distortion regions, are of greater interest in this comparison study.

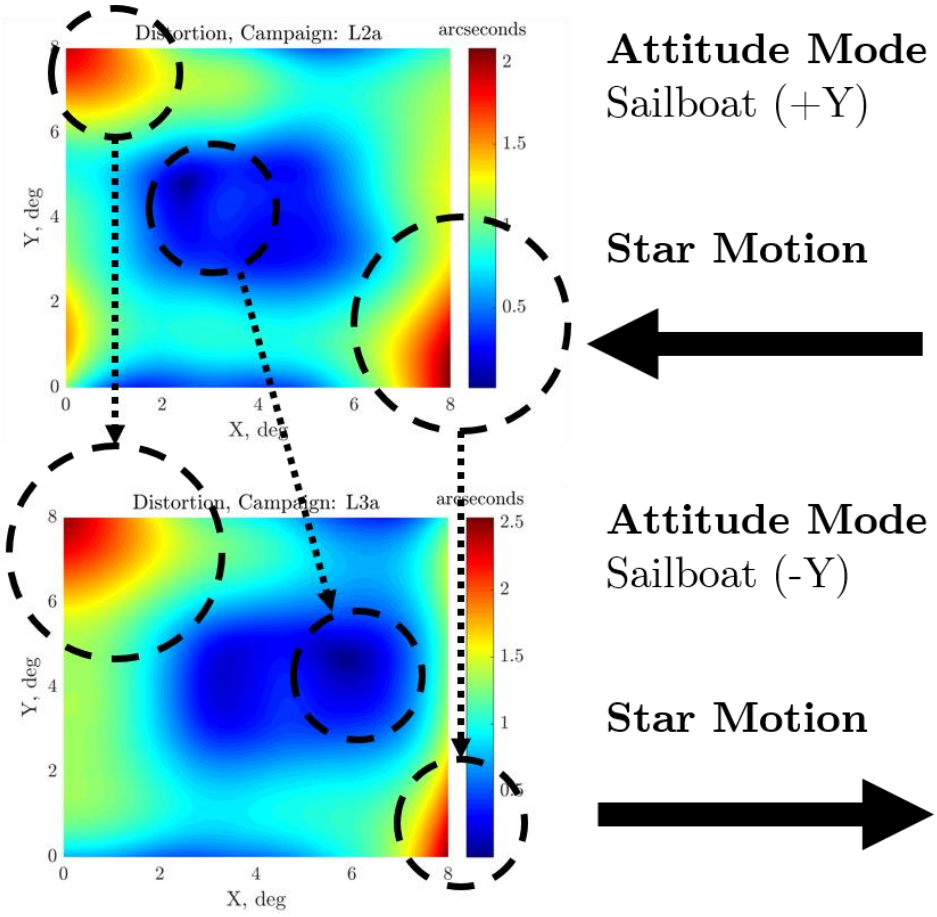

Figure 67: Comparison of distortion map features for campaigns L2a and L3a, flown in (+Y) sailboat mode and (-Y) sailboat mode respectively. L2a spanned day 268 to day 323 of 2003. L3a spanned day 277 to day 313 of 2004.

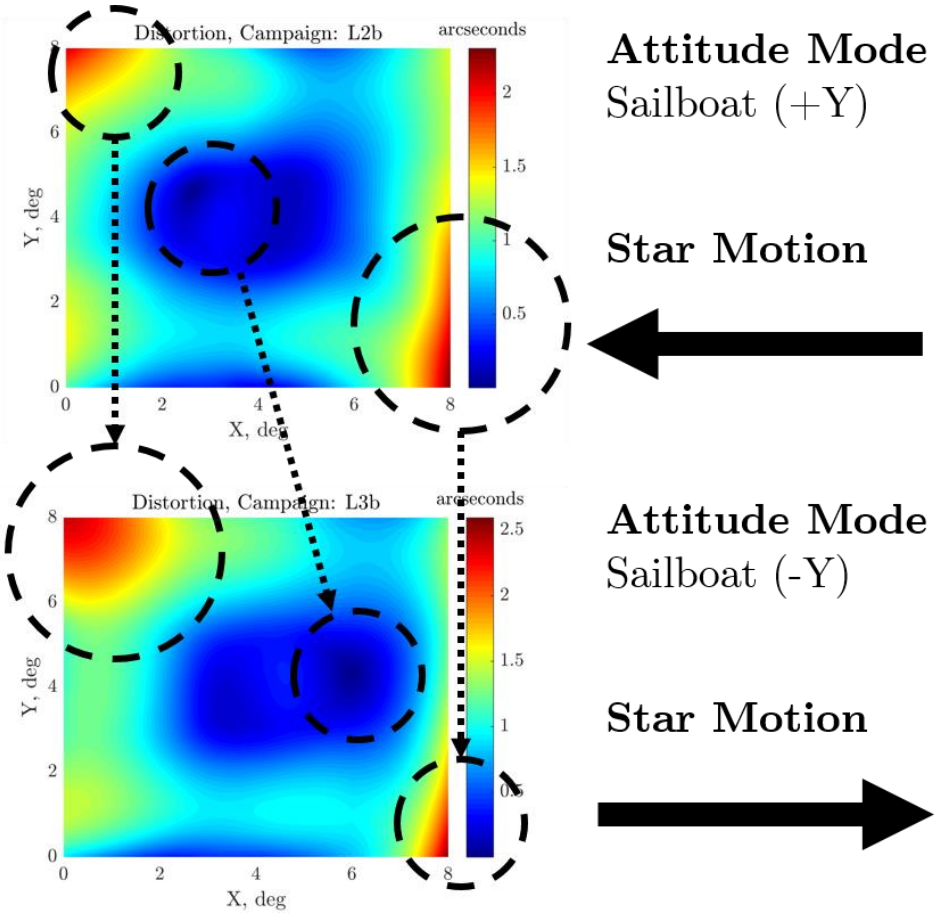

Figure 68: Comparison of distortion map features for campaigns L2b and L3b, flown in (+Y) sailboat mode and (-Y) sailboat mode respectively. L2b spanned day 48 to day 81 of 2004. L3b spanned day 48 to day 83 of 2005.

In campaigns L2a and L2b, stars move right to left across the FOV, creating a sparser observation region to the right of the FOV where they enter. Campaigns L3a and L3b experience star movement in the FOV in the opposite direction, left to right, creating more sparse regions to the left of the FOV where they enter. The effects of star entry and exit in the FOV manifests as an increase in relative distortion where stars enter and a decrease in relative distortion where stars exit.

This is illustrated in the campaign comparisons provided in the figures above, where the circled features to the left and right of the FOV are shown to increase or decrease depending on direction of apparent star motion. Furthermore, the low regions of distortion near the center of the FOV are also observed to shift in the direction of apparent star motion. Originally, the distinct appearance of the L2c and L3f distortion maps was thought to be attributed to the direction of star motion within the FOV; however, campaign L2f was also operated in a (–X) attitude mode and did not share those distinct features. Artifacts of the attitude mode are identifiable in all three (–X) attitude mode campaigns in Figure 69 showing that regions of higher distortion are concentrated to the top of these distortion maps, where stars enter the FOV.

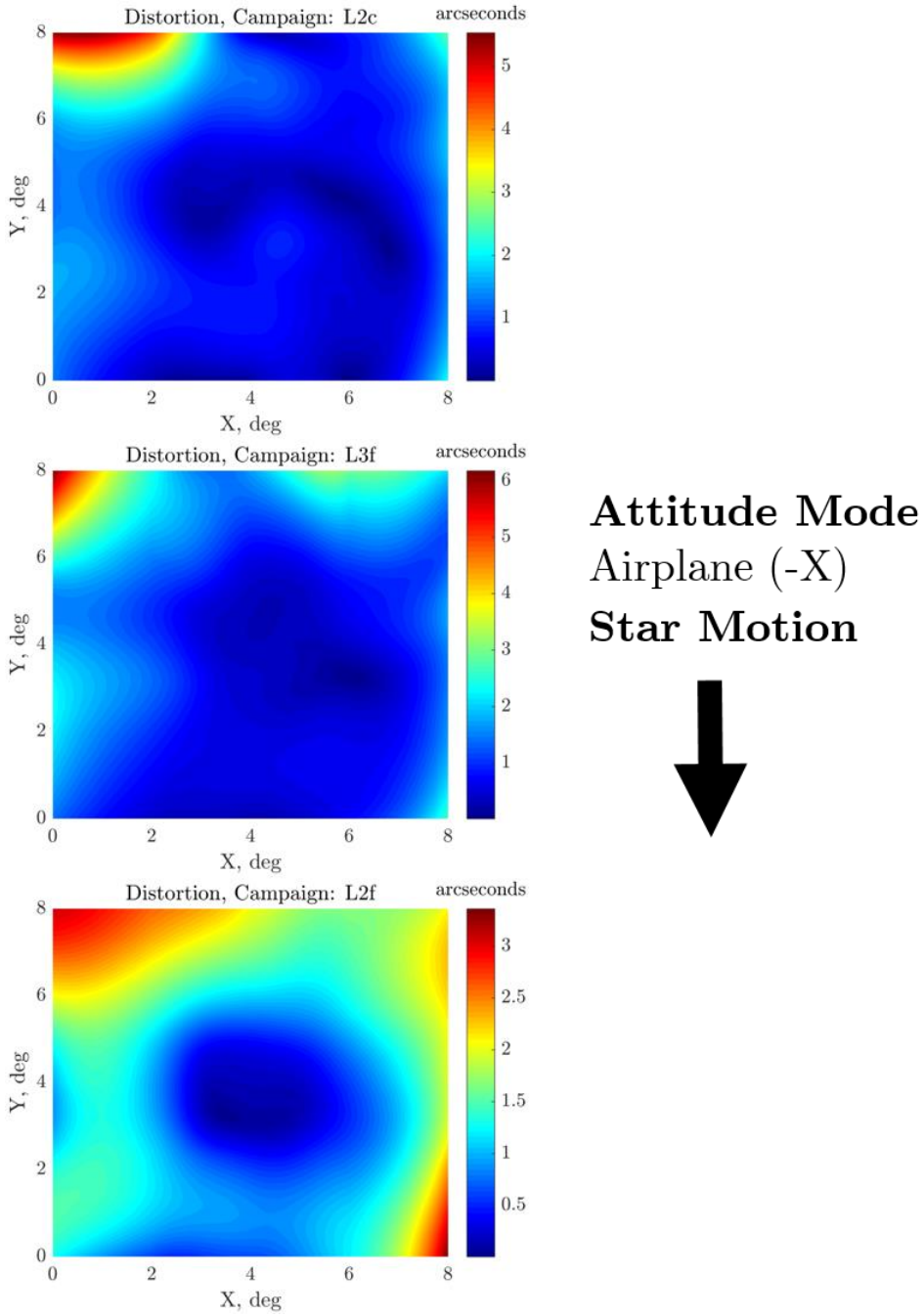

Figure 69: Distortion maps for campaigns where ICESat was operated in the (–X) attitude mode. L2c spanned day 139 to day 173 of 2004. L3f spanned day 144 to day 177 of 2006. L2f spanned day 273 to day 284 of 2009.

Finally, the low regions of distortion at the bottom of the FOV present in other campaigns show an increase in distortion for campaigns L3c and L3k where stars now enter the FOV from the bottom, as shown in Figure 70.

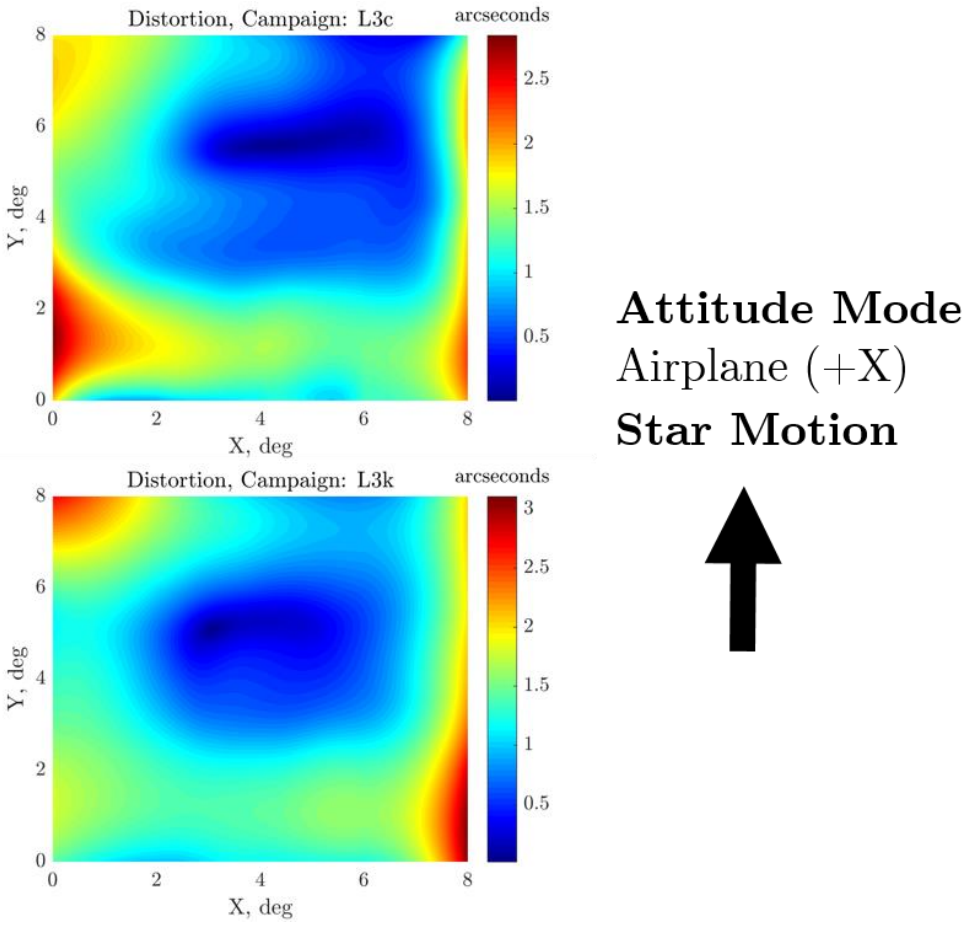

Figure 70: Distortion maps for campaigns where ICESat was operated in the (+X) attitude mode. L3c spanned day 140 to day 174 of 2005. L3k spanned day 278 to day 293 of 2008.

These observed phenomena are significant in that they demonstrate the direction stars enter the FOV does influence the distortion map.

As explained in the earlier section, *ICESat Attitude Determination Implementation*, after periods of no star observations, the attitude estimate is poor. The first stars will be observed at the edge of the FOV causing this region to be more sensitive to high distortion observations due to poor attitude estimates because of the attitude dependent nature of the distortion estimation algorithm. Furthermore, because fewer observations tend to occur in this region, there are fewer observations corresponding to distortion observations of a more typical magnitude to mitigate the effects of outliers. The sparsity of observations in this region is evident in the star density maps provided in the section, *Star Tracker Distortion Maps*.

To prevent the creation of regions of artificially high distortion, observations should be collected for varying attitude modes to ensure a more uniform coverage of the FOV. Recognizing that spacecraft maneuvers are not typically driven by calibration requirements of attitude sensors, it is recommended that this artifact be compensated for through additional post-processing techniques that identify and either exclude or reduce the weight of high distortion observations corresponding to poor attitude estimates from sources not attributable to systematic star tracker distortion. If additional star trackers are available to support attitude determination while the star tracker of interest is blinded, these artifacts will not be as significant and additional post-processing would be unnecessary. The effects of excluding high distortion observations will be explored in a later section, *Effects of Blinding on Distortion*. Capturing the systematic distortion present in the star

tracker while mitigating non-systematic artifacts is paramount to obtaining a distortion map that will yield the highest reduction in uncertainty in the resulting attitude estimates.

4.4 Effects of Region of Celestial Sphere Observed on Distortion

The region of the celestial sphere observed by the star tracker is dependent on both the Earth's position in its orbit around the Sun and the beta angle. The position of the Earth in its orbit around the Sun defines the season, or calendar date. Beta angle is the angle between the spacecraft orbital plane and the Sun vector. Beta angle is defined between +90° and -90°. If the Sun vector is parallel to the orbital plane, the beta angle is 0°. If the Sun vector is perpendicular to the orbital plane, the beta angle is 90°. The range of beta angle possible for a spacecraft is a function of the obliquity of the ecliptic and the orbital inclination. The smaller the beta angle, the less time the spacecraft experiences daylight. For a star tracker oriented towards zenith, this also corresponds to an increased number of sun blinding events. Beta angle is positive when the spacecraft appears to orbit the Earth counterclockwise relative to the Sun, and negative when the spacecraft appears to orbit clockwise about the Earth relative to the Sun.

The dependence of season and beta angle on the region of stars observed is due to the precession of the spacecraft orbital plane. For an idealized inertial orbit, where the orbital plane does not precess, a zenith-pointing star tracker will always observe the same region of stars. This is illustrated in Figure 71, where the gray regions convey the star tracker line of sight.

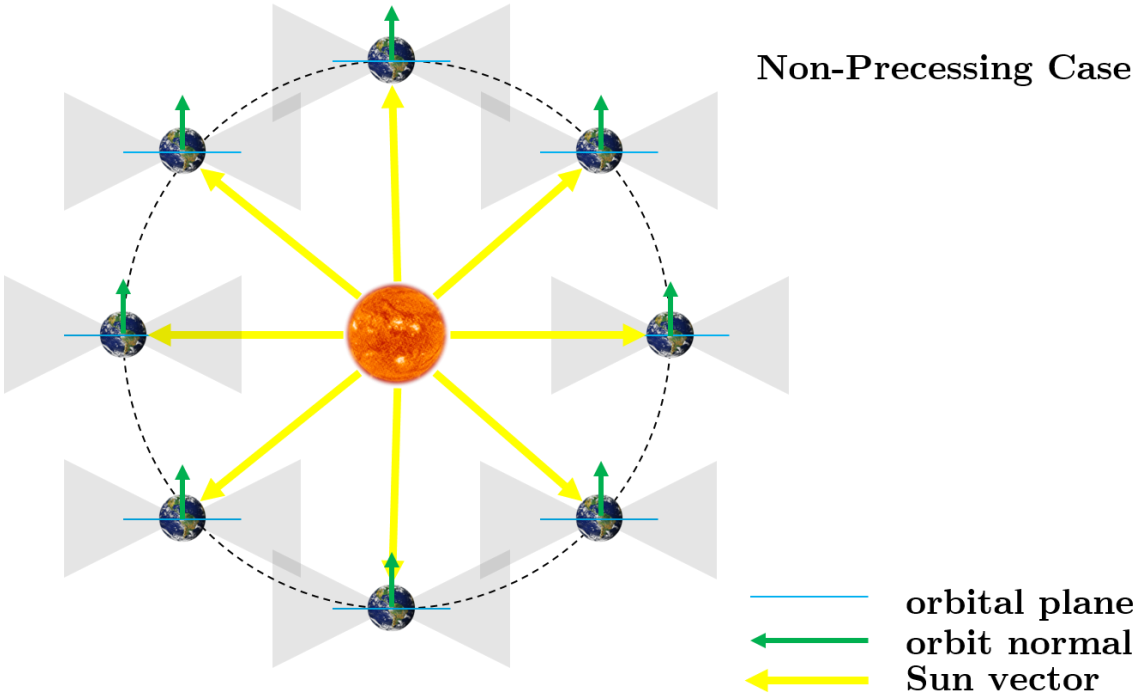

Figure 71: Star tracker observation of the celestial sphere for an inertial orbit. The gray regions convey the star tracker line of sight.

For the case of a sun-synchronous orbit, the orbital plane precesses at approximately 1° per day, resulting in a full rotation of the orbital plane once per year. The beta angle is constant for all seasons, but different regions of the celestial sphere are observed as the Earth orbits the Sun. Figure 75 illustrates a noon-midnight sun-synchronous orbit where the beta angle is constant at 0° and different regions of the celestial sphere are observed. The gray regions convey the star tracker line of sight

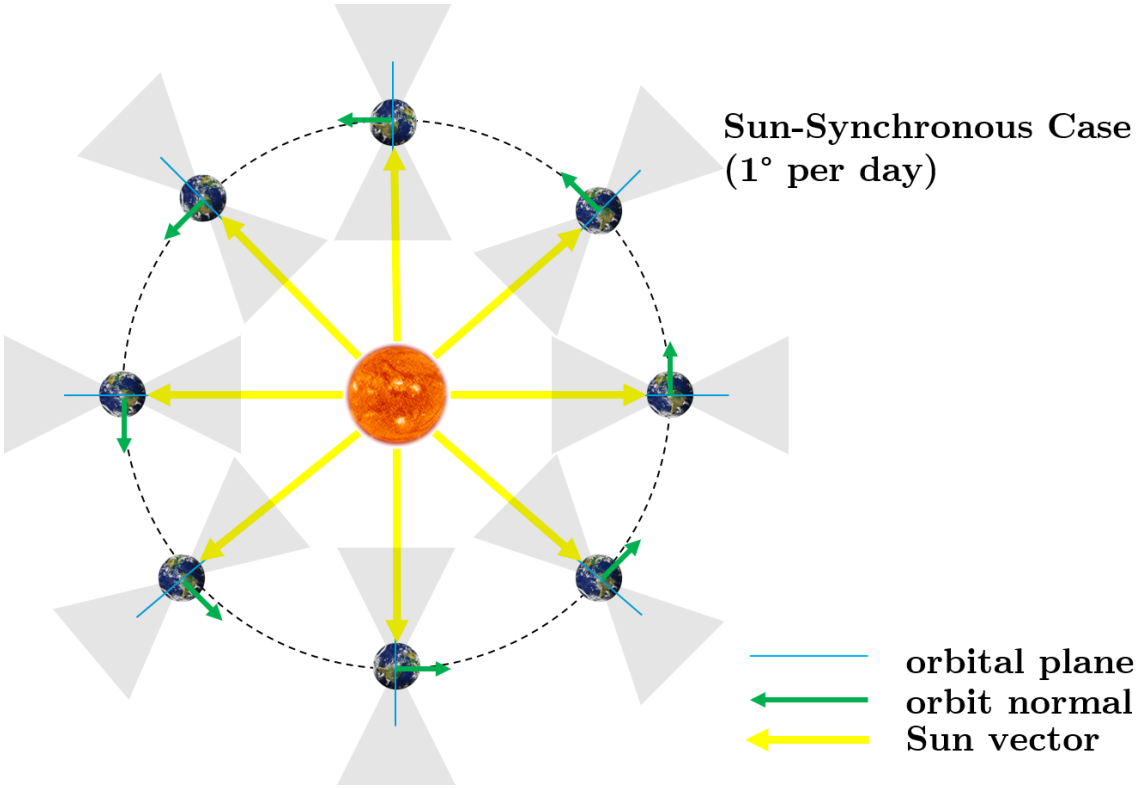

Figure 72: Star tracker observation of the celestial sphere for a noon-midnight sun-synchronous orbit. The gray regions convey the star tracker line of sight.

For ICESat, whose orbit precesses at 0.5° per day, a given region of the celestial sphere is observed once per year, for the same season and the same beta angle. This is illustrated in Figure 72, where changes in beta angle are shown over the period of one year and the gray regions convey the star tracker line of sight. The figure also models the changes in beta angle for the subsequent year, where the orbit normal is 180° out of phase from the depicted direction.

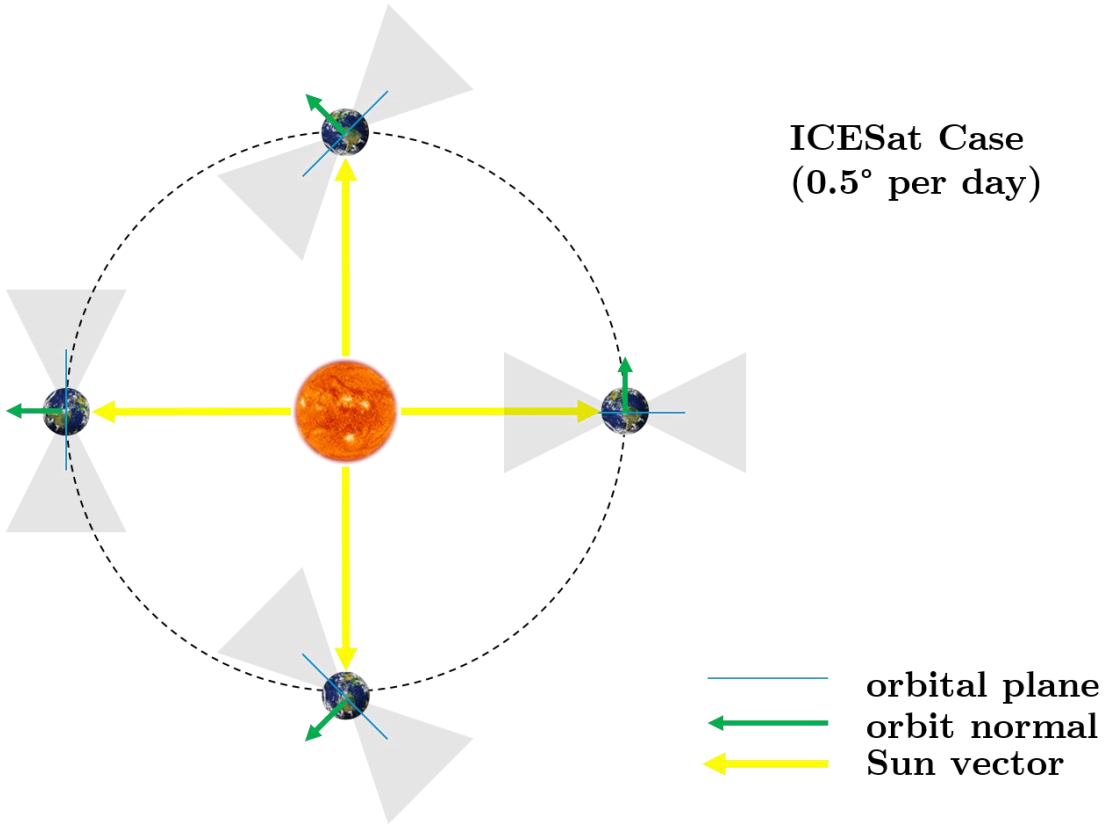

Figure 73: Star tracker observation of the celestial sphere for an ICESat-like orbit. The gray regions convey the star tracker line of sight.

Recognizing the dependence of the region of the celestial sphere on these parameters, distortion maps were compared for campaigns that coincided with similar seasons and beta angles to determine if there were any similarities observed in the distortion maps derived from stars observed over similar regions of the celestial sphere. To verify that similar regions of the celestial sphere were being observed for the campaigns of interest, a correlation study was performed. Using the stars defined in the GLAS catalog as the categories, histograms of star observations for each campaign were generated. Next, correlation coefficients were calculated between each vector of observation counts associated with each catalog

entry. The relevant properties for the most correlated campaigns are shown in Table 2. The full correlation matrix can be found in Appendix 2.

Table 2: Relevant properties for the campaigns with the most correlated star observations.

Campaign	Year	Calendar Day	S/C Attitude Mode (GLAS Frame)	Initial Beta Angle, deg	Final Beta Angle, deg	Correlation Coefficient
L3d	2005	21 Oct – 24 Nov	Sailboat (+Y)	51	63	0.97
L3i	2007	02 Oct – 05 Nov	Sailboat (+Y)	32	46	
L3g	2006	25 Oct – 27 Nov	Sailboat (-Y)	-44	-54	0.83
L3k	2008	04 Oct – 19 Oct	Airplane (+X)	-28	-32	
L3e	2006	22 Feb – 28 Mar	Sailboat (+Y)	62	48	0.75
L3j	2008	17 Feb – 21 Mar	Sailboat (+Y)	74	62	
L1a	2003	20 Feb – 29 Mar	Sailboat/Airplane (-Y/+X)	-45	-32	0.73
L3b	2005	17 Feb – 24 Mar	Sailboat (-Y)	-56	-45	

Campaigns were chosen for comparison in accordance with Table 2. L2f and L3d were also highly correlated, but because the duration of campaign L2f was much less than the duration of other campaigns, it was excluded from this analysis. For consistency in comparison, the maximum value of the distortion colorbar remains unscaled.

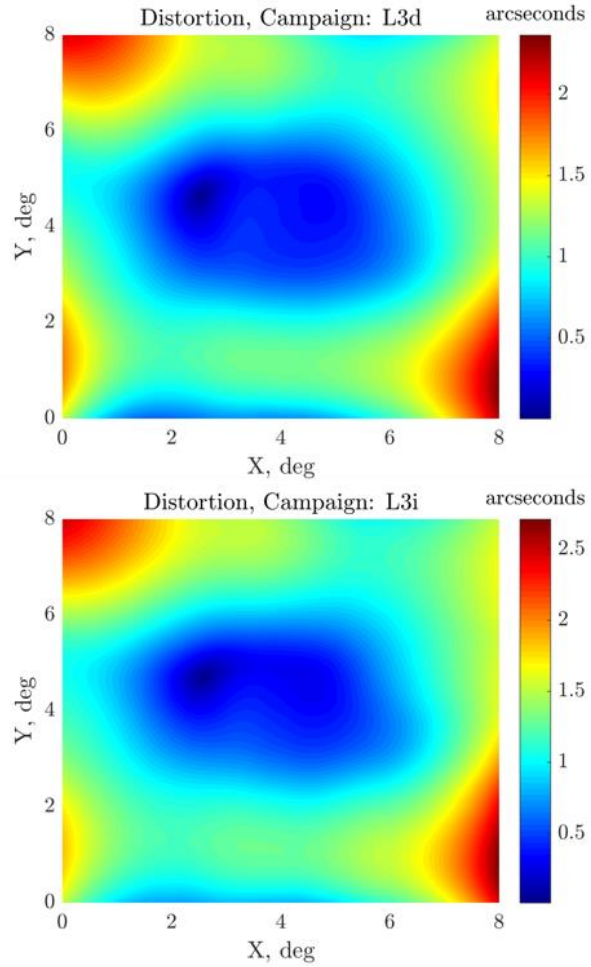

Figure 74: Distortion maps for campaigns L3d and L3i. Properties of these campaigns can be found in Table 2.

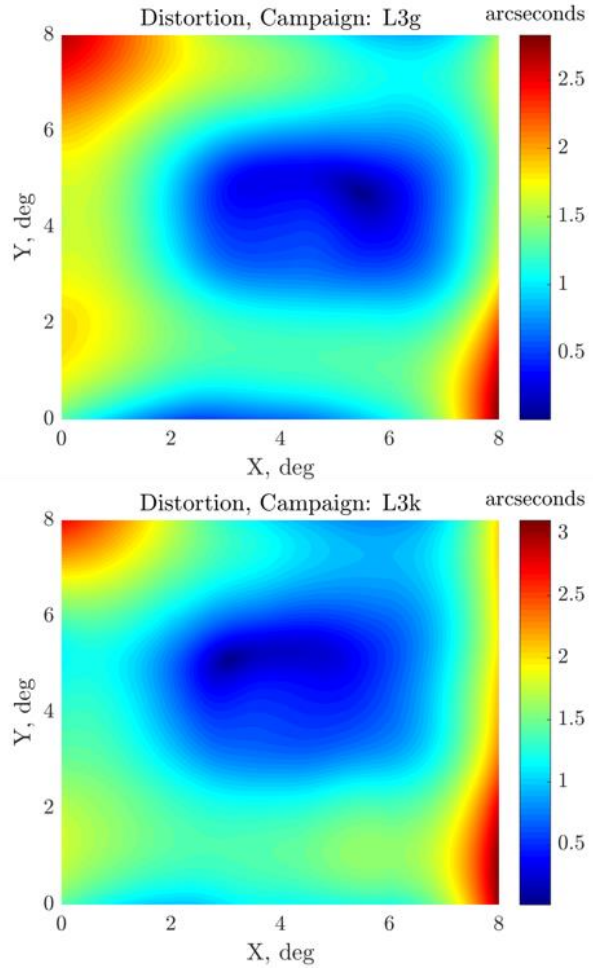

Figure 75: Distortion maps for campaigns L3g and L3k. Properties of these campaigns can be found in Table 2.

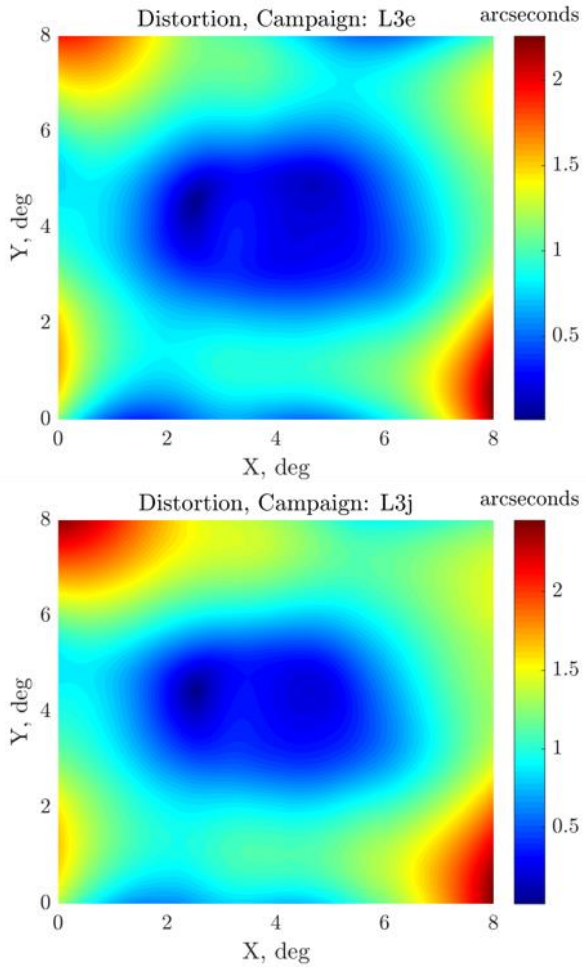

Figure 76: Distortion maps for campaigns L3e and L3j. Properties of these campaigns can be found in Table 2.

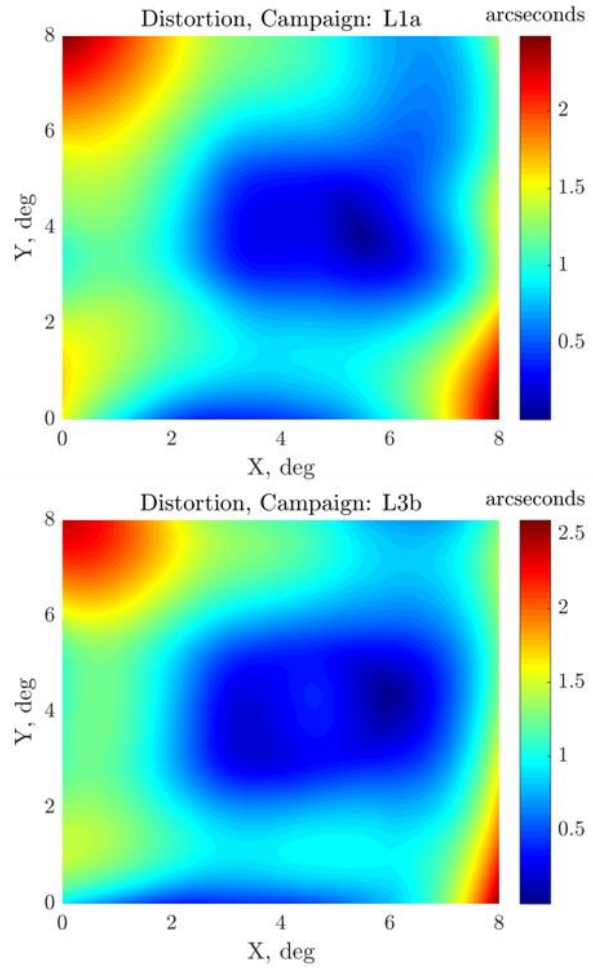

Figure 77: Distortion maps for campaigns L1a and L3b. Properties of these campaigns can be found in Table 2.

Through simple visual inspection of the distortion maps presented above, there are some obvious similarities in their features. Unfortunately, because the attitude mode is dependent on beta angle, it is not possible to decouple the problem of distortion dependence on attitude mode and region of the celestial sphere observed. Almost all comparisons above share the same attitude mode, so it is difficult to determine definitively if their similarity is due to the region of stars the

IST is observing, or an artifact of the attitude mode. The comparison between campaigns L3g and L3k is the most reflective of the effects of observing similar regions of the celestial sphere because of the difference in attitude mode. Furthermore, the correlation coefficient defining the degree of similarity between their observations is the second highest at a value of 0.83. Examining the features of the distortion maps for L3g and L3k, the similarities between them appear less pronounced than the other distortion map comparisons suggesting the effects of attitude mode are more dominant than the region of the celestial sphere observed.

This result is not unexpected, since the positions of the stars are well-defined in the star catalog. If the positions of stars in a certain region of the celestial sphere were more poorly defined, we would expect this to yield a consistently higher magnitude distortion map estimated using observations from that region of stars. This effect did not appear dominant in the distortion features and magnitudes observed. From the results of this analysis, it is possible to conclude that the region of the celestial sphere observed does not appear to affect the resulting distortion map more significantly than the parameters already considered. Furthermore, the precession of the orbital plane ensures that a variety of stars with different characteristics are used in estimating the distortion for any given region within the FOV. This should limit the contribution of any star property dependent distortion in estimating a more systematic star tracker distortion, yielding a greater reduction in uncertainty in the attitude estimates generated from applying distortion corrections to observed star positions as defined by the distortion maps.

4.5 Effects of Blinding on Distortion

Star trackers experience blinding when the FOV becomes saturated and no stars can be observed. This can happen if the Sun or Moon enters the FOV. Here, blinding is defined as any period where the star tracker observes no stars for at least two consecutive time tags. Campaigns that coincide with smaller beta angles will experience more frequent and longer periods of blinding due to the Sun. As discussed in the earlier section, *ICESat Attitude Determination Implementation*, attitude estimates during and immediately following periods of blinding are less accurate due to the attitude estimation algorithm not incorporating new observations until the EKF initialization criteria are satisfied.

The distortion observations associated with stars that coincide with poor attitude estimates are artificially inflated by an inaccurate rotation matrix. Because observed distortion is defined as the difference between the measured star position and the catalog star position rotated from the CRF to the SCF, the rotation can shift the catalog position far from the measured value. The observed distortion associated with this phenomenon can exceed arcminutes. For the purposes of this work, a high distortion observation is defined as greater than one arcminute. Figure 78 provides an example of high distortion observations occurring after blinding. The red circles define periods of blinding and the blue marks correspond to the distortion magnitude associated with each star observation. The sudden drop in observed distortion coincides with a time tag where four stars were observed and identified within the star tracker FOV. The attitude estimate associated with this time tag was obtained using QUEST, whereas the estimates preceding this were obtained through quaternion propagation using the gyroscope.

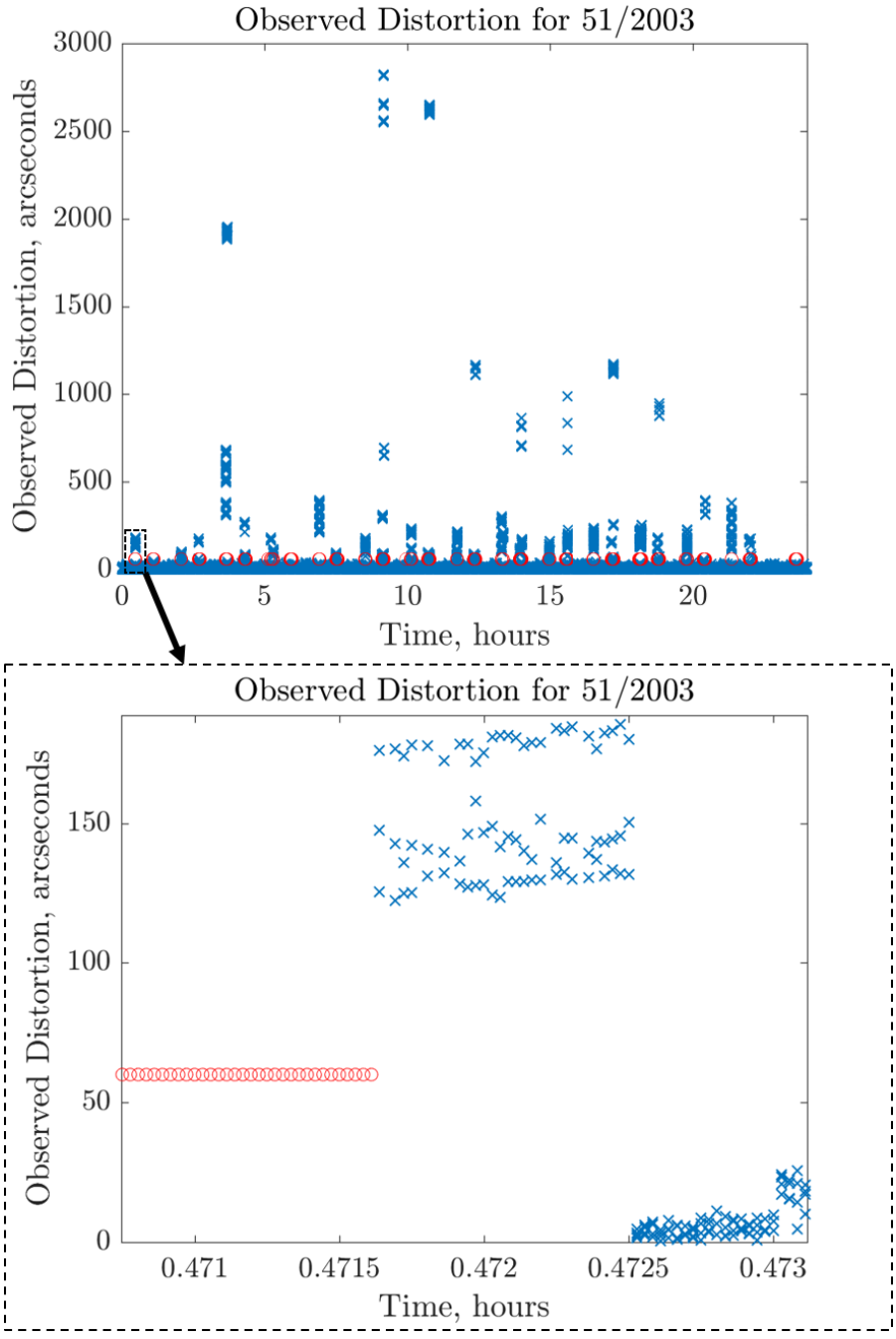

Figure 78: Example of high distortion observations occurring after periods of blinding during campain L1a on day 51 of the year 2003.

Blinding statistics were analyzed for each campaign. The results of this analysis are presented in Table 3.

Table 3: Campaign blinding observation statistics.

Campaign	Percentage of Time Blinded	Number of Blinding Periods	Number of Stars	Mean Distortion Observation (arcseconds)
L1a	5.03%	2741	145352376	4.40
L2a	0.32%	1413	254282205	4.06
L2b	4.70%	2152	137380590	4.42
L2c	13.55%	**5678**	135654382	5.77
L3a	0.94%	2400	161387262	4.21
L3b	1.25%	2635	151888368	4.32
L3c	11.96%	**7611**	137303074	5.37
L3d	0.52%	1214	159025723	4.34
L3e	0.35%	1078	156443642	4.26
L3f	11.58%	**4841**	133451338	5.45
L3g	1.03%	**4329**	145423157	4.43
L3h	0.69%	**5634**	150349948	4.35
L3i	4.34%	3693	144878058	4.71
L3j	0.20%	716	159760021	4.42
L3k	0.52%	833	67748591	4.42
L2d	1.88%	2983	94009239	4.93
L2e	0.30%	1333	155654414	4.52
L2f	4.79%	1846	46875331	4.81

The blinding statistics indicate that the campaigns that experienced the highest number of blinding periods were campaigns L2c, L3c, L3f, L3g, and L3h. Campaigns L2c, L3c, and L3f experienced both the longest periods of blinding and the highest mean observed distortion. Campaigns L3g and L3f, although they also experienced a high number of blinding periods, did not yield a high mean observed distortion. Further examination of the distribution of the high distortion observations indicated that for campaigns L2c, L3c, and L3f, there was a high number of observations corresponding to 1000 arcseconds or greater relative to the other campaigns. The distributions of the high distortion observations for these campaigns are shown in the figures below.

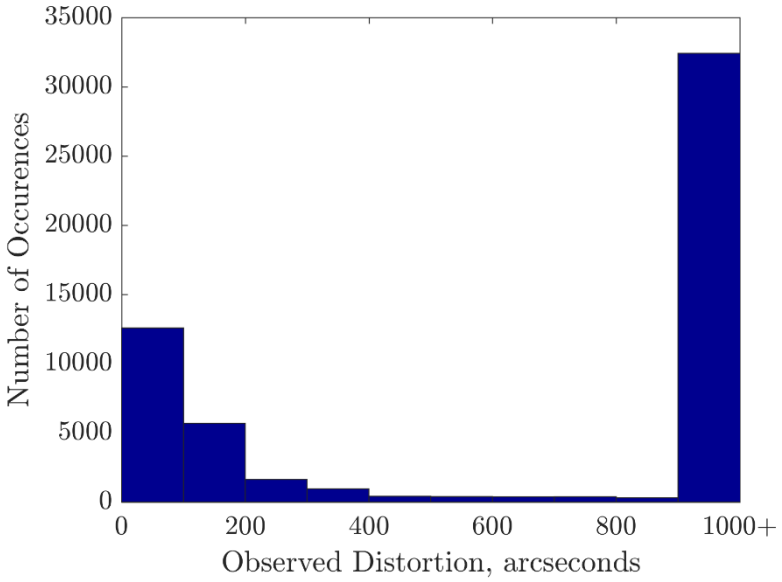

Figure 79: Distribution of high distortion observations for campaign L2c.

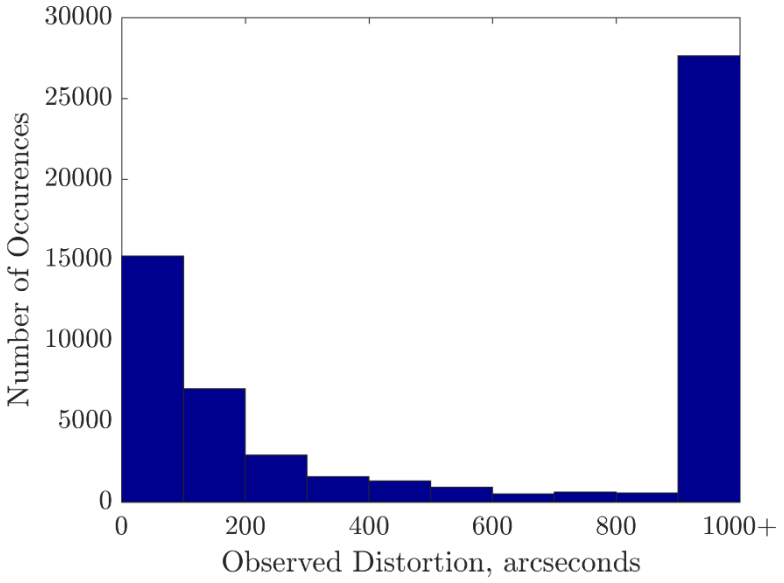

Figure 80: Distribution of high distortion observations for campaign L3c.

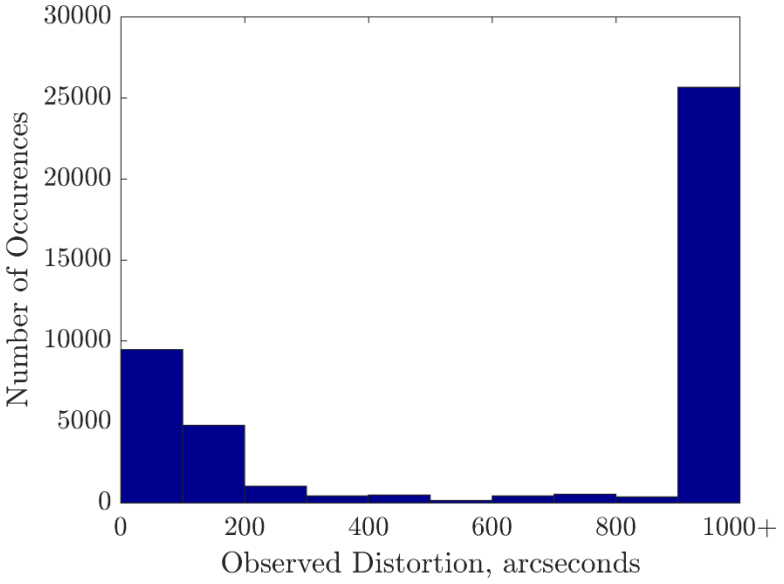

Figure 81: Distribution of high distortion observations for campaign L3f.

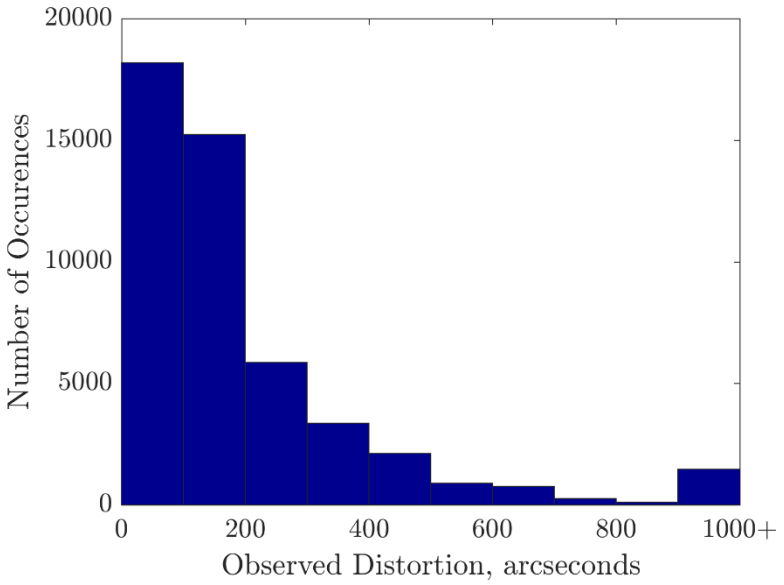

Figure 82: Distribution of high distortion observations for campaign L3g.

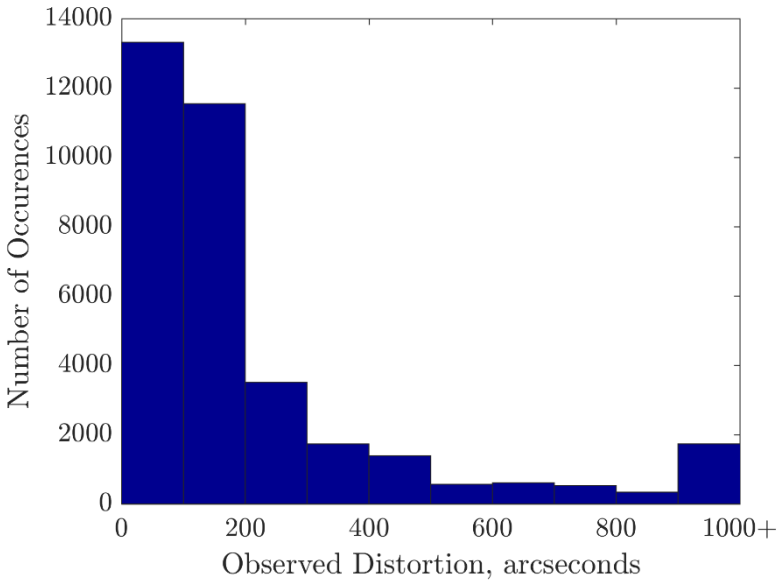

Figure 83: Distribution of high distortion observations for campaign L3h.

Most campaigns reflect distributions like those in L3g and L3f where the observations occur mostly below 100 arcseconds and gradually diminish as the distortion magnitude increases. Note that because a high distortion observation is defined at one arcminute, the histogram bin corresponding to 0 to 100 arcseconds is a measure of distortion observations between 60 and 100 arcseconds. The outliers prevalent in campaigns L2c, L3c, and L3f are reflected in the distortion maps generated from these data. The distortion maps for these campaigns are provided in Figure 84.

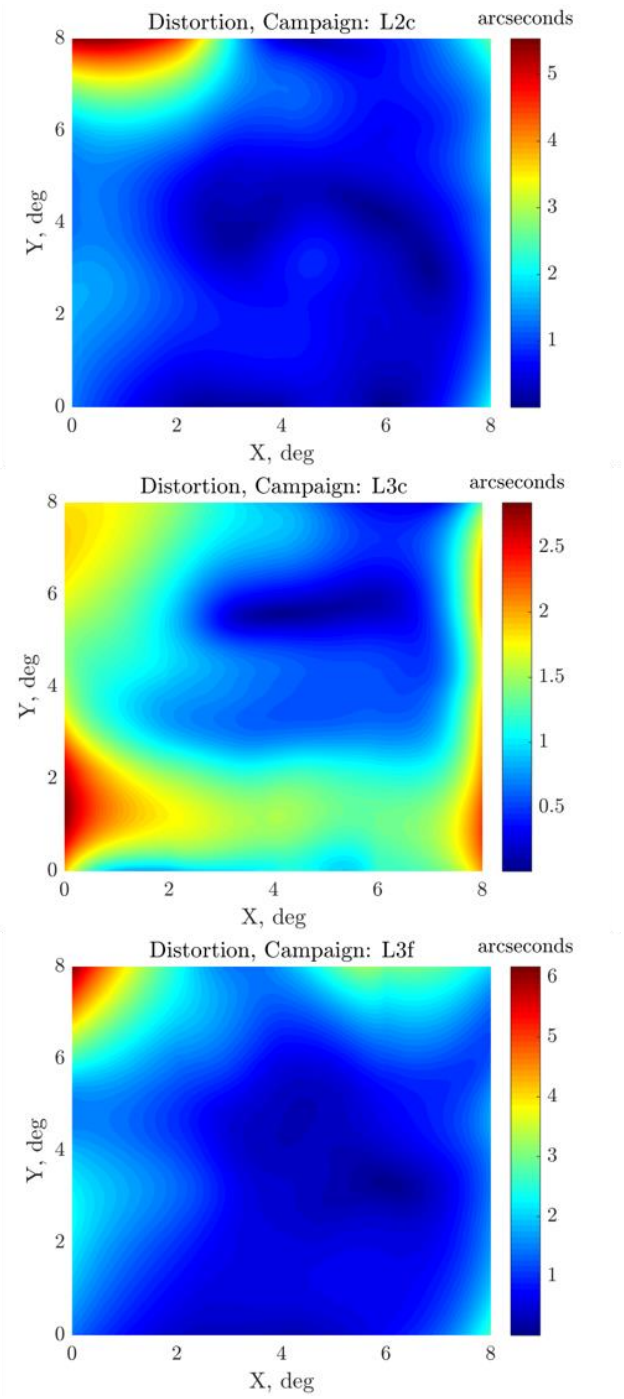

Figure 84: Distortion maps for campaigns L2c, L3c, and L3f illustrating the effects of high distortion observations following blinding periods.

The estimated distortion for all three campaigns, L2c, L3c, and L3f, deviates significantly from the distortion maps generated for other campaigns as well as the mission distortion map. This deviation is due to the high distortion observations that occur after periods of blinding yield poor attitude estimates. The high distortion regions at the top of the FOV for campaigns L2c and L3f are caused in part by the (-X) airplane attitude mode which coincides with apparent star motion from top to bottom of the FOV. After blinding periods, stars will first be observed by the star tracker at the top of the FOV, where they enter. At the same time, these star observations will be associated with poor attitude estimates, inflating the distortion observation. Furthermore, as the star tracker transitions from a blinding period to one of nominal operations, a relative sparsity of observations will be maintained at the top of the FOV, due to the nature of the IST's search and track algorithm described in the earlier section, *ICESat Mission Overview*. A similar explanation can be applied to campaign L3c, where it appears there was a high enough concentration of distortion observations between 60 and 100 arcseconds to help average out the effect of the higher distortion observations. Additionally, the (+X) airplane attitude mode resulted in stars entering the FOV from the bottom, where distortion estimates were consistently lower for that region across all campaigns. The ultimate effect of these conditions is a distortion map the reflects an inflated distortion where stars enter the FOV. If these distortion maps were used to calibrate the star tracker, corrections applied to observations in the region where stars enter the FOV would be too large and ultimately decrease the precision of the attitude estimate.

To confirm that these outliers were the source of the high distortion estimated for these campaigns, distortion maps were generated where high distortion observations, greater than one arcminute, were excluded. The distortion maps presented below demonstrate the effects of excluding these observations on the campaigns containing the highest number of these outliers, L2c, L3c, and L3f. These were the same campaigns presented in Figure 84.

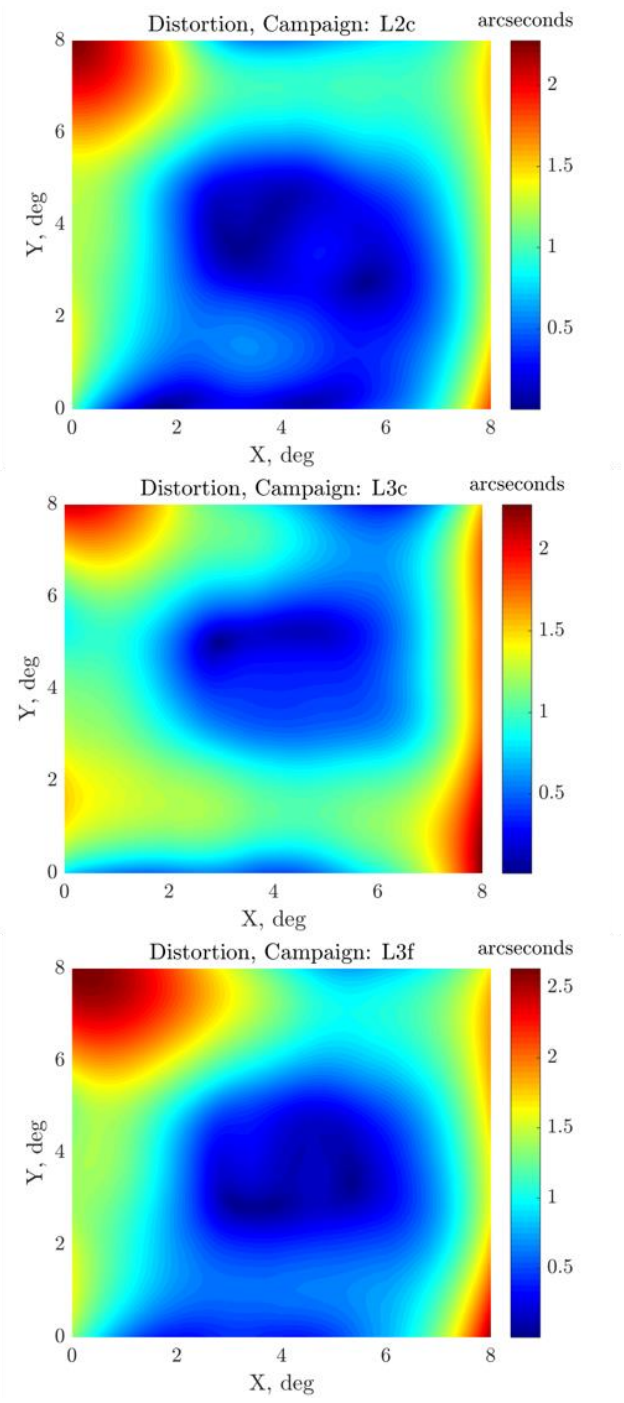

Figure 85: Distortion maps excluding high distortion observations for campaigns L2c, L3c, and L3f.

The distortion maps for these campaigns now better reflect the ICESat mission average in both magnitude and general shape. Some unique features remain in campaigns L2c and L3f, mainly the large region of low distortion at the bottom of the FOV, but this is an artifact of the attitude mode as explained in the section, *Effects of Apparent Star Motion*. Distortion maps excluding high distortion observations were generated for all ICESat campaigns. For most campaigns, apart from those shown in Figure 85, the difference between the original and modified distortion maps was negligible. It is worth noting that for the distortion map generated using all observations over the mission, excluding high distortion observations similarly had a negligible effect. This is due to the larger number of distortion observations that correspond to a more typical distortion magnitude effectively averaging out the outlier values occurring in certain campaigns. Through proper consideration of these artificially high distortion observations, the resulting distortion map will be more reflective of the systematic distortion present in the star tracker, and yield correction vectors that more effectively reduce the uncertainty in the attitude estimates.

4.6 Effects of Temperature on Distortion

Temperature data for the beginning and end of each campaign were obtained from NASA. Temperatures for campaign L2f were not available. The temperatures were recorded from thermocouples mounted to the optical bench where the IST was also mounted. The temperature data does not have high temporal resolution and is more representative of an average campaign temperature. Even with higher frequency temperature data available, it would not

be possible to use those data to determine the relationship between temperature and distortion over the entire FOV using this method primarily because the data collected over small time intervals would also correspond to small spatial regions of the FOV. By considering the effects of temperature at the beginning and end of the campaign, it is still possible to obtain a general understanding of how the long-term temperature gradient and average temperature experienced by the star tracker during each campaign affects the distortion map. The incident solar flux experienced by a spacecraft depends primarily on the beta angle. Without the presence of thermal control, an increase in Sun exposure coinciding with a larger beta angle should result in a temperature increase. Although a lower beta angle does coincide with less Sun exposure, it also coincides with greater thermal cycling as the spacecraft transitions between daylight and eclipse as it orbits the Earth. Orbital variations in temperature are not captured with these data. The temperature data are presented in Table 4.

Table 4: Temperature data from the optical bench thermocouples for each campaign, excluding campaign L2f.

Campaign	Initial Temperature, °C	Final Temperature, °C	Initial Beta Angle, deg	Final Beta Angle, deg
L1a	**17.8**	**18.5**	**-45**	**-32**
L2a	14.2	17.6	51	69
L2b	**18**	**18.8**	**54**	**40**
L2c	**15.2**	**14.8**	**13**	**-4**
L3a	16.6	16.3	-48	-58
L3b	16.3	16.8	-56	-45
L3c	**14.4**	**14.5**	**-20**	**-4**
L3d	16	15.5	51	63
L3e	16.5	17	62	48
L3f	**15.8**	**15.8**	**20**	**4**
L3g	16.3	16	-44	-54
L3h	16	16.5	-60	-47
L3i	17.5	17	32	46
L3j	16	16.5	74	62
L3k	16.5	16.8	-28	-32
L2d	17	22	-45	-53
L2e	**21.9**	**24**	**-71**	**-59**

Campaign L2e experienced higher temperatures and higher beta angles relative to most of the other campaigns; however, campaign L3j experienced even higher beta angles but maintained a much lower temperature. The presence of thermal control systems is the reason temperature effects were considered

separately from beta angle. The plot in Figure 86 demonstrates the growth in mean distortion with time, but also identifies the campaigns with the highest average temperature and the lowest average temperatures.

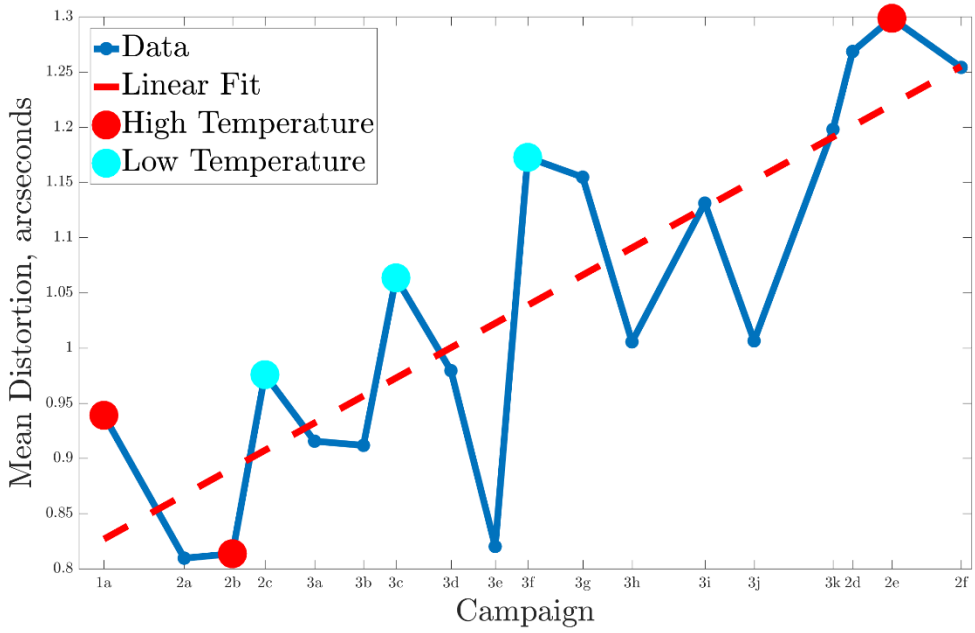

Figure 86: Mean distortion estimated over each campaign. The horizontal distance between points is scaled to correspond to time in days. High and low temperature campaigns correspond to red and blue points respectively.

Increases in temperature for a CCD imaging array cause higher occurrences of hot pixels and a general increase in dark current. Typically, dark current corresponds to approximately 1 $nAcm^{-2}$ at 20 °C and decreases by a factor of two for every 7 °C to 8 °C reduction in temperature[27]. This would suggest higher distortion for campaigns operating at higher temperatures and lower distortion for

those at lower temperatures. The above plot does not support those predicted trends. L2c and L3c, with the lowest average operating temperatures should yield the lowest distortion; however, L2c experienced some of the highest distortion. L1a, which operated around 18 °C, and L2e, which operated around 23 °C, did not correspond to significantly higher distortion values. This lack of temperature sensitivity on a campaign to campaign basis does not permit a very robust approach to analyzing the temperature effects on distortion. The availability of higher frequency temperature data would allow for a more comprehensive analysis. Temperature effects on distortion over the period of a campaign as modeled using this method do not appear significant in the ICESat IST. It is also possible that temperature effects are negligible relative to the effects of aging, attitude mode, and blinding. The temperature stability of ICESat over the duration of the mission makes the IST less suitable for studying temperature effects on distortion relative to a mission that experiences larger temperature fluctuations, which would be more susceptible to temperature induced star tracker distortion. Temperature effects are not significant in modeling campaign-based distortion of the IST focal plane for the ICESat mission using this method.

4.7 Effects of Star Color on Distortion

Chromatic aberration is a phenomenon that can occur in any imaging sensor where light must first pass through a lens. Because the refractive index of the lens varies for different wavelengths, the position of the light on the focal plane is shifted as a function of the light source's color. Because natural light is polychromatic, this effect can be dispersive, causing shifts in multiple directions determined by

each wavelength. Chromatic aberration can be classified as axial or transverse, where axial chromatic aberration is caused by variations in focal length with wavelength and transverse chromatic aberration is caused by deviations in light position on the focal plane from the nominal position[30]. Because both types of chromatic aberration result in shifted positions in the focal plane, it should be possible to capture these effects using this distortion estimation method. For star tracker applications, these effects manifest as shifts in star centroid position.

In the GLAS catalog, star color is assigned according to the B-V color index. The B-V color index for a given star is obtained by taking the difference between the observed magnitudes in the blue and visible ranges of the spectrum, noting that star magnitudes are defined using an inverse relation such that a smaller apparent magnitude corresponds to a brighter star. The B-V color index for known stars ranges between approximately -0.3 to 5.8. The bluest stars have the lowest B-V color index whereas the reddest stars have the highest. To determine any distortion dependence on star color, it was first necessary to isolate the stars corresponding to a specific range of B-V color index to use in generating the distortion maps. Two histograms were generated to investigate how star color was distributed through the GLAS catalog as well as observed over the entire ICESat mission. The vertical axis defines number of occurrences whereas the horizontal axis defines a star color. Different stars may share the same B-V color index.

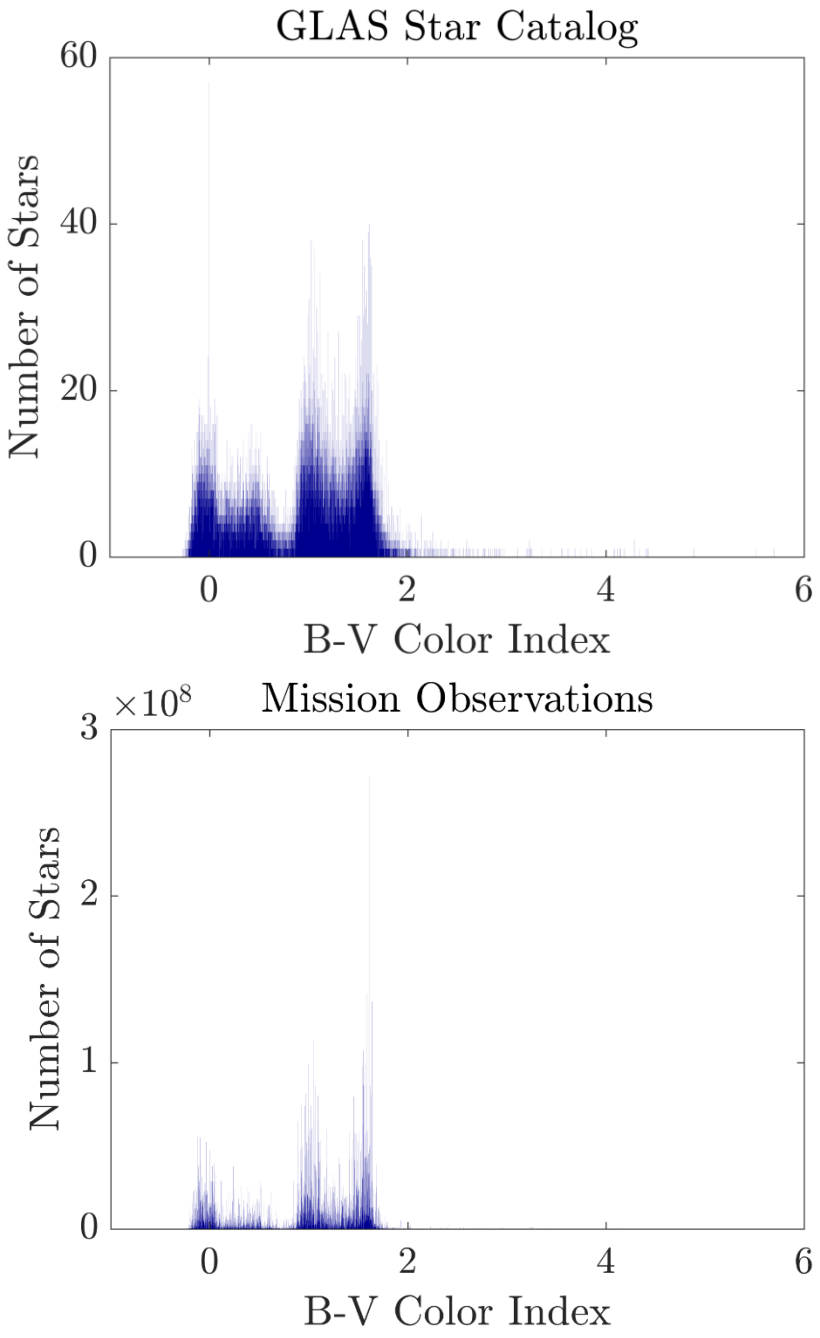

Figure 87: Star color histograms for stars defined in the GLAS star catalog and observed over the ICESat mission.

The histograms indicated that a majority of both observed and catalog stars were defined by a B-V color index below 2. It was decided to investigate the distortion associated with the bluest stars, corresponding to a negative B-V color index. This range was chosen primarily because the extremes of B-V color index, corresponding to blue and red stars, were identified as the greatest sources of chromatic aberration for ICESat-2. Furthermore, there was a greater concentration of observations at the lower end of B-V index, corresponding to bluer stars, than at the higher end, corresponding to redder stars. Histograms were generated for each campaign to determine if the color constraint was too restrictive for any campaign. It was found that the distribution of star colors observed for each campaign was similar and the observations were sufficient in number to effectively span the FOV. It was expected that the color distribution of observed stars match that of the catalog, but because stars at higher magnitude declinations are observed more frequently due to the inclination of ICESat's orbit and the precession of its orbital plane, this is not the case. The peak in star observations at a B-V color index of 1.61 suggests that there are a higher number of stars of this magnitude near the poles or possibly the existence of a hot spot corresponding to the same observed magnitude. It is unlikely that the magnitude corresponds to a hot spot, since the star observations included here were all successfully identified.

Further analysis was conducted to determine the effect that downsampling the star observations would have on the distortion map, since isolating blue stars would be reducing the available data. L3a was chosen as the campaign of study to better understand the effects of downsampling. By artificially downsampling the data from the original 10 Hz sampling rate, it was possible to determine where the

distortion map began to significantly degrade from the original. The downsampling results from campaign L3a are represented in Figure 88. The degree of downsampling is represented in terms of percentage of total observations; however, these percentages coincide with sampling frequencies corresponding to 10 Hz through 1e-3 Hz. Maximum distortion over the FOV was used as the metric to identify degradation of stability. Because there are large regions of low distortion near the center of the distortion map, changes in the average distortion value are subtle and less useful in this analysis.

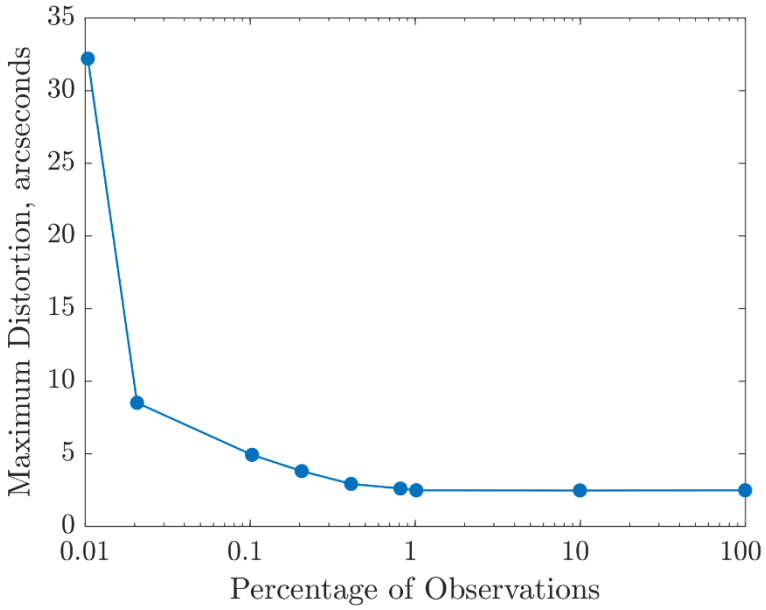

Figure 88: Effects of downsampling star observations on maximum estimated distortion for ICESat campaign L3a.

The maximum distortion remains stable for a reduction of observations to approximately 1% of the total which corresponds to a sampling rate reduction from 10 Hz to 0.1 Hz, suggesting there should be enough star observations to build a

stable distortion map if the reduction in observations does not exceed the specified threshold.

The distortion maps generated for each campaign using stars with a negative B-V color index are shown in the figures below. These color-dependent distortion maps can be generated for ranges of B-V color index to directly estimate and correct for chromatic aberration. Distortion can then be estimated as a function of both color and position in the focal plane, allowing for the generation of unique corrections of observed star positions based upon their associated B-V color index. This allows for more robust reduction in uncertainty in attitude estimates through compensation for chromatic aberration effects.

4.7.1 Campaign L1a

There were 13,725,602 blue stars observed by the IST during campaign L1a. This represents 9% of the total observations for this campaign. The distortion map, distortion vector map, and star density maps generated from these blue star observations are provided in the figures below.

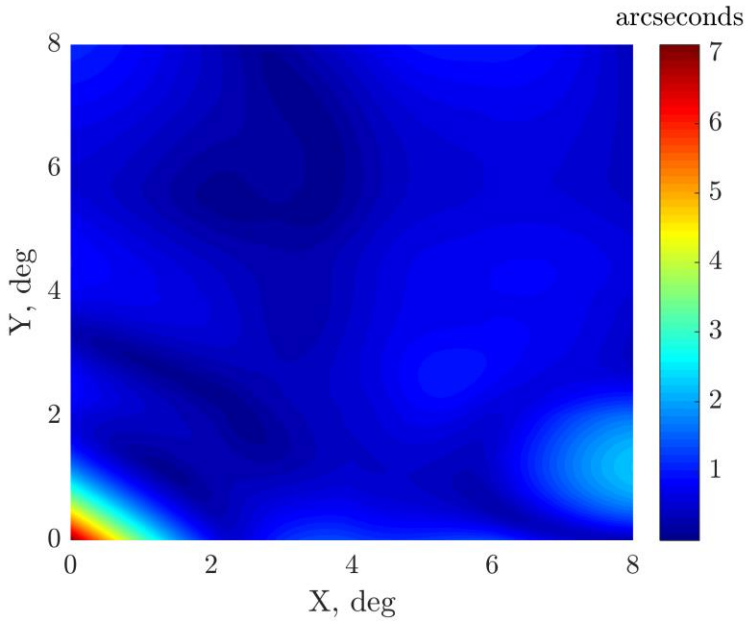

Figure 89: Distortion map for the ICESat IST, generated from blue star observations collected during campaign L1a.

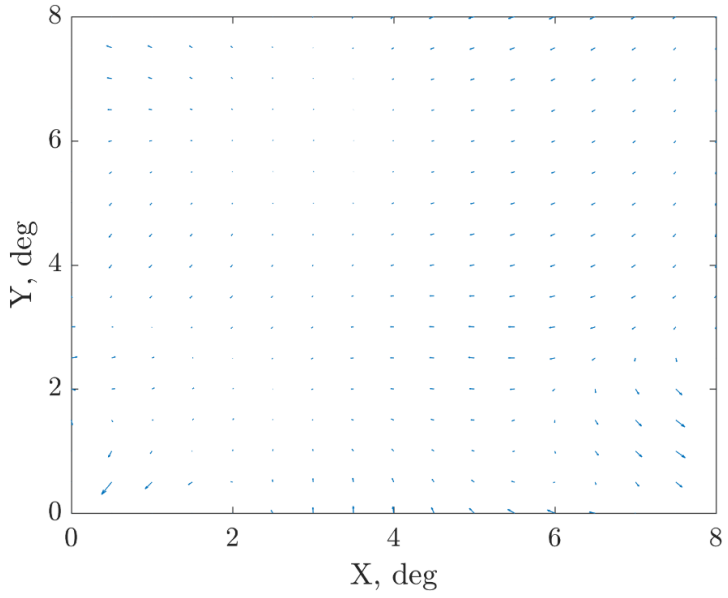

Figure 90: Distortion vector map for the ICESat IST, generated from blue star observations collected during campaign L1a.

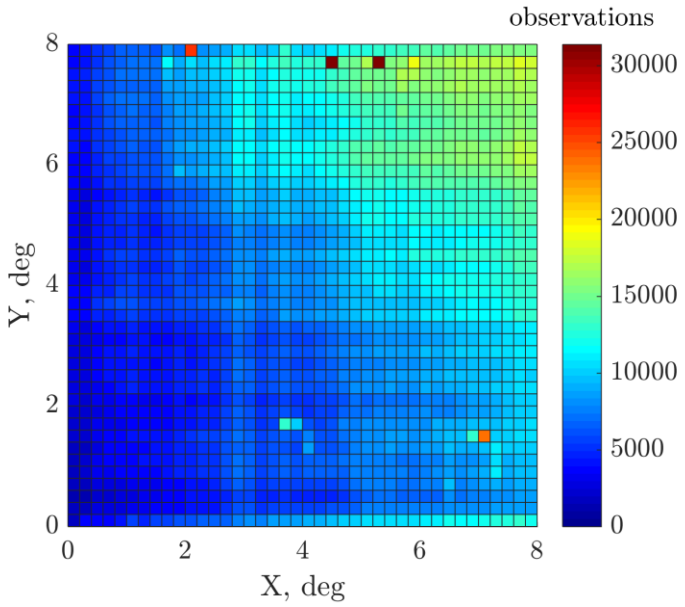

Figure 91: Star density map for the ICESat IST, generated from blue star observations collected during campaign L1a

4.7.2 Campaign L2a

There were 24,175,417 blue stars observed by the IST during campaign L2a. This represents 10% of the total observations for this campaign. The distortion map, distortion vector map, and star density maps generated from these blue star observations are provided in the figures below.

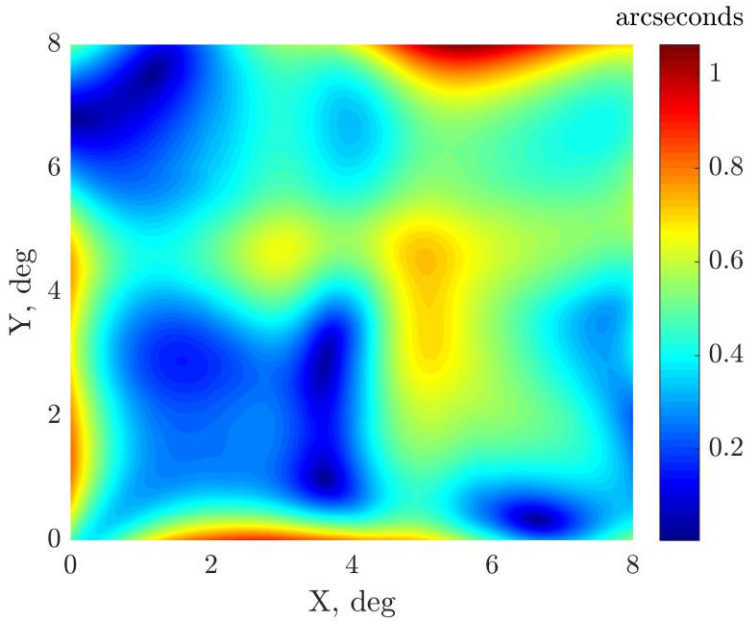

Figure 92: Distortion map for the ICESat IST, generated from blue star observations collected during campaign L2a.

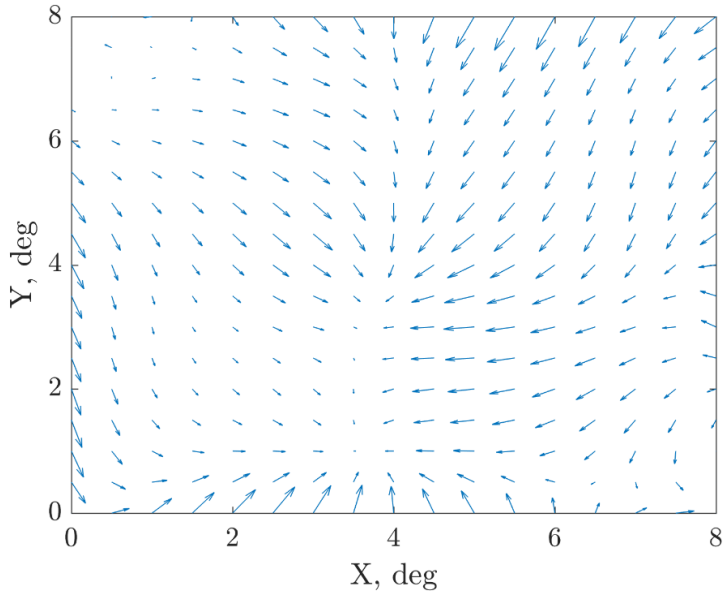

Figure 93: Distortion vector map for the ICESat IST, generated from blue star observations collected during campaign L2a.

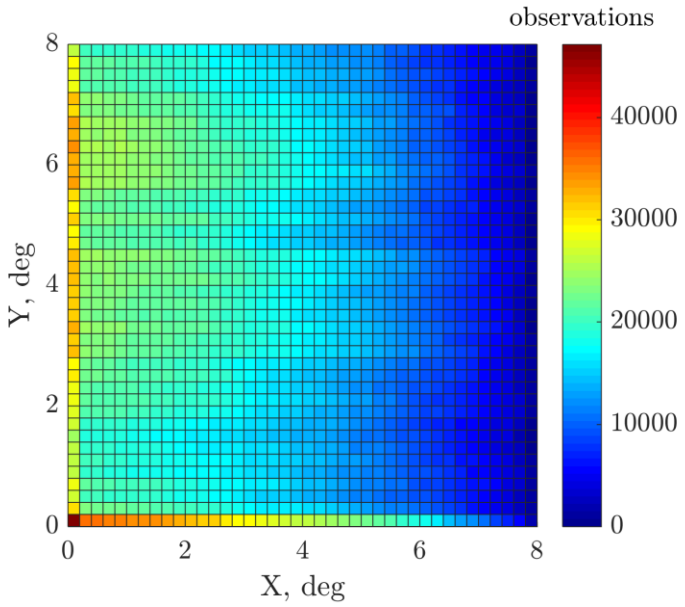

Figure 94: Star density map for the ICESat IST, generated from blue star observations collected during campaign L2a.

4.7.3 Campaign L2b

There were 16,474,292 blue stars observed by the IST during campaign L2b. This represents 12% of the total observations for this campaign. The distortion map, distortion vector map, and star density maps generated from these blue star observations are provided in the figures below.

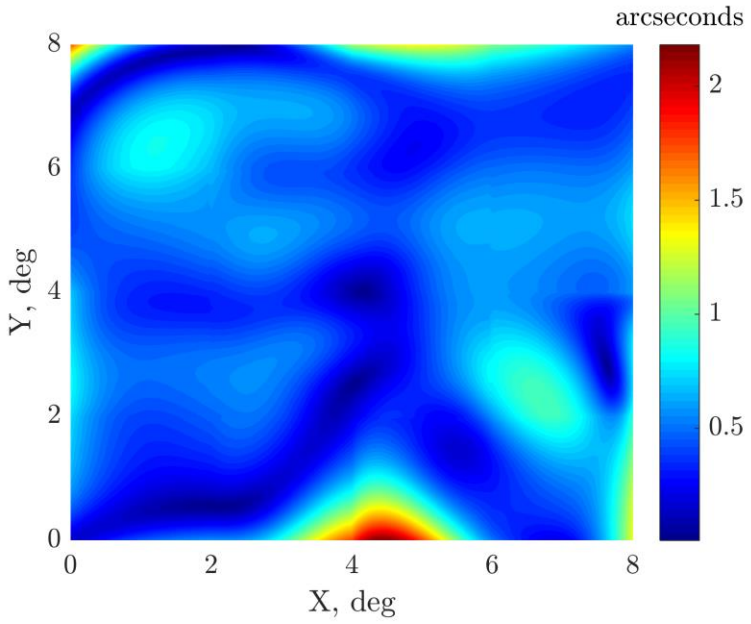

Figure 95: Distortion map for the ICESat IST, generated from blue star observations collected during campaign L2b.

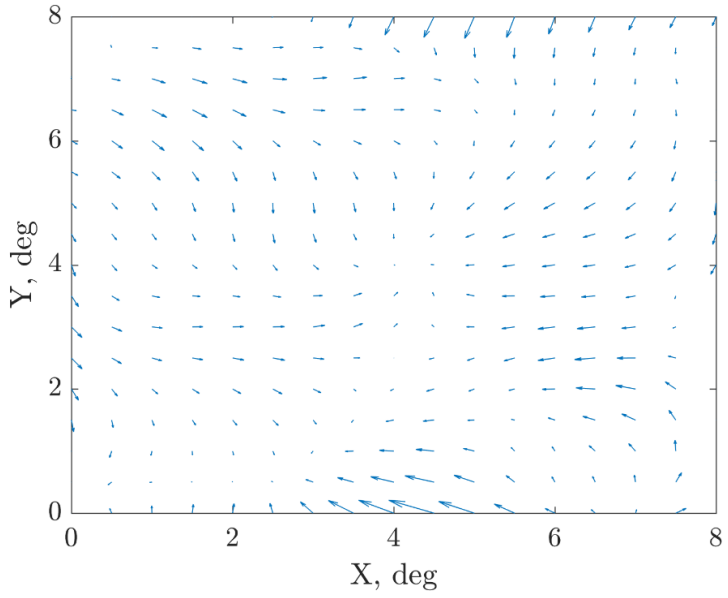

Figure 96: Distortion vector map for the ICESat IST, generated from blue star observations collected during campaign L2b.

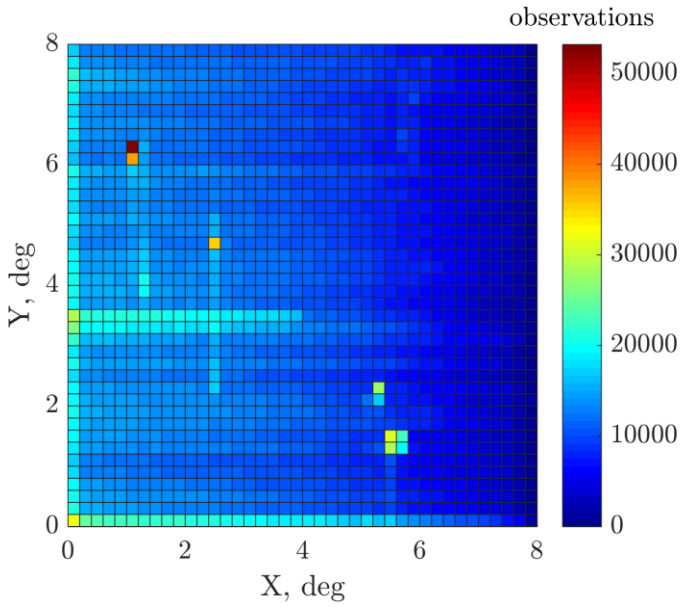

Figure 97: Star density map for the ICESat IST, generated from blue star observations collected during campaign L2b.

4.7.4 Campaign L2c

There were 15,330,022 blue stars observed by the IST during campaign L2c. This represents 11% of the total observations for this campaign. The distortion map, distortion vector map, and star density maps generated from these blue star observations are provided in the figures below.

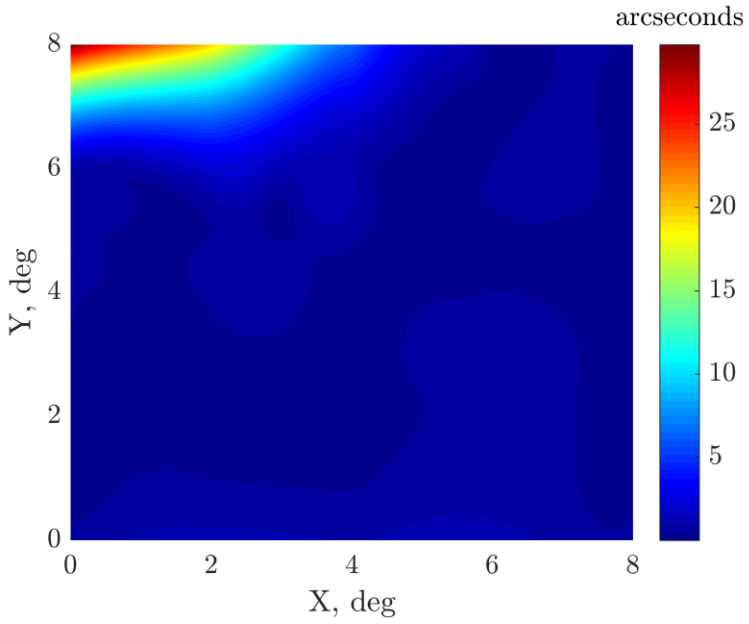

Figure 98: Distortion map for the ICESat IST, generated from blue star observations collected during campaign L2c.

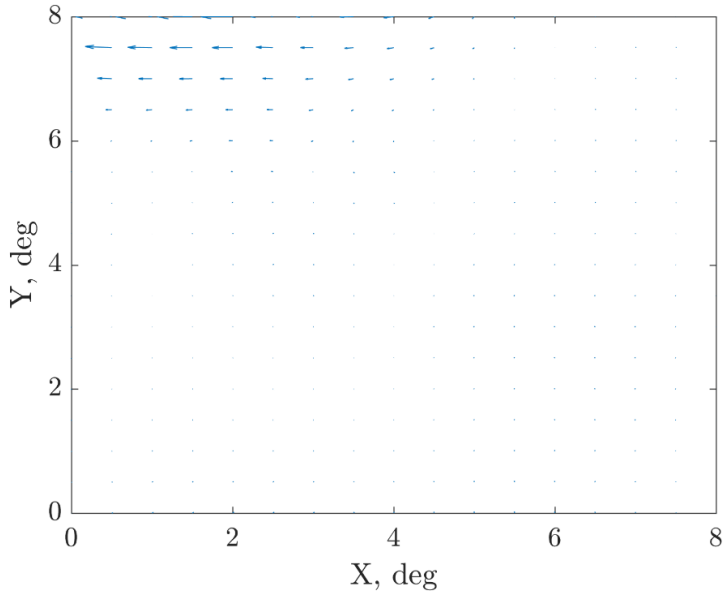

Figure 99: Distortion vector map for the ICESat IST, generated from blue star observations collected during campaign L2c.

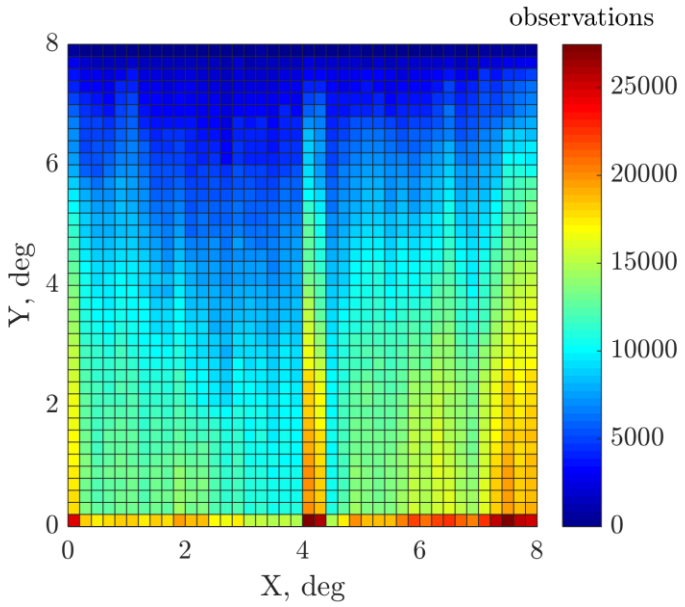

Figure 100: Star density map for the ICESat IST, generated from blue star observations collected during campaign L2c.

4.7.5 Campaign L3a

There were 14,408,016 blue stars observed by the IST during campaign L3a. This represents 9% of the total observations for this campaign. The distortion map, distortion vector map, and star density maps generated from these blue star observations are provided in the figures below.

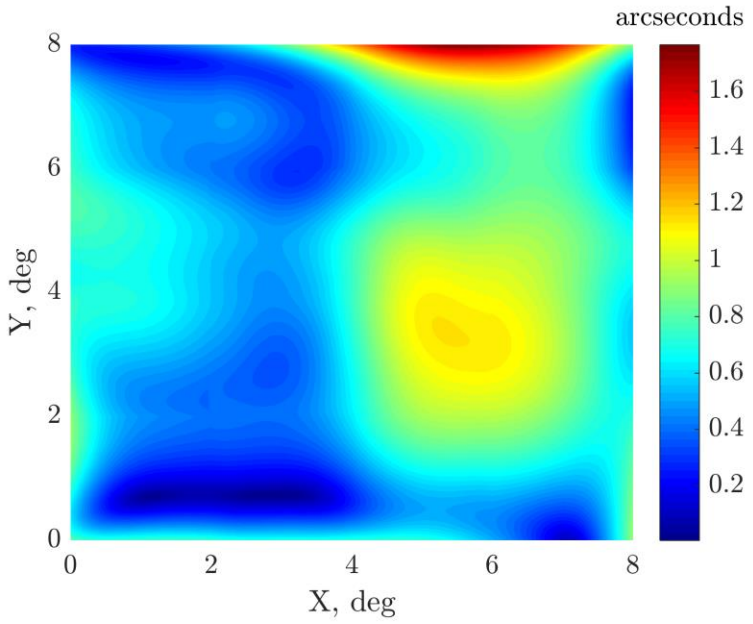

Figure 101: Distortion map for the ICESat IST, generated from blue star observations collected during campaign L3a.

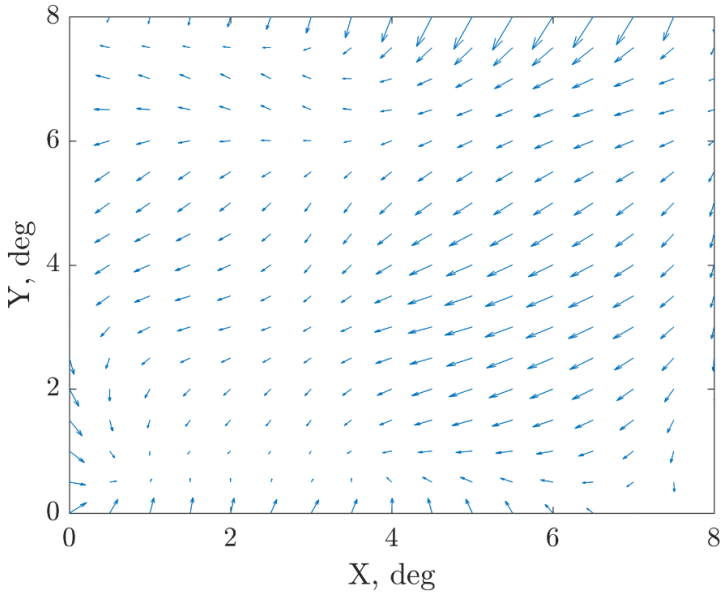

Figure 102: Distortion vector map for the ICESat IST, generated from blue star observations collected during campaign L3a.

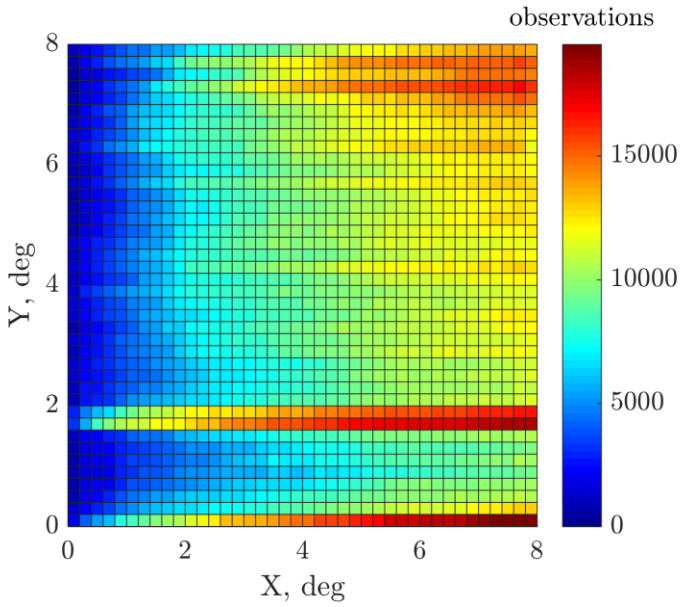

Figure 103: Star density map for the ICESat IST, generated from blue star observations collected during campaign L3a.

4.7.6 Campaign L3b

There were 14,146,968 blue stars observed by the IST during campaign L3b. This represents 9% of the total observations for this campaign. The distortion map, distortion vector map, and star density maps generated from these blue star observations are provided in the figures below.

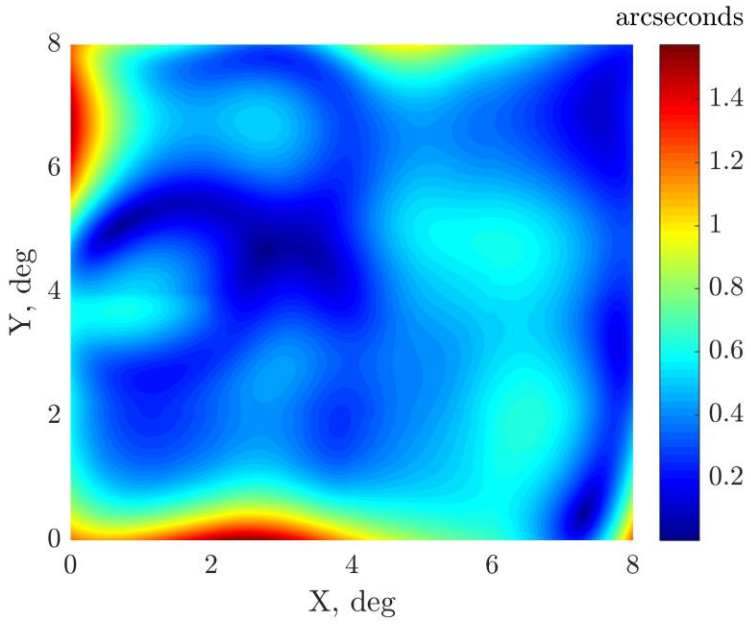

Figure 104: Distortion map for the ICESat IST, generated from blue star observations collected during campaign L3b.

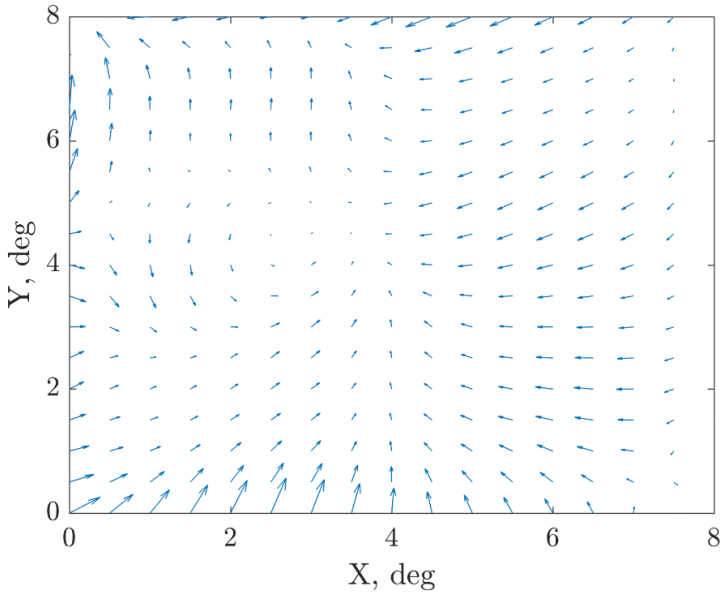

Figure 105: Distortion vector map for the ICESat IST, generated from blue star observations collected during campaign L3b.

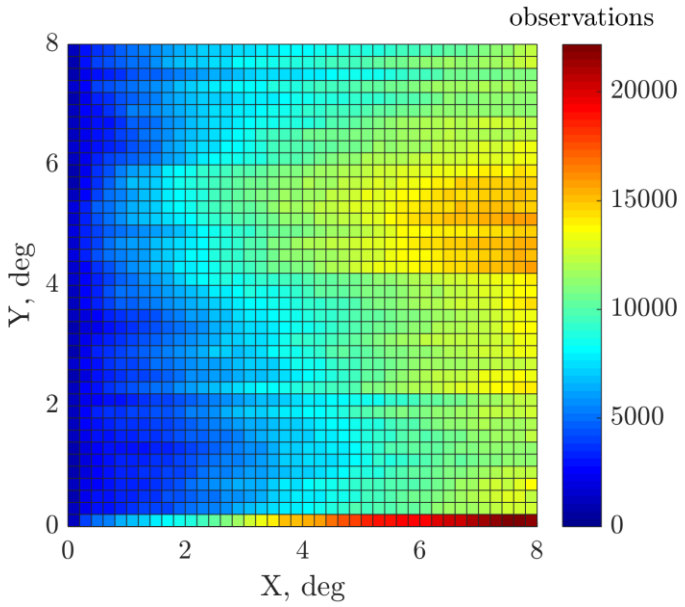

Figure 106: Star density map for the ICESat IST, generated from blue star observations collected during campaign L3b

4.7.7 Campaign L3c

There were 13,987,672 blue stars observed by the IST during campaign L3c. This represents 10% of the total observations for this campaign. The distortion map, distortion vector map, and star density maps generated from these blue star observations are provided in the figures below.

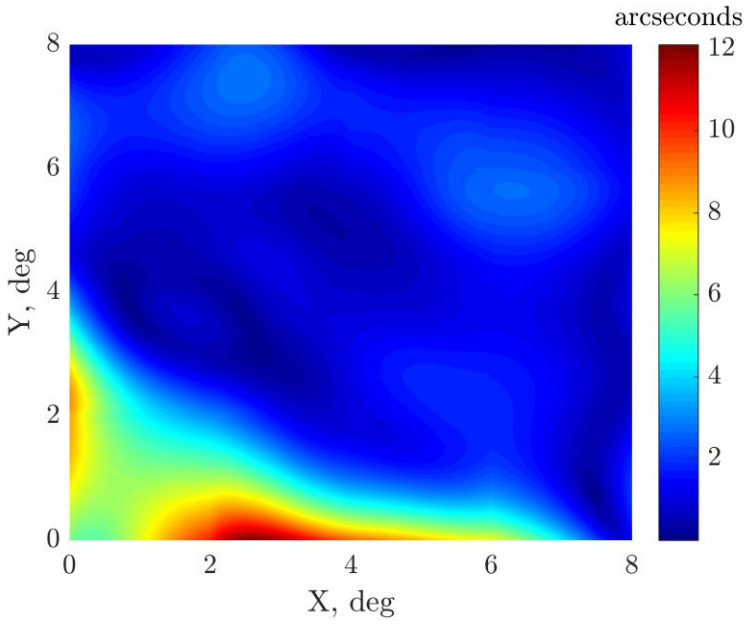

Figure 107: Distortion map for the ICESat IST, generated from blue star observations collected during campaign L3c.

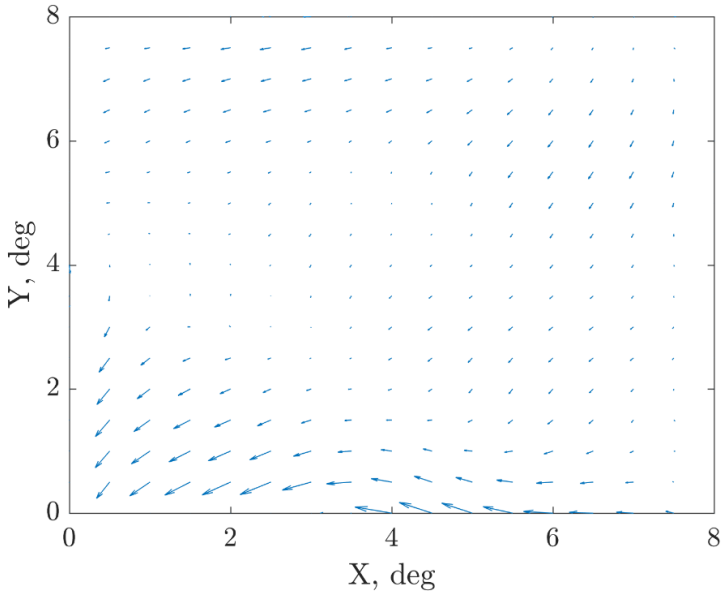

Figure 108: Distortion vector map for the ICESat IST, generated from blue star observations collected during campaign L3c.

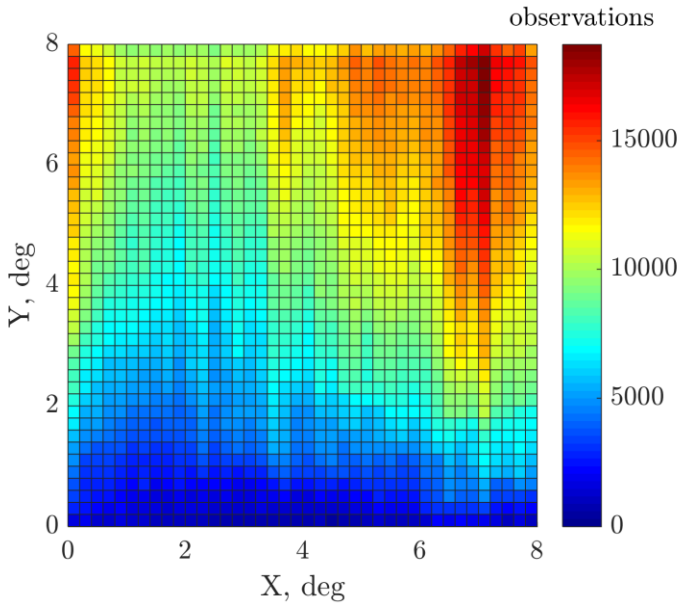

Figure 109: Star density map for the ICESat IST, generated from blue star observations collected during campaign L3c.

4.7.8 Campaign L3d

There were 14,279,997 blue stars observed by the IST during campaign L3d. This represents 9% of the total observations for this campaign. The distortion map, distortion vector map, and star density maps generated from these blue star observations are provided in the figures below.

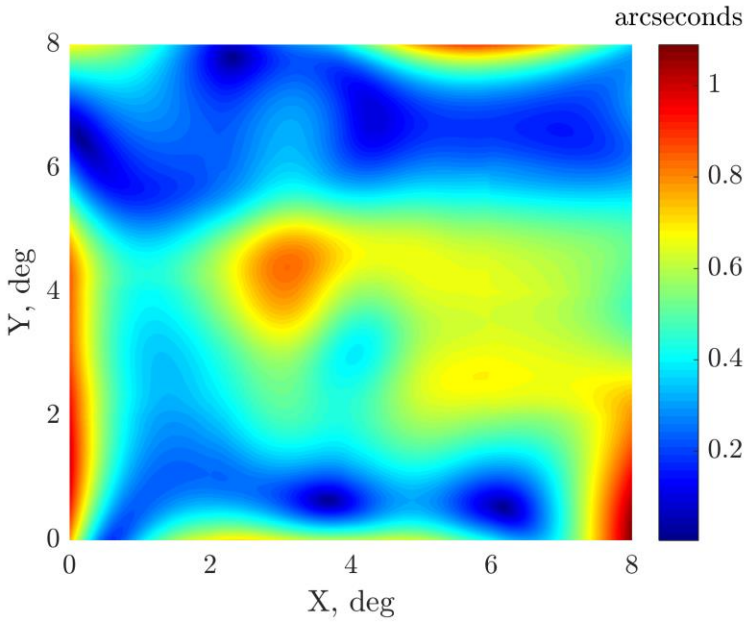

Figure 110: Distortion map for the ICESat IST, generated from blue star observations collected during campaign L3d.

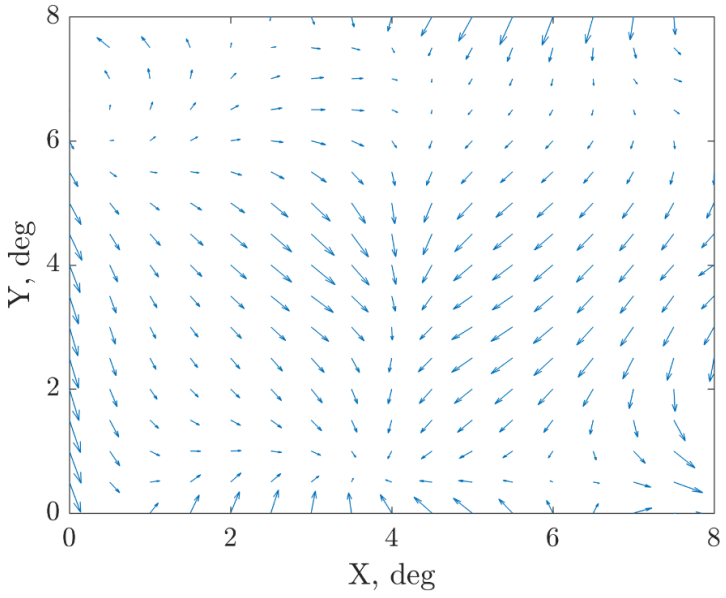

Figure 111: Distortion vector map for the ICESat IST, generated from blue star observations collected during campaign L3d.

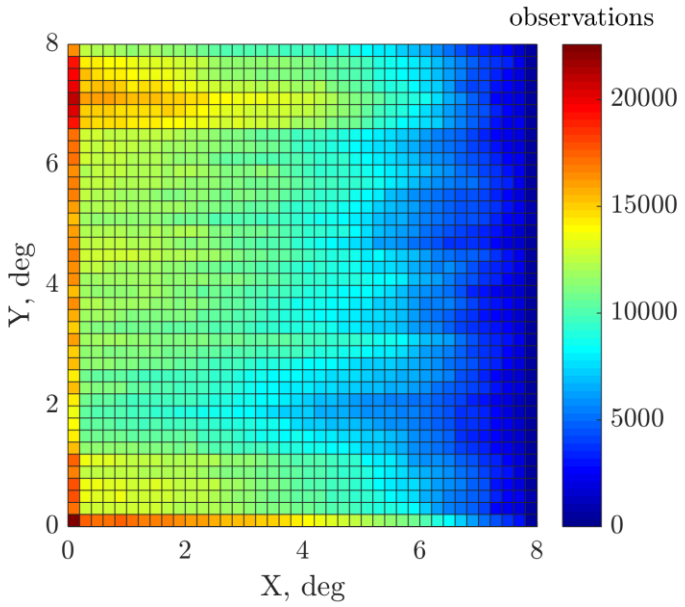

Figure 112: Star density map for the ICESat IST, generated from blue star observations collected during campaign L3d.

4.7.9 Campaign L3e

There were 17,959,592 blue stars observed by the IST during campaign L3e. This represents 11% of the total observations for this campaign. The distortion map, distortion vector map, and star density maps generated from these blue star observations are provided in the figures below.

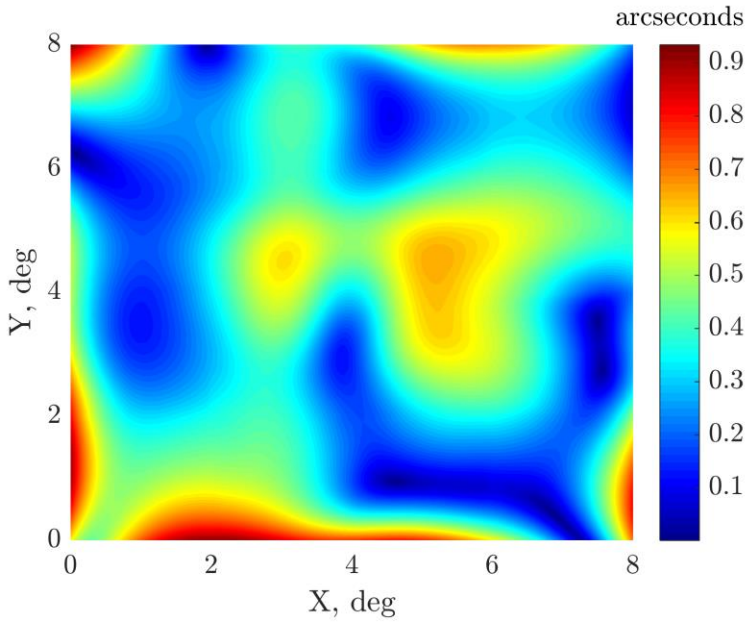

Figure 113: Distortion map for the ICESat IST, generated from blue star observations collected during campaign L3e.

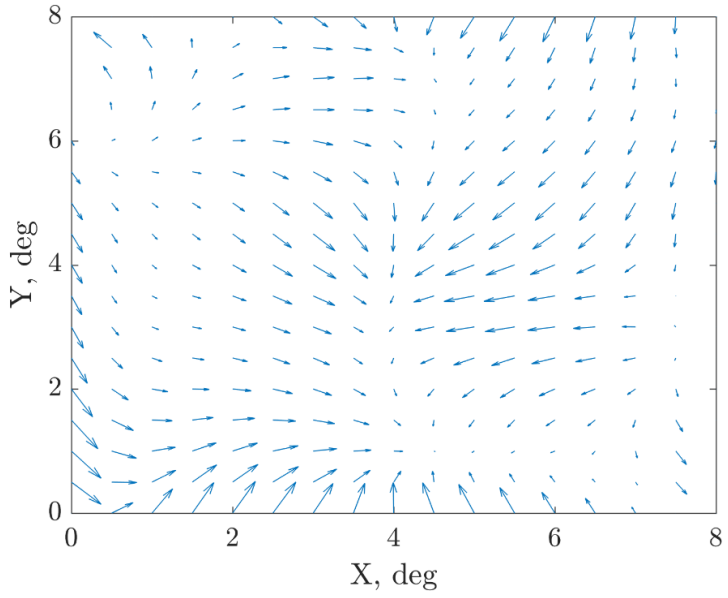

Figure 114: Distortion vector map for the ICESat IST, generated from blue star observations collected during campaign L3e.

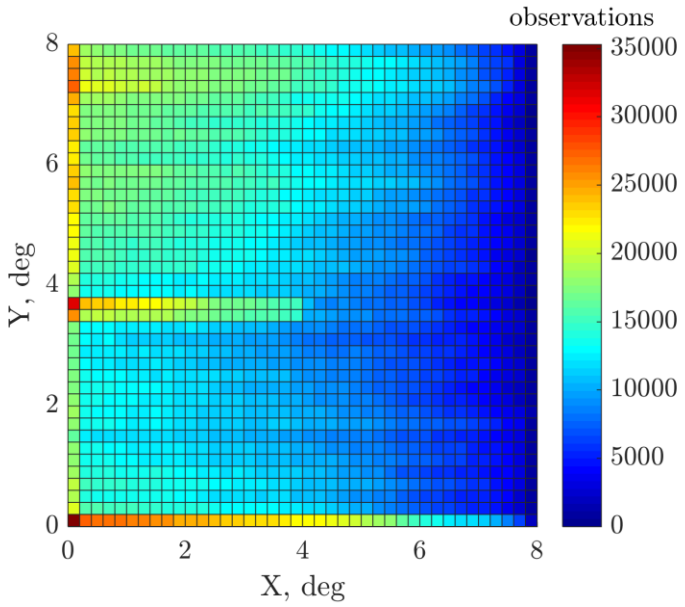

Figure 115: Star density map for the ICESat IST, generated from blue star observations collected during campaign L3e.

4.7.10 Campaign L3f

There were 17,314,005 blue stars observed by the IST during campaign L3f. This represents 13% of the total observations for this campaign. The distortion map, distortion vector map, and star density maps generated from these blue star observations are provided in the figures below.

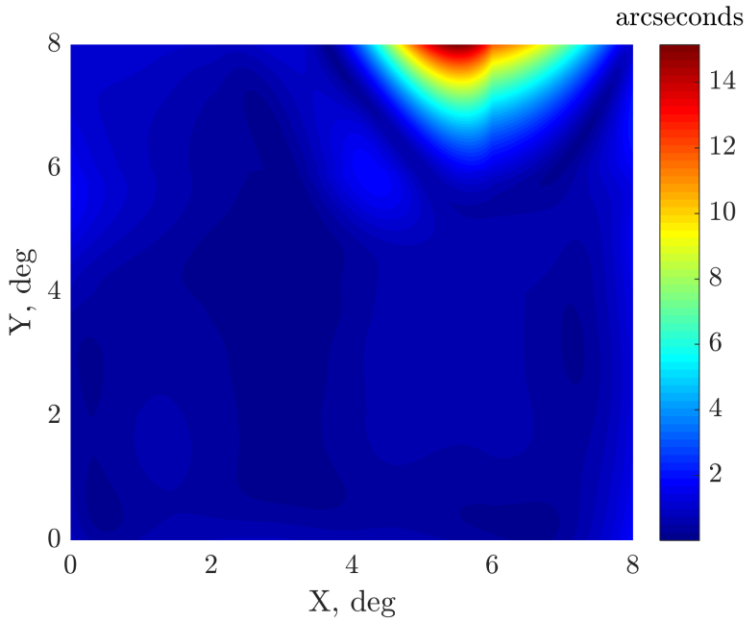

Figure 116: Distortion map for the ICESat IST, generated from blue star observations collected during campaign L3f.

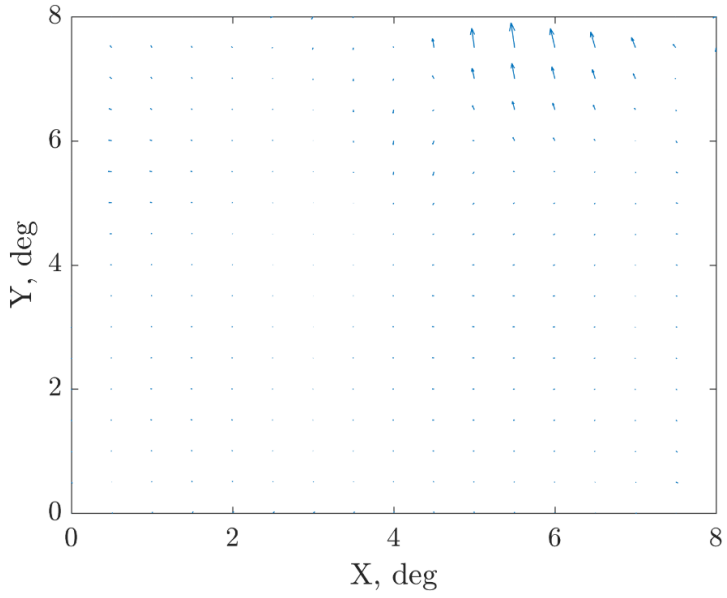

Figure 117: Distortion vector map for the ICESat IST, generated from blue star observations collected during campaign L3f.

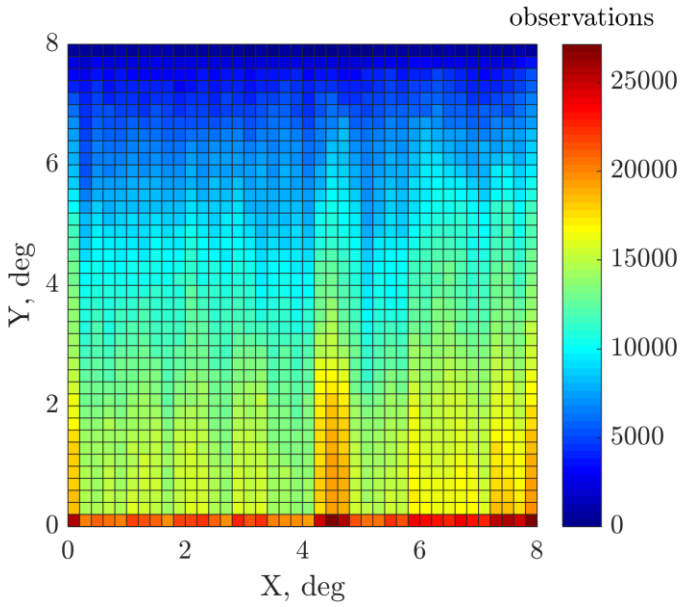

Figure 118: Star density map for the ICESat IST, generated from blue star observations collected during campaign L3f.

4.7.11 Campaign L3g

There were 12,475,811 blue stars observed by the IST during campaign L3g. This represents 9% of the total observations for this campaign. The distortion map, distortion vector map, and star density maps generated from these blue star observations are provided in the figures below.

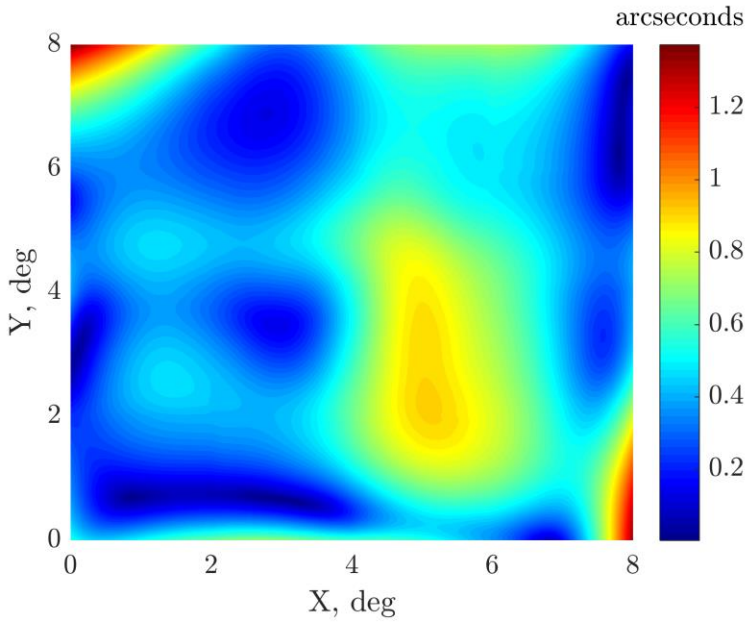

Figure 119: Distortion map for the ICESat IST, generated from blue star observations collected during campaign L3g.

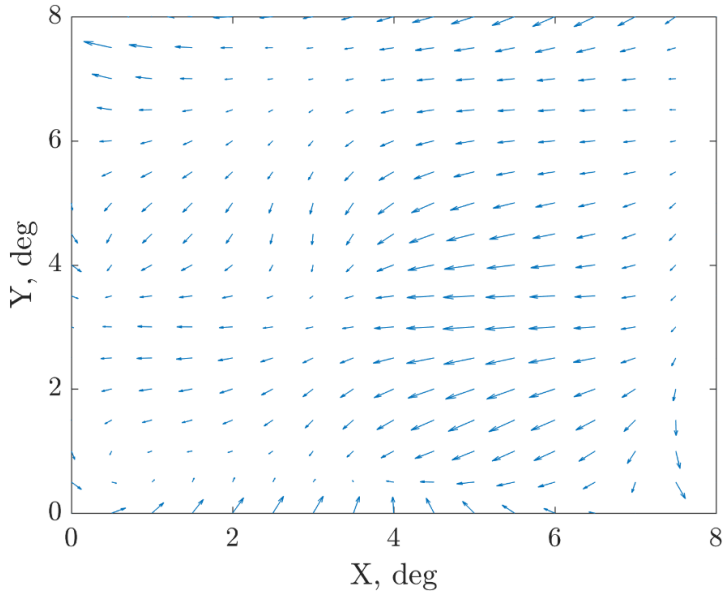

Figure 120: Distortion vector map for the ICESat IST, generated from blue star observations collected during campaign L3g.

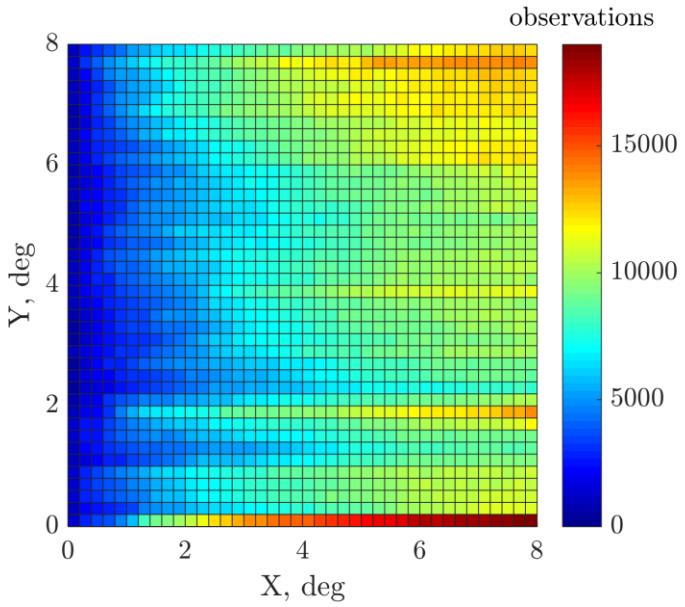

Figure 121: Star density map for the ICESat IST, generated from blue star observations collected during campaign L3g.

4.7.12 Campaign L3h

There were 19,372,410 blue stars observed by the IST during campaign L3h. This represents 13% of the total observations for this campaign. The distortion map, distortion vector map, and star density maps generated from these blue star observations are provided in the figures below.

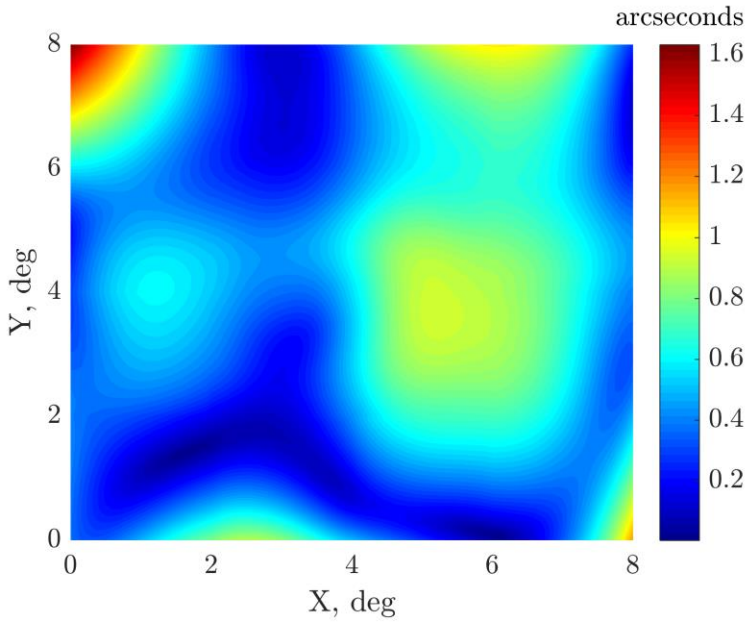

Figure 122: Distortion map for the ICESat IST, generated from blue star observations collected during campaign L3h.

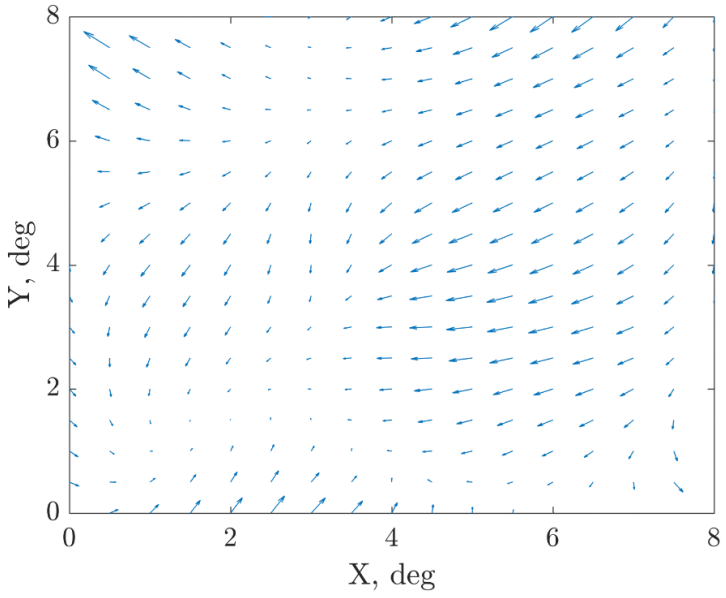

Figure 123: Distortion vector map for the ICESat IST, generated from blue star observations collected during campaign L3h.

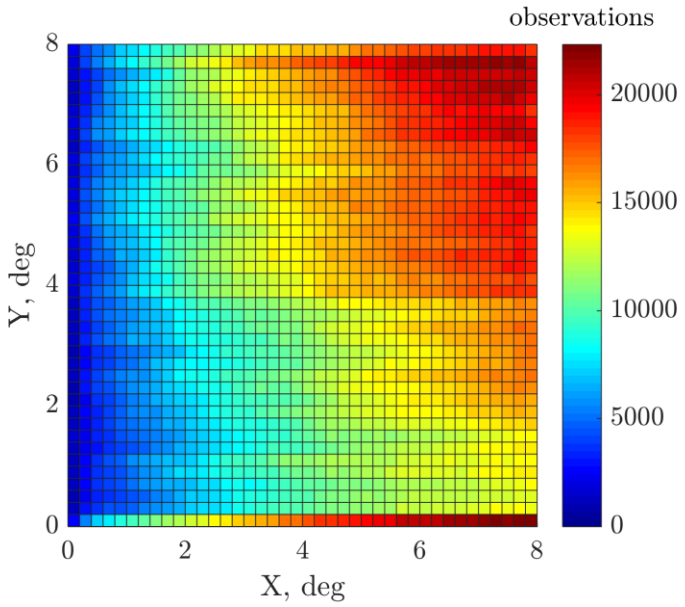

Figure 124: Star density map for the ICESat IST, generated from blue star observations collected during campaign L3h.

4.7.13 Campaign L3i

There were 13,070,493 blue stars observed by the IST during campaign L3i. This represents 9% of the total observations for this campaign. The distortion map, distortion vector map, and star density maps generated from these blue star observations are provided in the figures below.

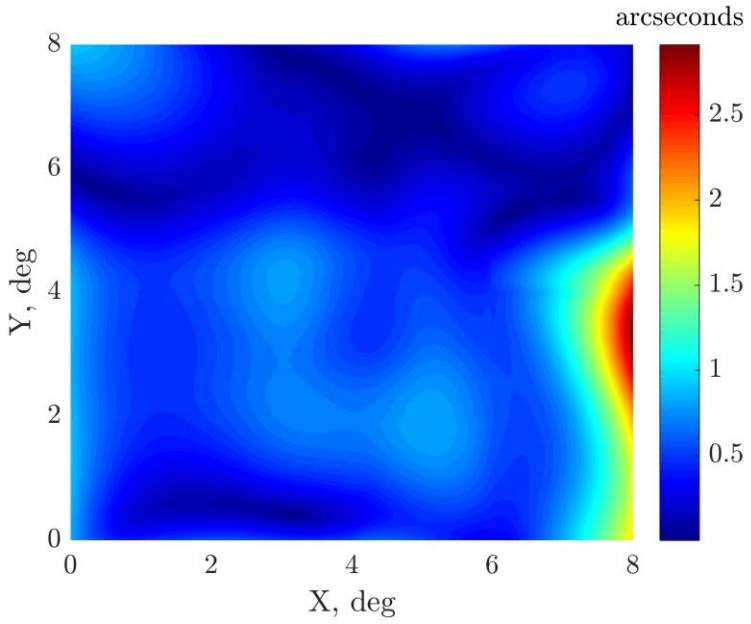

Figure 125: Distortion map for the ICESat IST, generated from blue star observations collected during campaign L3i.

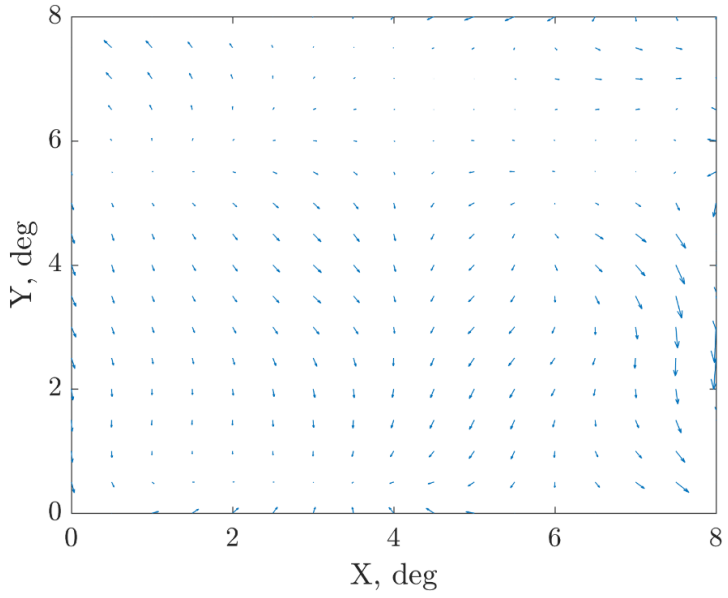

Figure 126: Distortion vector map for the ICESat IST, generated from blue star observations collected during campaign L3i.

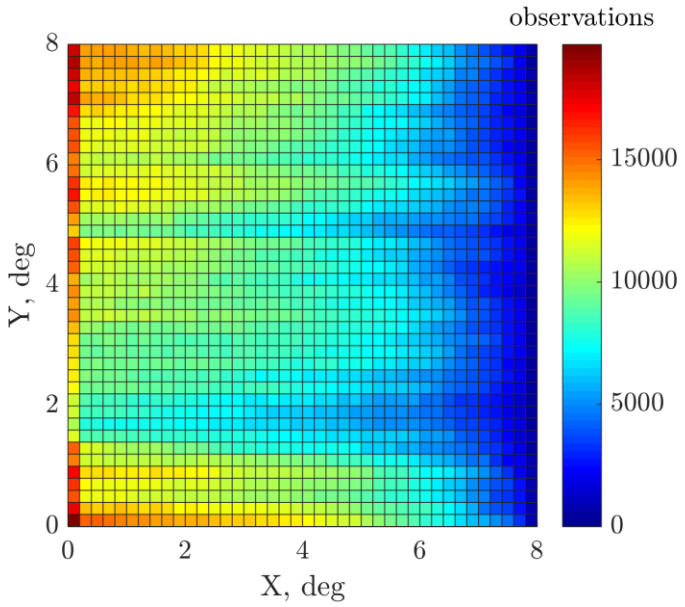

Figure 127: Star density map for the ICESat IST, generated from blue star observations collected during campaign L3i.

4.7.14 Campaign L3j

There were 23,236,985 blue stars observed by the IST during campaign L3j. This represents 15% of the total observations for this campaign. The distortion map, distortion vector map, and star density maps generated from these blue star observations are provided in the figures below.

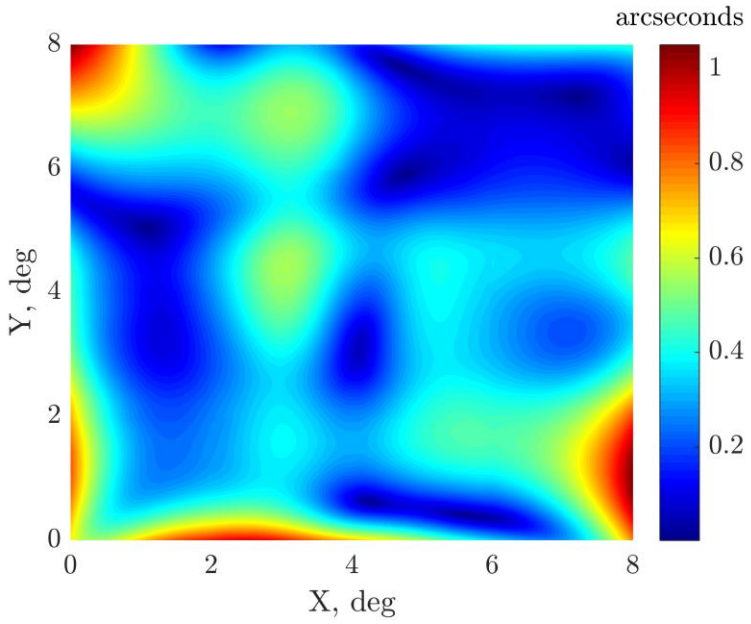

Figure 128: Distortion map for the ICESat IST, generated from blue star observations collected during campaign L3j.

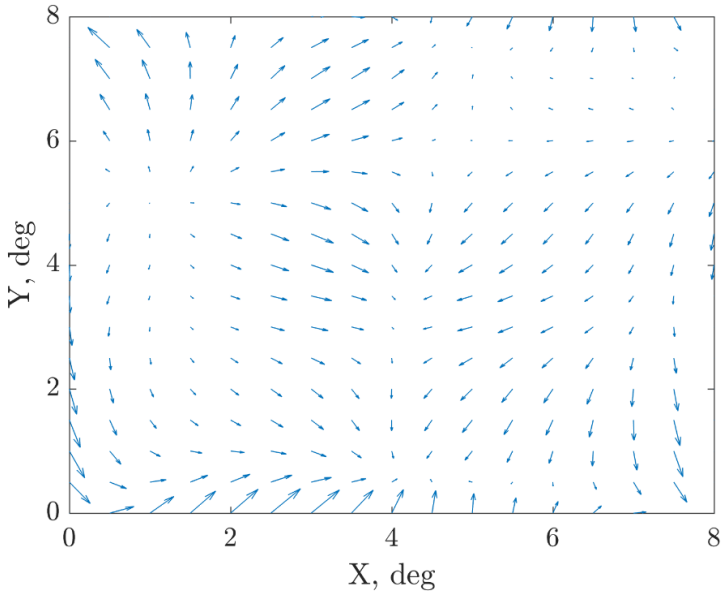

Figure 129: Distortion vector map for the ICESat IST, generated from blue star observations collected during campaign L3j.

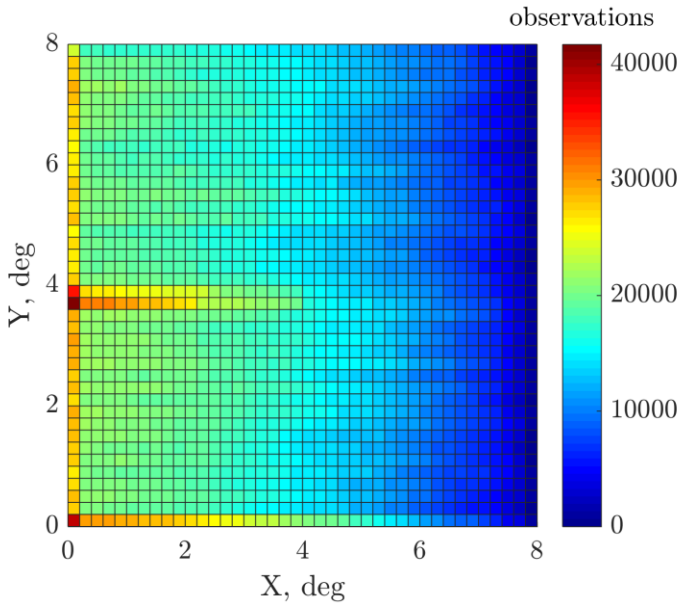

Figure 130: Star density map for the ICESat IST, generated from blue star observations collected during campaign L3j.

4.7.15 Campaign L3k

There were 6,263,193 blue stars observed by the IST during campaign L3k. This represents 9% of the total observations for this campaign. The distortion map, distortion vector map, and star density maps generated from these blue star observations are provided in the figures below.

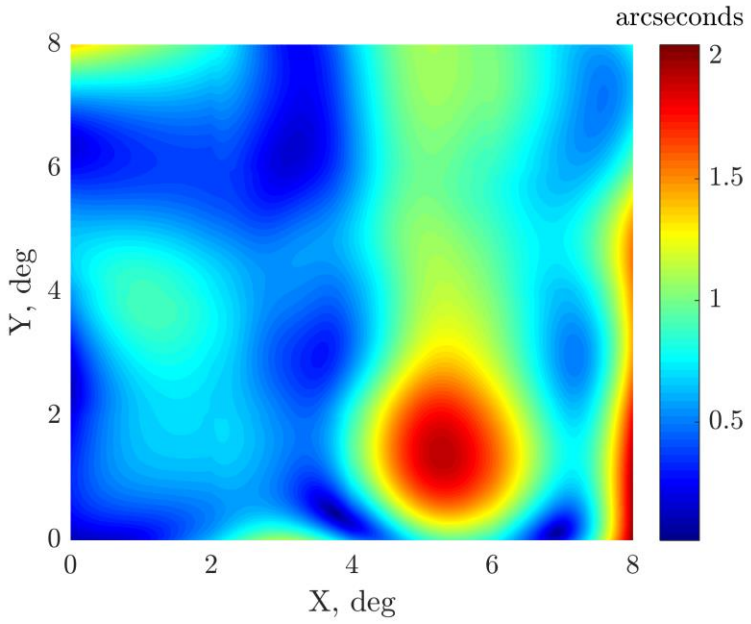

Figure 131: Distortion map for the ICESat IST, generated from blue star observations collected during campaign L3k.

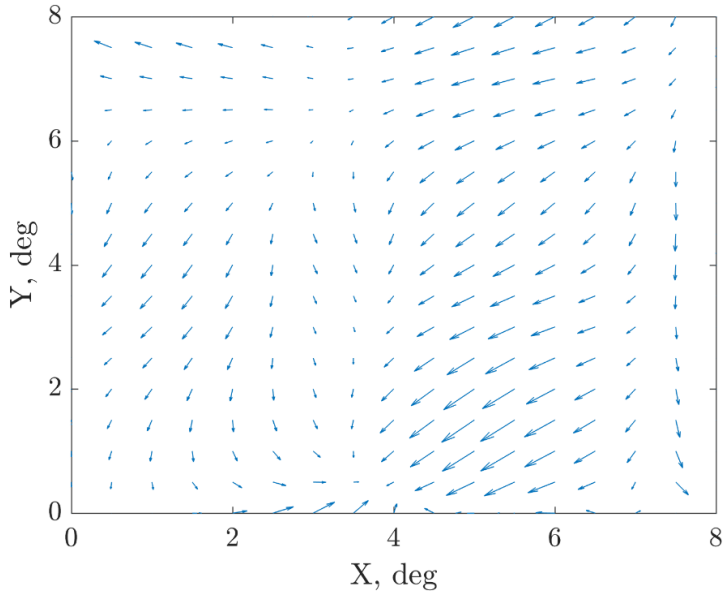

Figure 132: Distortion vector map for the ICESat IST, generated from blue star observations collected during campaign L3k.

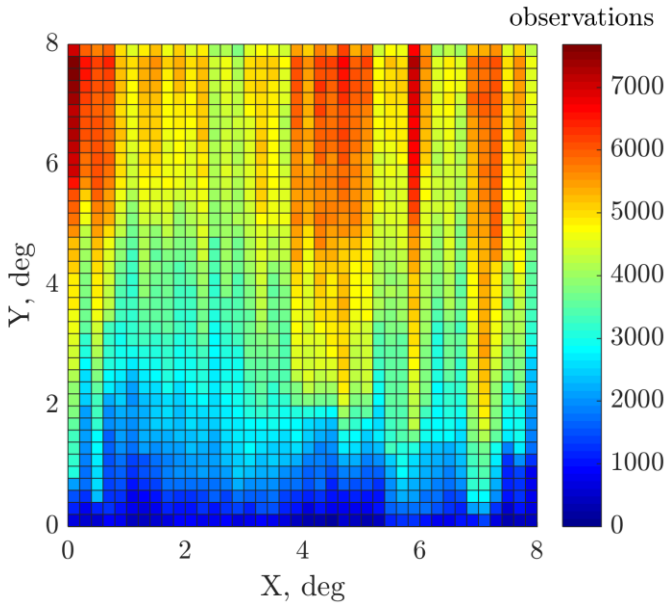

Figure 133: Star density map for the ICESat IST, generated from blue star observations collected during campaign L3k.

4.7.16 Campaign L2d

There were 8,295,944 blue stars observed by the IST during campaign L2d. This represents 9% of the total observations for this campaign. The distortion map, distortion vector map, and star density maps generated from these blue star observations are provided in the figures below.

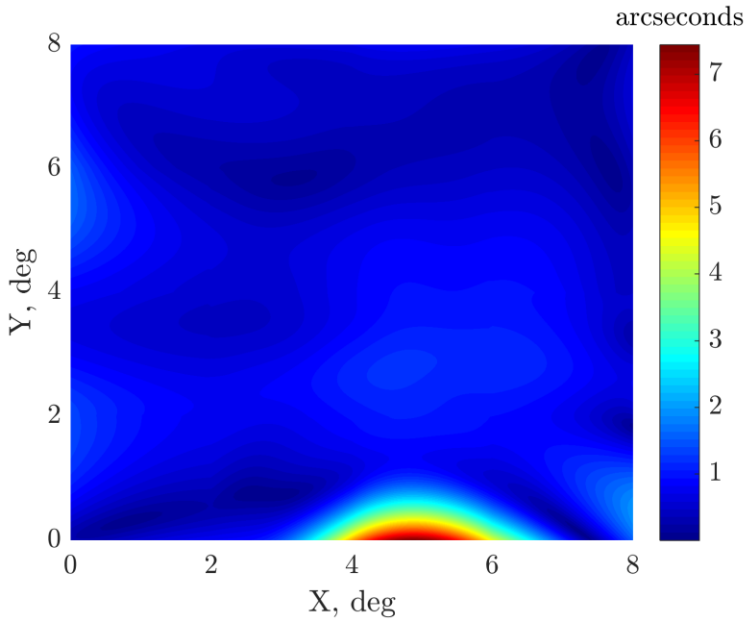

Figure 134: Distortion map for the ICESat IST, generated from blue star observations collected during campaign L2d.

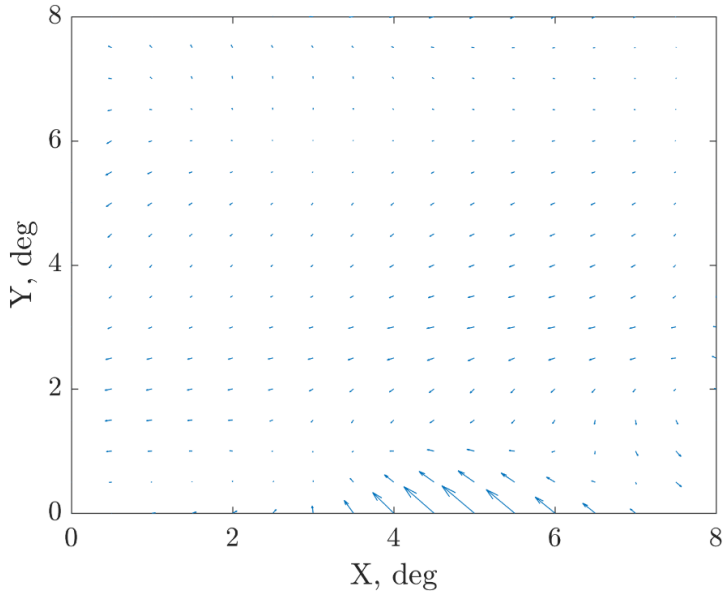

Figure 135: Distortion vector map for the ICESat IST, generated from blue star observations collected during campaign L2d.

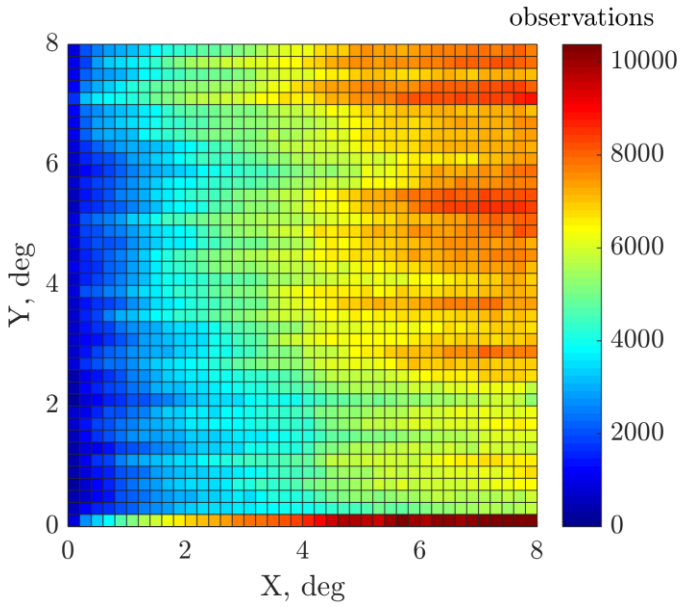

Figure 136: Star density map for the ICESat IST, generated from blue star observations collected during campaign L2d.

4.7.17 Campaign L2e

There were 17,259,138 blue stars observed by the IST during campaign L2e. This represents 11% of the total observations for this campaign. The distortion map, distortion vector map, and star density maps generated from these blue star observations are provided in the figures below.

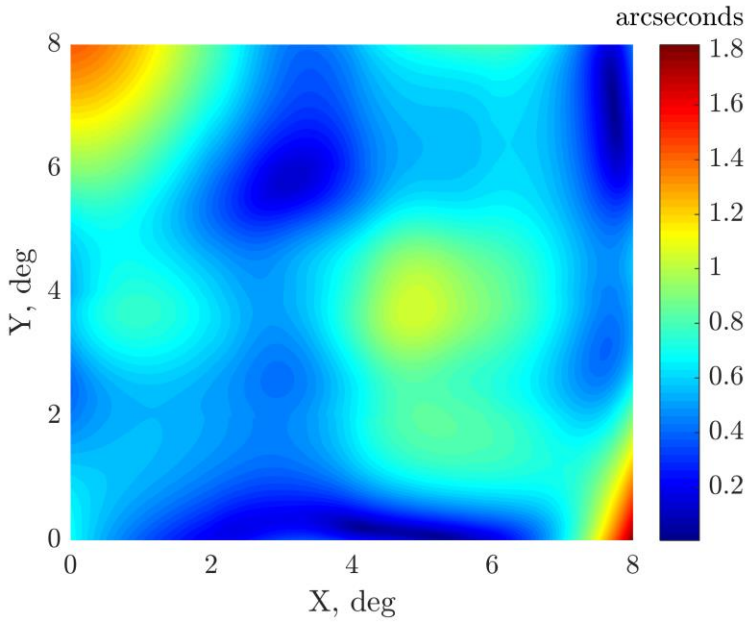

Figure 137: Distortion map for the ICESat IST, generated from blue star observations collected during campaign L2e.

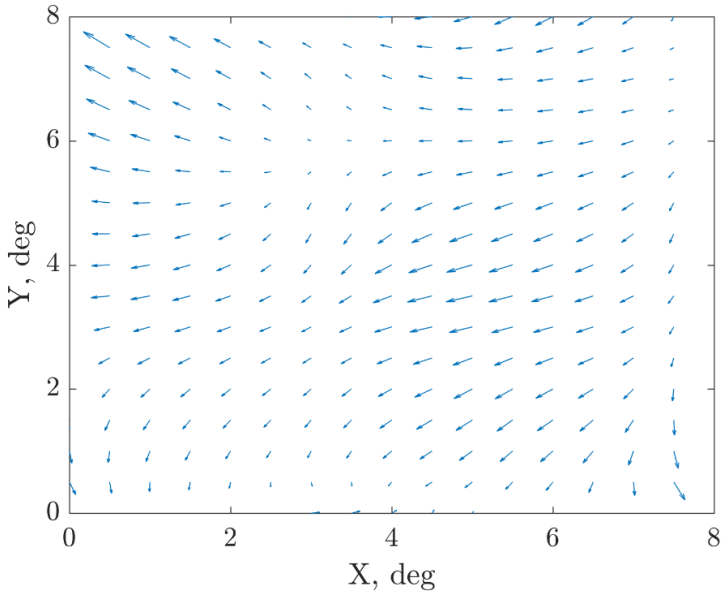

Figure 138: Distortion vector map for the ICESat IST, generated from blue star observations collected during campaign L2e.

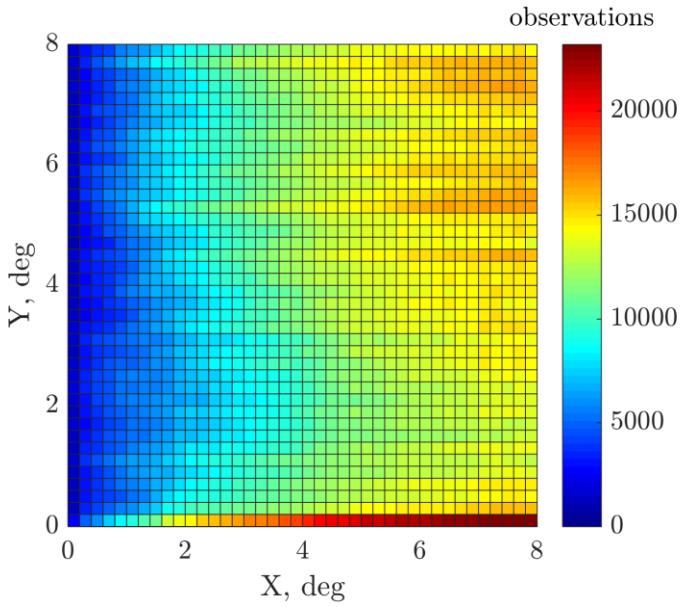

Figure 139: Star density map for the ICESat IST, generated from blue star observations collected during campaign L2e.

4.7.18 Campaign L2f

There were 3,726,107 blue stars observed by the IST during campaign L2f. This represents 8% of the total observations for this campaign. The distortion map, distortion vector map, and star density maps generated from these blue star observations are provided in the figures below.

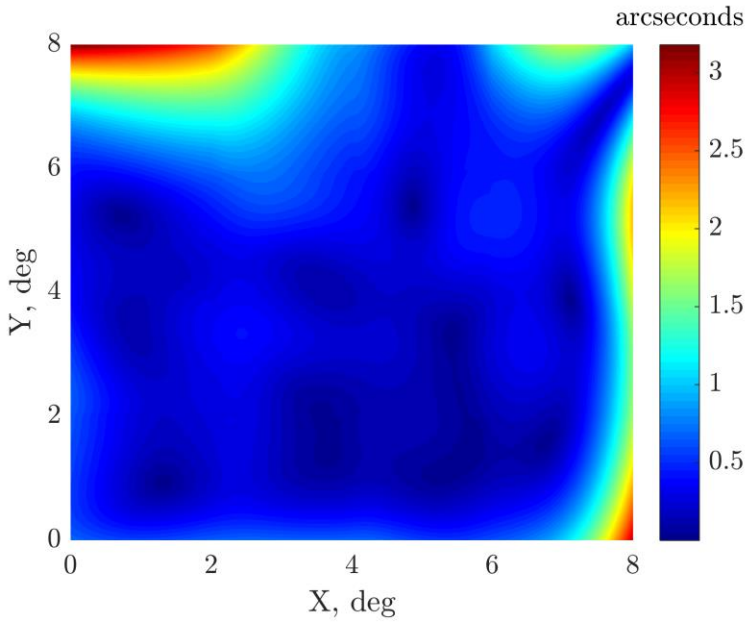

Figure 140: Distortion map for the ICESat IST, generated from blue star observations collected during campaign L2f.

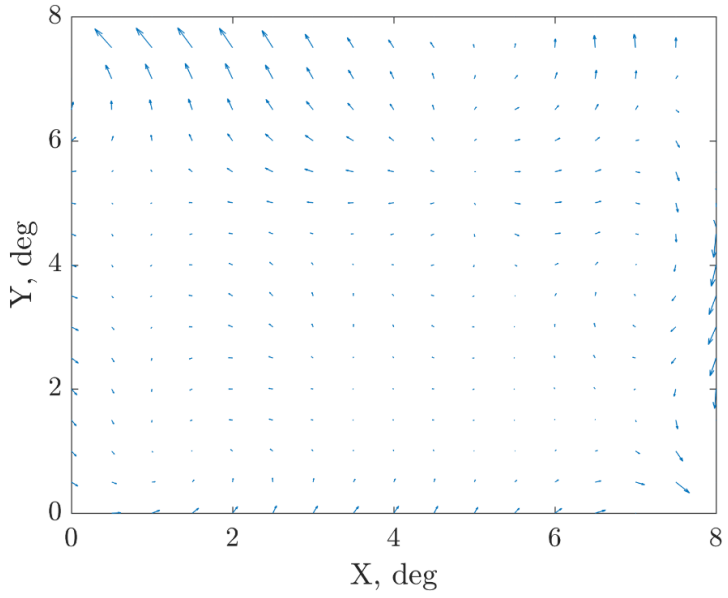

Figure 141: Distortion vector map for the ICESat IST, generated from blue star observations collected during campaign L2f.

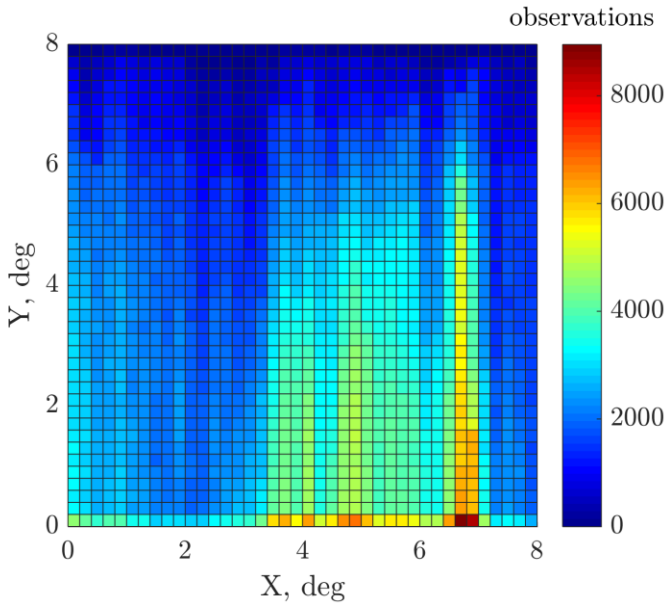

Figure 142: Star density map for the ICESat IST, generated from blue star observations collected during campaign L2f

4.7.18 Mission

Over the duration of the mission, the IST observed 265,501,664 blue stars. This represents 10% of the total observations for the full mission. The distortion map, distortion vector map, and star density map generated using the entirety of the blue star observations collected over the mission are provided in the figures below.

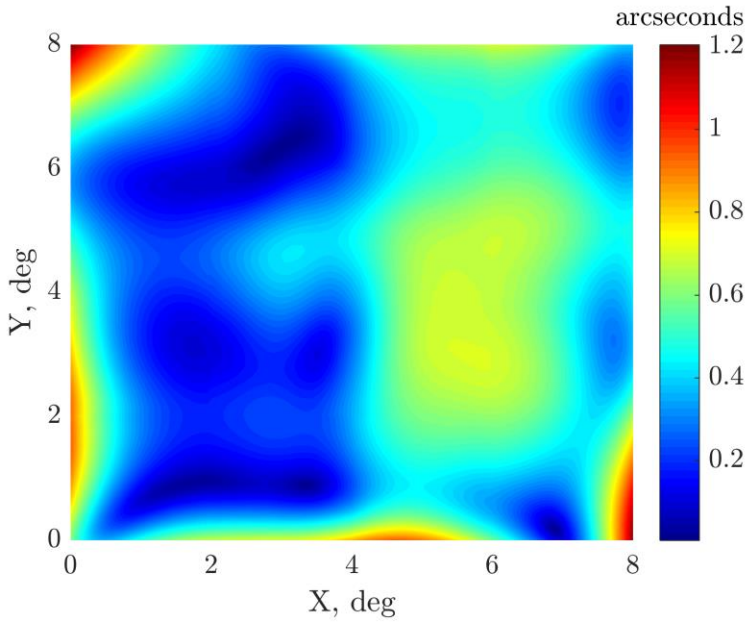

Figure 143: Distortion map for the ICESat IST, generated from blue star observations collected over the full mission.

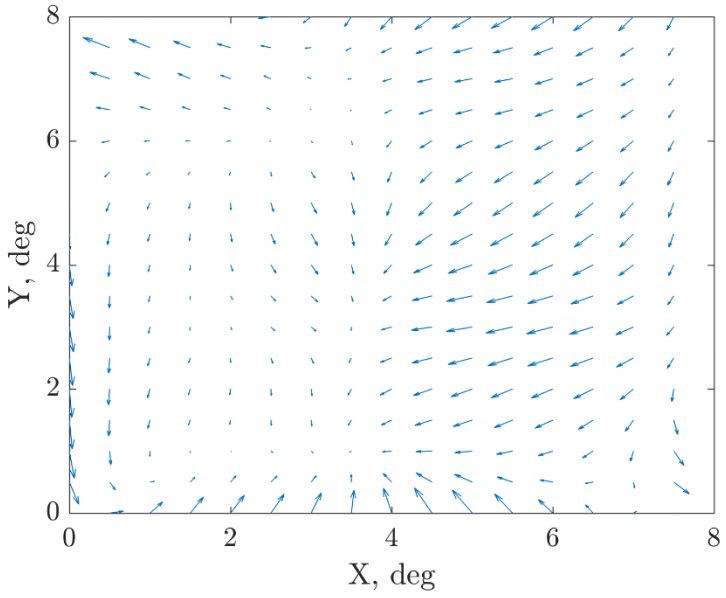

Figure 144: Distortion vector map for the ICESat IST, generated from blue star observations collected over the full mission.

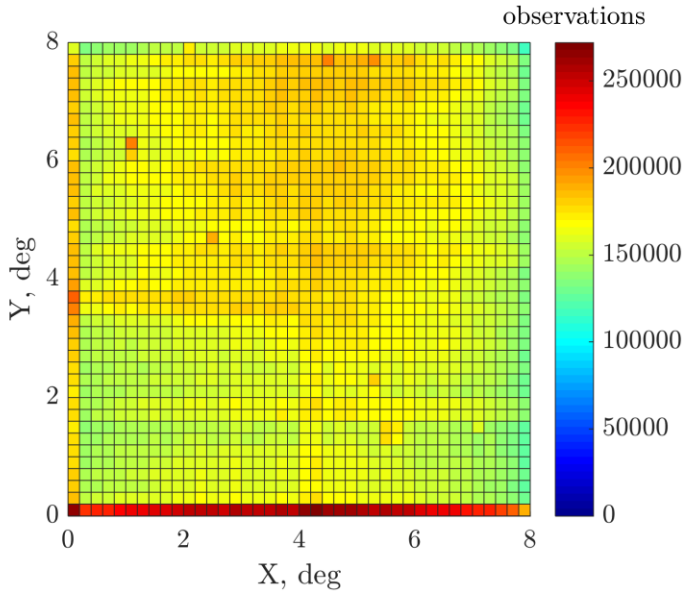

Figure 145: Star density map for the ICESat IST, generated from blue star observations collected over the full mission.

4.7.19 Summary

The results presented in the figures above do not suggest the existence of color-dependent distortion in the ICESat IST. If a color-dependent distortion were to exist, similar artifacts would be distinguishable between different campaigns, such as the red spot of low distortion in campaign L3k. The distortion vector maps no longer reveal the pincushion-type distortion observed in the distortion vector maps generated using all star observations. This indicates either that chromatic aberration was successfully decoupled from lens distortion, or that the distribution of stars is creating regions of higher noise that yield a poor estimate of the distortion coefficients. The latter assertion is supported by the observation that the distortion maps are inconsistent between campaigns, something that was not

observed when distortion maps were generated using all star observations in a campaign.

Because other sources of distortion contribute to these distortion maps, an initial distortion correction using all star observations needs to be performed before generating a color specific distortion map. This will isolate distortion caused by chromatic aberration. The artificially high distortion present in campaigns L1a, L2c, L3c, L3f, and L2d are the result of sparse regions of observations that were created in the FOV by excluding all star observations corresponding to positive B-V color indices. For each campaign, the number of observations used to generate the blue star distortion maps was approximately 10% of the total number of observations. The downsampling analysis suggested that this number of data points is sufficient to generate a stable distortion map; however, because in that study observations were excluded at regular time intervals and not by color, the color-specific observation densities across the FOV do not share the uniformity of observation densities for those in the downsampled case. The regions more heavily impacted by a reduction in observations are more sensitive to noise and result in higher distortion because fewer observations are present to damp the estimated distortion coefficients where high distortion observations may be more dominant.

By lowering the order of the distortion basis function or by using a global approach, these effects should become less pronounced and better illustrate the existence any star color dependent distortion. Because chromatic aberration is star color dependent, determining the existence of chromatic aberration necessitates the adoption of a basis function that incorporates both star color and focal plane position. The localized distortion estimation approach employed here should be

adjusted to incorporate B-V index for chromatic aberration specific distortion estimation across the FOV. Successful consideration of chromatic aberration effects in estimating distortion will allow for more effective reduction in uncertainty in attitude estimates when distortion correction is applied.

Chapter 5: Conclusions and Future Work

A localized attitude dependent distortion estimation method, presented in this thesis, was used to generate distortion maps for each laser campaign of the ICESat mission to determine the effects of certain parameters of interest on the estimated distortion. These parameters included time, apparent motion of stars across the star tracker FOV, region of the celestial sphere observed, frequency and duration of star tracker blinding events, star tracker temperature, and star color. These parameters were selected due to their potential to affect star centroid position, contributing to the estimated distortion over the focal plane. Proper consideration of these parameters will result in the generation of more comprehensive distortion maps that will more effectively reduce the uncertainty in the attitude estimates. The results of this analysis will be incorporated into the precision attitude and pointing determination process for ICESat-2 to achieve improved precision through estimation and correction of star tracker distortion. These results have relevance to any future spacecraft missions that utilize star trackers for the purposes of attitude determination and can be incorporated into calibration or post-processing efforts to reduce uncertainty through mitigation of star tracker distortion.

CCD aging effects were observed over the duration of the mission through an increasing trend in maximum and mean estimated distortion associated with each campaign. The increase corresponded to approximately half an arcsecond to an arcsecond over seven years. The effects of star motion across the FOV manifest as an increase in relative distortion where stars enter the FOV and a decrease in

relative distortion where stars exit the FOV. This was reflected in the distortion maps where features of low distortion were shown to shift in the direction of star motion. There were some evident similarities in the features of the distortion maps generated from observations derived from a similar region of the celestial sphere. However, because of the dependence of the attitude mode on beta angle, it wasn't possible to entirely decouple the effects of the attitude mode and the region of the celestial sphere observed. The comparison between two distortion maps that were generated using similar regions of the celestial sphere and operated in distinct attitude modes suggested that the effects of star motion are more dominant than those related to the properties associated with a given region of stars. Campaigns which experienced a higher frequency of star tracker blinding events yielded higher distortion estimates due to poor attitude estimates inflating the observed distortion value. Excluding distortion observations greater than one arcminute yielded distortion maps more similar in magnitude and shape to those generated for other campaigns, confirming that these high distortion observations caused inflated distortion estimates for these campaigns. Star tracker temperature was discovered to be insignificant in modeling campaign-based distortion of the star tracker focal plane, primarily because temperature on the ICESat optical bench did not fluctuate significantly. Chromatic aberration in the IST was also not observed. This was in part caused by the non-uniformity of observations created by isolating blue stars which yielded regions of sparse observations that inflated the estimated distortion in some cases and resulted in inconsistent distortion maps between campaigns.

These results indicate that implementing a distortion map to correct star positions collected over the duration of a mission for use in generating improved

attitude estimates in post-processing for precision pointing applications such as geolocation should be effective if the distortion map is estimated with proper consideration of parameters that can introduce artifacts that negatively impact the performance of this method. CCD aging effects should be considered if a static distortion model yields distortion residuals with a temporal dependence. Star observations should sufficiently span the FOV with uniform density to reduce the influence of outliers on the estimated distortion for regions of the FOV with relatively sparse observations. Recognizing that spacecraft maneuvers are not typically driven by calibration requirements of attitude sensors, it is recommended that this artifact be compensated for through additional post-processing techniques that identify and either exclude or reduce the weight of high distortion observations corresponding to poor attitude estimates from sources not attributable to systematic star tracker distortion. If additional star trackers are available to support attitude determination while the star tracker of interest is blinded, these artifacts will not be as significant and additional post-processing would be unnecessary. By estimating distortion using observations from different regions of the celestial sphere, any contributions from properties associated with stars corresponding to a specific region can be reduced. The incorporation of telemetry from additional star trackers to support attitude estimation during periods when the star tracker of interest is blinded would eliminate the artifacts that resulted in the high distortion estimates for campaigns L2c, L3c, and L3f. Including data from the BSTs to supplement IST distortion estimation is an area of future work. A more effective approach to estimate and correct for chromatic aberration would require the adjustment of the distortion basis function to incorporate star color

dependent coefficients for direct estimation of both position and star color dependent distortion. There is potential for this method to be applied to low cost star trackers to improve their performance and reduce attitude uncertainty if the precision is limited by systematic distortion. This is an additional area of future work. Proper consideration of the results presented in this thesis will yield a more robust distortion estimation and correction process for future missions which require precision pointing, such as ICESat-2, effectively reducing the uncertainty in the estimated attitude and improving mission performance.

Appendix 1: ICESat Campaign Properties

Campaign	Year	Day of Year	Calendar Day	Total Days	S/C Attitude Mode (GLAS Frame)	Star Movement in FOV (IST Frame)	Total Number of Observations	Initial Beta Angle, deg	Final Beta Angle, deg
L1a	2003	051 – 088	20 Feb – 29 Mar	38	Sailboat/Airplane (-Y/+X)	Left to Right/Bottom to Top (+x/+y)	145352382	-45	-32
L2a	2003	268 – 323	25 Sep – 19 Nov	55	Sailboat (+Y)	Right to Left (-x)	254282205	51	69
L2b	2004	048 – 081	17 Feb – 21 Mar	34	Sailboat (+Y)	Right to Left (-x)	137380590	54	40
L2c	2004	139 – 173	18 May – 21 Jun	35	Airplane (-X)	Top to Bottom (-y)	135654382	13	-4
L3a	2004	277 – 313	03 Oct – 08 Nov	37	Sailboat (-Y)	Left to Right (+x)	161387262	-48	-58
L3b	2005	048 – 083	17 Feb – 24 Mar	36	Sailboat (-Y)	Left to Right (+x)	151888368	-56	-45
L3c	2005	140 – 174	20 May – 23 Jun	35	Airplane (+X)	Bottom to Top (+y)	137303074	-20	-4
L3d	2005	294 – 328	21 Oct – 24 Nov	35	Sailboat (+Y)	Right to Left (-x)	159025723	51	63
L3e	2006	053 – 087	22 Feb – 28 Mar	35	Sailboat (+Y)	Right to Left (-x)	156443642	62	48
L3f	2006	144 – 177	24 May – 26 Jun	34	Airplane (-X)	Top to Bottom (-y)	133451338	20	4
L3g	2006	298 – 331	25 Oct – 27 Nov	34	Sailboat (-Y)	Left to Right (+x)	145423157	-44	-54
L3h	2007	071 – 104	12 Mar – 14 Apr	34	Sailboat (-Y)	Left to Right (+x)	150349948	-60	-47
L3i	2007	275 – 309	02 Oct – 05 Nov	35	Sailboat (+Y)	Right to Left (-x)	144878058	32	46
L3j	2008	048 – 081	17 Feb – 21 Mar	34	Sailboat (+Y)	Right to Left (-x)	159760021	74	62
L3k	2008	278 – 293	04 Oct – 19 Oct	16	Airplane (+X)	Bottom to Top (+y)	67748591	-28	-32
L2d	2008	330 – 352	25 Nov – 17 Dec	23	Sailboat (-Y)	Left to Right (+x)	94009239	-45	-53
L2e	2009	068 – 101	09 Mar – 11 Apr	34	Sailboat (-Y)	Left to Right (+x)	155654414	-71	-59
L2f	2009	273 – 284	30 Sep – 11 Oct	12	Airplane (-X)	Top to Bottom (-y)	46875331	20	25

Appendix 2: Star Observation Correlation Coefficients

	L1a	L2a	L2b	L2c	L3a	L3b	L3c	L3d	L3e	L3f	L3g	L3h	L3i	L3j	L3k	L2d	L2e	L2f
L1a	1	0.07	0.38	0.08	0.09	**0.73**	0.09	0.10	0.21	0.08	0.12	0.15	0.11	0.15	0.09	0.38	0.11	0.11
L2a	0.07	1	0.04	0.05	**0.44**	0.06	0.11	0.39	0.03	0.06	0.20	0.06	0.36	0.03	0.21	0.07	0.07	0.19
L2b	0.38	0.04	1	0.08	0.05	0.39	0.08	0.05	0.50	0.06	0.06	0.15	0.06	0.23	0.05	0.14	0.09	0.06
L2c	0.08	0.05	0.08	1	0.05	0.11	0.39	0.03	0.14	**0.54**	0.04	0.18	0.04	0.19	0.03	0.05	0.27	0.03
L3a	0.09	**0.44**	0.05	0.05	1	0.08	0.08	0.21	0.03	0.07	0.24	0.06	0.21	0.03	0.27	0.07	0.06	0.13
L3b	**0.73**	0.06	0.39	0.11	0.08	1	0.10	0.08	0.33	0.08	0.10	0.25	0.09	0.23	0.08	0.17	0.14	0.09
L3c	0.09	0.11	0.08	0.39	0.08	0.10	1	0.08	0.10	0.28	0.06	0.22	0.08	0.13	0.05	0.05	0.45	0.07
L3d	0.10	0.39	0.05	0.03	0.21	0.08	0.08	1	0.03	0.04	0.41	0.06	**0.97**	0.02	0.38	0.10	0.05	**0.77**
L3e	0.21	0.03	0.50	0.14	0.03	0.33	0.10	0.03	1	0.08	0.04	0.28	0.03	**0.75**	0.03	0.09	0.15	0.04
L3f	0.08	0.06	0.06	**0.54**	0.07	0.08	0.28	0.04	0.08	1	0.04	0.13	0.05	0.09	0.03	0.04	0.17	0.04
L3g	0.12	0.20	0.06	0.04	0.24	0.10	0.06	0.41	0.04	0.04	1	0.05	0.41	0.04	**0.83**	0.15	0.05	0.34
L3h	0.15	0.06	0.15	0.18	0.06	0.25	0.22	0.06	0.28	0.13	0.05	1	0.07	0.37	0.04	0.07	**0.67**	0.06
L3i	0.11	0.36	0.06	0.04	0.21	0.09	0.08	**0.97**	0.03	0.05	0.41	0.07	1	0.02	0.36	0.12	0.06	0.81
L3j	0.15	0.03	0.23	0.19	0.03	0.23	0.13	0.02	**0.75**	0.09	0.04	0.37	0.02	1	0.03	0.07	0.23	0.03
L3k	0.09	0.21	0.05	0.03	0.27	0.08	0.05	0.38	0.03	0.03	**0.83**	0.04	0.36	0.03	1	0.10	0.04	0.31
L2d	0.38	0.07	0.14	0.05	0.07	0.17	0.05	0.10	0.09	0.04	0.15	0.07	0.12	0.07	0.10	1	0.05	0.13
L2e	0.11	0.07	0.09	0.27	0.06	0.14	0.45	0.05	0.15	0.17	0.05	**0.67**	0.06	0.23	0.04	0.05	1	0.05
L2f	0.11	0.19	0.06	0.03	0.13	0.09	0.07	**0.77**	0.04	0.04	0.34	0.06	0.81	0.03	0.31	0.13	0.05	1

The highest correlation coefficients for each campaign are highlighted in red.

References

[1] Schutz, B. E., Zwally, H. J., Shuman, C. A., Hancock, D., and DiMarzio, J. P., "Overview of the ICESat Mission," *Geophysical Research Letters*, vol. 32, 2005.

[2] Rim, H. J., and Schutz, B. E., *Geoscience Laser Altimeter System (GLAS) Precision Orbit Determination (POD) - Algorithm Theoretical Basis Document Version 2.2*, Center for Space Research, The University of Texas at Austin, 2002.

[3] *ICESat Attitudes*, NASA Distributed Active Archive Center (DAAC) at NSIDC, 2014.

[4] Bae, S., and Schutz, B. E., *Geoscience Laser Altimeter System (GLAS) Precision Attitude Determination (PAD) - Algorithm Theoretical Basis Document Version 2.2*, Center for Space Research, The University of Texas at Austin, 2002.

[5] Smith, N. H., "Localized Distortion Estimation and Correction for the ICESat Star Trackers," M. S., The University of Texas at Austin, 2006.

[6] Urban, T., Bae, S., Rim, H. J., Webb, C., and Yoon, S., *CSR SCF Release Notes for Orbit and Attitude Determination Version 3.0*, Center for Space Research, The University of Texas at Austin, 2011.

[7] Smith, N. H., Bae, S., and Schutz, B. E., *Ice, Cloud, and Land Elevation Satellite 2 (ICESat-2) Project - Algorithm Theoretical Basis Document for Precision Pointing Determination Version 1.0*, Center for Space Research, The University of Texas at Austin, 2014.

[8] Correll, T., *Advanced Topographic Laser Altimeter System (ATLAS) - Laser Reference System (LRS) Command and Data Interface Control Document (ICD) Revision A*, Goddard Space Flight Center, 2012.

[9] *The ICESat-2 Mission Level-1 Requirements and Mission Success Criteria Version 4.0*, NASA Goddard Space Flight Center, 2013.

[10] "Saturation and Blooming," *Photometrics* Available: http://www.photometrics.com/resources/learningzone/saturationblooming.php .

[11] Liebe, C. C., "Accuracy Performance of Star Trackers - A Tutorial," *IEEE Transactions on Aerospace and Electronic Systems*, vol. 38, Apr. 2002, pp. 587–599.

[12] Bae, S., and Wolfenbarger, N., "Distortion Correction of the ICESat Star Tracker Data," *AAS/AIAA Space Flight Mechanics Meeting*, Napa, California: 2016, pp. 99–112.
[13] Shuster, M. D., "Focal-Plane Representation of Rotations," *The Journal of Astronautical Sciences*, vol. 48, Sep. 2000, pp. 381–390.
[14] Spratling, B. B., and Mortari, D., "A Survey on Star Identification Algorithms," *Algorithms*, vol. 2, Jan. 2009, pp. 93–107.
[15] Wahba, G., "A Least Squares Estimate of Satellite Attitude," *SIAM Review*, vol. 7, 1965, p. 409.
[16] Markley, F. L., "Three-Axis Attitude Determination Methods," *Spacecraft Attitude Determination and Control*, J.R. Wertz, ed., Springer Science & Business Media, 2012.
[17] Markley, F. L., and Mortari, D., "Quaternion Attitude Estimation using Vector Observations," *Journal of the Astronautical Sciences*, vol. 48, 2000, pp. 359–380.
[18] Shuster, M. D., and Oh, S. D., "Three-Axis Attitude Determination from Vector Observations," *Journal of Guidance, Control, and Dynamics*, vol. 4, Jan. 1981, pp. 70–77.
[19] Lefferts, E. J., Markley, F. L., and Shuster, M. D., "Kalman Filtering for Spacecraft Attitude Estimation," *Journal of Guidance, Control, and Dynamics*, vol. 5, Sep. 1982, pp. 417–429.
[20] Fisher, H. L., Shuster, M. D., and Strikwerda, T. E., "Attitude Determination for the Star Tracker Mission," *AAS/AIAA Astrodynamics Specialist Conference*, Stowe, Vermont: AAS, 1989, pp. 139–150.
[21] Rufino, G., and Accardo, D., "Enhancement of the centroiding algorithm for star tracker measure refinement," *Acta Astronautica*, vol. 53, 2003, pp. 135–147.
[22] Fowell, R. A., Smith, N. H., Bae, S., and Schutz, B. E., "Bad Stars," *Proceedings of the 32nd Annual AAS Rocky Mountain Guidance and Control Conference*, Breckenridge, Colorado: AAS, 2009, pp. 19–36.
[23] Lam, Q., Woodruff, C., Ashton, S., and Martin, D., "Noise Estimation for Star Tracker Calibration and Enhanced Precision Attitude Determination," *IEEE Fifth International Conference on Information Fusion*, 2002, pp. 235–242.
[24] Mikhail, E. M., Bethel, J. S., and McGlone, J. C., *Introduction to Modern Photogrammetry*, New York: John Wiley & Sons, 2001.

[25] Griffith, T. D., Singla, P., and Junkins, J. L., "Autonomous On-orbit Calibration Approaches for Star Trackers," *AAS/AIAA Space Flight Mechanics Meeting*, San Antonio, Texas: AAS, 2002, pp. 39–57.

[26] *Attributes for Laser Operations Periods*, NASA Distributed Active Archive Center (DAAC) at NSIDC, 2014.

[27] Fernando, K. C., "Hot Pixel Detection for Star Trackers," M. S., Ryerson University, 2009.

[28] Waltham, N., "CCD and CMOS sensors," *Observing photons in space*, Springer, 2013, pp. 423–442.

[29] Enright, J., Sinclair, D., and Fernando, K. C., "COTS Detectors for Nanosatellite Star Trackers: A Case Study," *25th Annual AIAA/USU Conference on Small Satellites*, Logan, Utah: 2011.

[30] Mallon, J., and Whelan, P. F., "Calibration and removal of lateral chromatic aberration in images," *Pattern Recognition Letters*, vol. 28, Jan. 2007, pp. 125–135.

Vita

Natalie Soheila Wolfenbarger was born in Redondo Beach, California, on June 20, 1991. She received her Bachelor of Science in Aerospace Engineering at California Polytechnic State University, San Luis Obispo in 2013. During her undergraduate career, she supported the integration and test of CubeSats and performed deployment and orbit simulation. In the summer of her third year, she interned at NASA Goddard Space Flight Center in the propulsion group. Prior to starting graduate school, she worked at SpaceX as a dynamics intern.

Permanent contact: nswolfen@gmail.com

This thesis was typed by the author.